UNIVERSITY OF OKLAHOMA

GRADUATE COLLEGE

SEARCH FOR THE STANDARD MODEL HIGGS BOSON PRODUCTION AND DECAY TO W BOSON PAIRS USING THE LEPTON + MET + JETS CHANNEL USING 4.7 fb^{-1} OF DATA RECORDED BY THE ATLAS DETECTOR AT $\sqrt{s} = 7$ TEV PROTON-PROTON COLLISION

A DISSERTATION

SUBMITTED TO THE GRADUATE FACULTY

in partial fulfillment of the requirements for the

Degree of

DOCTOR OF PHILOSOPHY

By

DILIP KUMAR JANA
Norman, Oklahoma
2013

SEARCH FOR THE STANDARD MODEL HIGGS BOSON PRODUCTION AND DECAY TO W BOSON PAIRS USING THE LEPTON + MET + JETS CHANNEL USING 4.7 fb^{-1} OF DATA RECORDED BY THE ATLAS DETECTOR AT $\sqrt{s} = 7$ TEV PROTON-PROTON COLLISION

A DISSERTATION APPROVED FOR THE HOMER L. DODGE DEPARTMENT OF PHYSICS AND ASTRONOMY

BY

Dr. Patrick L. Skubic, Chair

Dr. Phillip Gutierrez

Dr. Brad Abbott

Dr. Eric Abraham

Dr. Zhisheng Shi

Acknowledgements

I would like to thank my advisor, Patrick L. Skubic, for his energy and enthusiasm, and for sending me to CERN and allowing me to conduct independent research. Thank you to all the members of the University of Oklahoma High Energy Physics Group.

None of the research presented in this thesis would have been possible without proper funding. This work was supported by a graduate research fellowship from US Department of Energy Grant DE-FOA-0000733.

I enjoyed working with the ATLAS pixel group while commissioning the pixel detector. A special thanks goes to Sara Strandberg, Heather Gray and Markus Keil during calibration and commissioning of the pixel detector.

I had pleasure working with Martine Bosman, Richard Hawkings when they were top quark working group convenors. Very special thanks goes to Tobias Golling from whom I learned multivariate technique for $t\bar{t}$ cross-section measurements. Thank you Tobi!

During Higgs boson search analysis, I had pleasure working with Bill Murray, Sandra Kortner, Christopher Arnold Walker, Jianming Qian, Bill Quayle, Rikard Sandstrom, Mark Neubauer, Lashkar Kashif and Magda Chelstowska. Chris was always there to help me, whenever I needed. Without your invaluable help, this thesis would not have been possible. Thanks so much Chris!

I am grateful to Satya Nandi and Rohini Godbole for their help in under-

standing theoretical high energy physics. Many thanks to Supriya Jain for her support and invaluable discussions during difficult times of the analysis. Thanks to Jane and Phillip Gutierrez for their help and company during our stay in Saint Genis!

I would like to thank all my friends specially Aveek Sarkar, Prachi Parashar, K. V. Shajesh for their help and support.

I would like to express my deep gratitude towards my parents and all family members for their love, care and blessings. I am forever grateful to my loving wife, Sunanda, who has made huge sacrifices in her life during my PhD. She has always been loving and patient beyond measure. My daughter, Debashmita, gave me the final delight by coming to Earth right before defending my PhD! Love you Debashmita!

During the course of my PhD thesis work at CERN, I was privileged to work on many different projects with many different people. This makes it impossible to thank individually all of the people who contributed to my PhD. To everyone I am so grateful.

Table of Contents

Abstract

A search for the Standard Model Higgs boson decaying to two W bosons with the subsequent decay to a final state containing one lepton, one neutrino, and two (or three) jets ($H \to WW^* \to \ell\nu jj$ where ℓ stands for electron or muon) is presented using 4.7 fb^{-1} of data recorded by the ATLAS detector in 2011 at center of mass energy $\sqrt{s} = 7$ TeV. No significant excess is observed over the expected Standard Model background. Limits on the Higgs production cross section are derived for masses between $m_H = 300$ GeV and $m_H = 600$ GeV. For a Higgs boson mass $m_H = 400$ GeV, the 95% confidence level upper bound on the cross-section for Higgs boson production by gluon fusion times the branching ratio for $H \to WW^*$ is 2.2 pb, or approximately 1.9 times the Standard Model prediction.

List of Tables

List of Figures

Chapter 1

Introduction

Over several decades, the Standard Model (SM) of particle physics has been able to successfully describe experimental results which are consistent with theoretical predictions. However, one important particle in the model, the Higgs boson which is believed to give mass to other particles, is not yet discovered. Very recently both ATLAS and CMS collaborations have discovered a new boson at ∼125 GeV in the search for SM Higgs boson [1, 2] using $H \to \gamma\gamma$, $H \to ZZ \to \ell\ell\ell\ell$ where ℓ stands for electron or muon. There is also evidence of this new boson using $H \to WW^* \to \ell\nu\ell\nu$ decay channel. There is compelling theoretical demand for the existence of new particles and interactions at TeV energy scales. Therefore, it is of great importance to search for the Higgs boson in the high mass range ($m_H > 300$ GeV) as well using $H \to WW^* \to \ell\nu jj$ decay channel and this is the content of this thesis. The challenge of this analysis is to extract a small Higgs boson signal from large backgrounds.

The thesis is organized as follows: Chapter 2 discusses the theory of the Higgs boson, Chapter 3 gives an overview of the Large Hadron Collider and the ATLAS detector that was used for Higgs boson searches in this thesis, Chapter 4 gives the Higgs boson search strategy in the $H \to WW^* \to \ell\nu jj$ decay channel. Finally Chapter 5 describes the present status of the Higgs searches at the LHC and its implication to the present analysis.

Chapter 2

The Standard Model and the Higgs Boson

The Standard Model [3, 4, 5, 6, 7, 8] of particle physics is a quantum field theory which describes all known fundamental constituents of matter and their interactions. This theory is based on the symmetries of the $SU(3)_c \otimes SU(2)_L \otimes U(1)_Y$ gauge group. The Standard Model is the first successful theory which unifies three of the four forces: electromagnetic, weak and strong forces at very small distance scales ($\approx 10^{-15}$ m). Since we are not able to describe gravity by a renormalizable quantum field theory, it is not included in the Standard Model. After a brief description of the constituents of matter and fundamental forces, we discuss how fermions and bosons acquire mass interacting with the Higgs field. Finally a short review of the status of the present Higgs boson searches at the Large Hadron Collider (LHC) will be presented. It will also include the Higgs boson search strategy using $H \to WW^* \to \ell\nu jj$ decay channel which is the main work of this thesis.

2.1 The elementary constituents of matter

The elementary particles are divided into two categories: fermions and bosons. Fermions have half-integer spin and obey the Pauli exclusion principle, which states that two fermions cannot be in the same quantum state. Bosons have integer spin value. Fermions are divided into two families: leptons and quarks.

Quarks and leptons exist in three generations which have the same quantum states but have different mass. The mass increases with the increase of generations.

In Table 2.1 and Figure 2.1, we list the particles of the Standard Model.

The first generation of fermions are the most common in the universe, i.e., u and d quarks are present in nucleons and form nuclei. Electrons revolve around the nuclei to form atoms, and the neutrino is produced in large amounts in stars. The c and s quarks, the μ and its associated neutrino form the second generation. Finally, the third generation is comprised of the t and b quark, the τ lepton and its associated neutrino. Particles in higher generations can be produced in high-energy interactions, through man-made accelerators or when cosmic rays hit the upper atmosphere. The particles in the higher generations are unstable and eventually decay into photons or stable first generation of particles.

Experimentally, masses of the neutrinos are very small; the Standard Model assumes that the neutrino mass is 0. The neutrino interacts very rarely with matter since it participates only in the weak interaction. This makes the direct detection of neutrinos very difficult, but their presence can be detected by measuring the imbalance of the total momentum.

Quarks are paired in each generation where one of them has $+\frac{2}{3}$ times the

	symbol	name	mass (GeV/c^2)	charge (e)
Quarks	d	down	≈ 0.008	$-1/3$
(spin = 1/2)	u	up	≈ 0.004	2/3
	s	strange	≈ 0.015	$-1/3$
	c	charm	≈ 1.4	2/3
	b	bottom	≈ 4.5	$-1/3$
	t	top	≈ 175	2/3
Leptons	e	electron	0.000511	-1
(spin=1/2)	ν_e	electron neutrino	$< 3 \times 10^{-9}$	0
	μ	muon	0.01057	-1
	ν_μ	muon neutrino	< 0.00019	0
	τ	tau	1.777	-1
	ν_τ	tau neutrino	< 0.0182	0
Gauge bosons	γ	photon	0	0
(spin = 1)	W	W	80.4	1
	Z	Z	91.2	0
	g	gluon	0	0
Higgs	H	Higgs	~ 125	?

Table 2.1: Particles in the Standard Model.

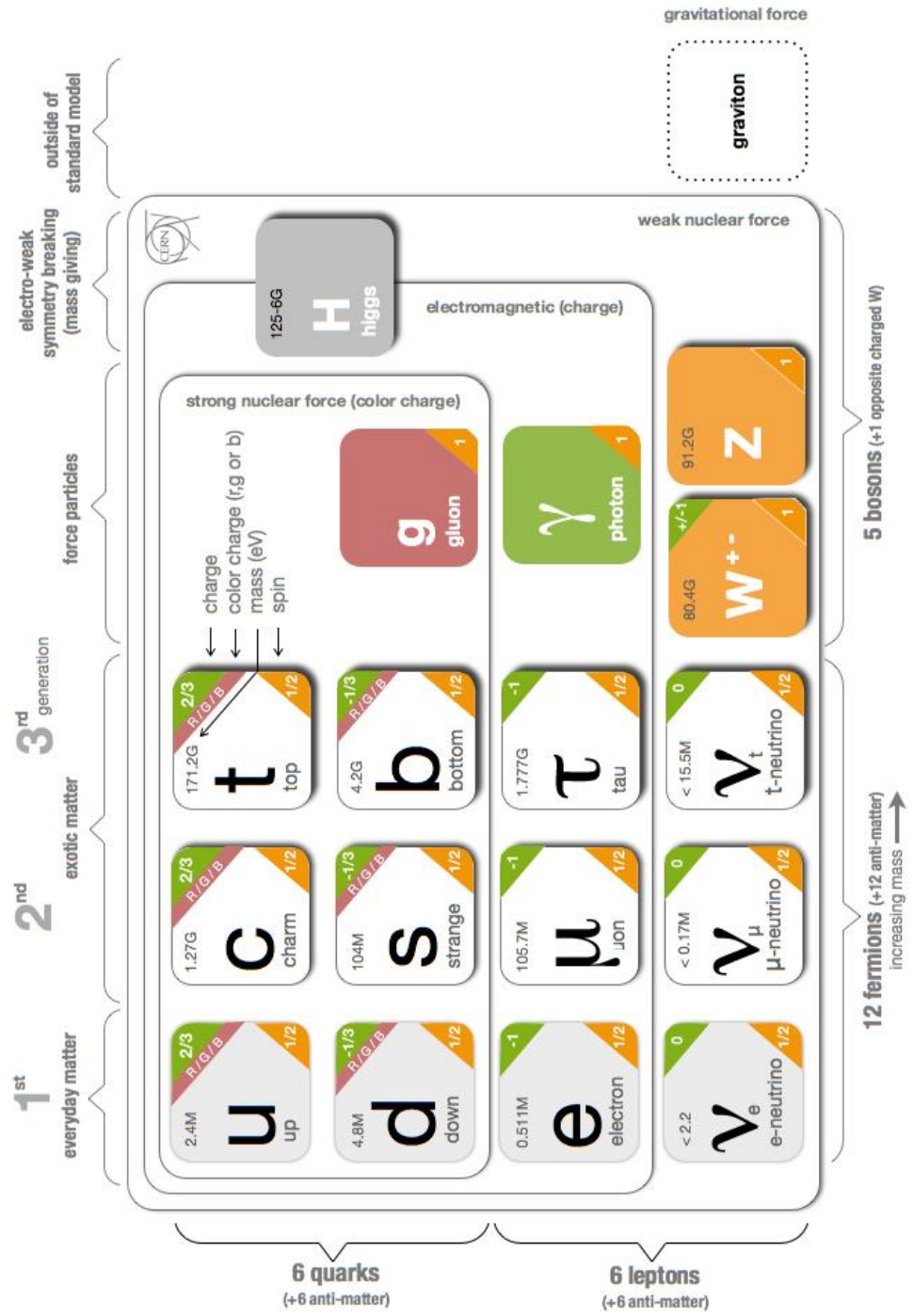

Figure 2.1: Particles in the Standard Model

magnitude of the electron charge (u, c and t quarks), whereas the other has a $-\frac{1}{3}$ times the magnitude of the electron charge (d, s and b quarks). Quarks can be grouped in $q\bar{q}$ pairs to form mesons with baryon number 0 or it can be grouped with three quarks to form baryons with baryon number[1] 1. The baryon number and lepton number[2] have to be conserved. Fermions are produced in particle-antiparticle pairs in order to preserve these conservation laws.

The gauge bosons ($W^{\pm}, Z, \gamma, g$) are spin-1 particles, and act as mediators of the electromagnetic, weak and strong forces. The Graviton, a spin-2 particle, is hypothesized to be the mediator of the gravitational force. However, we have not observed the graviton yet.

2.2 Fundamental Forces

The Standard Model unifies the electromagnetic, weak and strong forces. Each of these forces belong to different gauge groups. This dictates their behavior and interactions with other particles. Each force is mediated by a bosonic field which is exchanged between particles when interacting with each other. Though the Standard Model does not include gravity, it will be discussed here for completeness of the subject. Figure 2.2 shows the relative strengths of the four

[1] a number equal to the difference between the number of baryons and the number of antibaryons in any subatomic structure.

[2] the number of leptons minus the number of antileptons

basic forces. At small energies, the forces differ greatly. The weak and EM forces become identical at energies available at accelerators, or unified. Unfortunately, the energies at which the strong and electroweak forces become the same are probably unreachable at any conceivable accelerator.

2.2.1 Electromagnetic Force

The electromagnetic force is responsible for all electromagnetic processes, and its mediator is the photon. The symmetry group of the electromagnetic interactions is U(1). The coupling strength of the electromagnetic interaction is $\alpha \approx 1/137$ and its range is ∞.

2.2.2 Weak Force

The weak force is responsible for nuclear processes like nuclear β decay. Its mediators are the massive gauge bosons $W^{\pm}$ and Z. It belongs to the SU(2) symmetry group. The weak field strength is about a factor of 10^{-11} of that of the electromagnetic force and 10^{-13} of the typical field g of the weak interaction is defined by the equation

$$\frac{G_F}{\sqrt{2}} = \frac{g^2}{8M_W^2} \tag{2.1}$$

where M_W is the mass of the W boson and $G_F = 1.16637 \times 10^{-5}\ GeV^{-2}$ is the Fermi constant. The weak force is the only interaction that can change flavor. Weak interactions can also violate parity symmetry P as well as charge

conjugation-parity symmetry CP.

2.2.3 Strong Force

The strong force ('quantum chromodynamics' or 'QCD') is mediated by gluons. Gluons couple to objects which possess 'color' charge, which are the quarks and the gluons themselves. A color charge has three possible values, conventionally called 'red', 'green' and 'blue' for quarks; antiquarks come in 'anti-red', 'anti-green' and 'anti-blue' colors. However, as the energy of interaction increases, the strength of the strong coupling gets smaller. Therefore at the high energies typical of modern high-energy experiments, quarks behave nearly like free particles ('*asymptotic freedom*'). However, at lower energies (such as would be typical of quarks bound in a nucleon) the coupling strength becomes large enough that perturbation theory breaks down. The fact that the strength of this interaction increases as the energy of the interaction decreases, ensures that at distance scales larger than a nucleon, quarks always appear in bound states, a phenomenon known as *quark confinement*. These bound states (called hadrons) are always formed so that the color charges cancel exactly (either a quark and its antiquark with the opposite color, or a mixture of all three colors).

In order to pull a quark out of a bound state, one must expend sufficient energy to create a new quark-antiquark pair, one of which will pair with the removed quark, and the other one will take the place of the removed quark. This means that if a quark is produced or knocked out of a nucleus in some

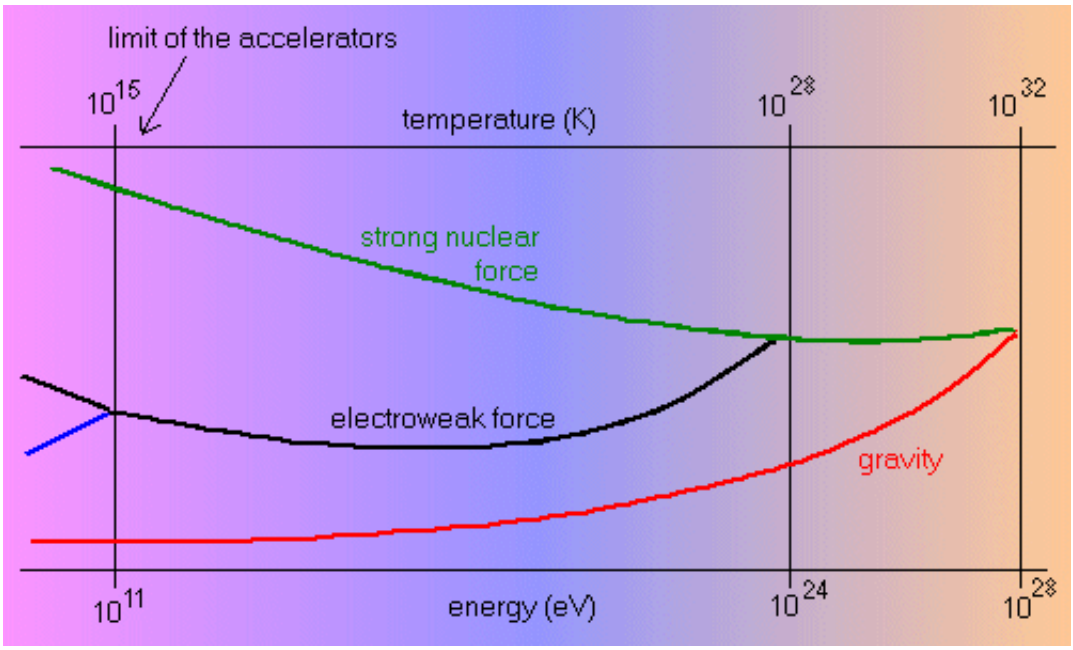

Figure 2.2: The relative strengths of the four basic forces and their unification.

interaction, it will rapidly 'clothe' itself with other quarks which bind together to form a collection of composite particles[3]. Experimentally, what we 'see' is not a single quark or gluon, but a collimated *jet* of many hadrons moving along directions close to that of the original quark.

2.2.4 Gravity

General relativity is the fundamental theory of gravity. There is, however, no fundamental theory of quantum gravity yet and it is in particular not described by the Standard Model. The range of this force is ∞ and it is weaker than the other forces. We will add further details in the relevant places in later chapters as gravity becomes important again at the Planck scale.

[3]This process is usually called '*fragmentation* and *hadronization*'.

2.3 Electroweak theory and Spontaneous Symmetry breaking

Abdus Salam, Sheldon Glashow and Steven Weinberg received the Nobel Prize in Physics in 1979 "for their contributions to the theory of the unified weak and electromagnetic interaction between elementary particles" [9]. They unified the electromagnetic and weak interactions into one theoretical description called the electroweak interaction. With the discovery of neutral currents in neutrino scattering and the discovery of the W and Z bosons at CERN in 1983 [10], the existence of the electroweak force was established. The new symmetry group of the combined electroweak interaction is $SU(2)_L \otimes U(1)_Y$. The gauge bosons of this group are the photon, $W^{\pm}$ and Z bosons. The index L is the left-handed fermions that interact weakly. Y is the weak hypercharge defined as $Y = 2(Q - T_3)$ where Q is the electric charge and T_3 is the third component of the weak isospin.

The Lagrangian of the interactions of the fermions and the bosons can be written as

$$\mathcal{L}_{ew} = \frac{1}{4} G^{\mu\nu} . G_{\mu\nu} - \frac{1}{4} F^{\mu\nu} F_{\mu\nu} + \sum_k \psi_k i \gamma^\mu D_\mu \psi_k \tag{2.2}$$

$G_{\mu\nu}$ is a field tensor given by

$$G_{\mu\nu} = \partial_\mu W_\nu - \partial_\nu W_\mu + ig \left[W_\mu, W_\nu \right] \tag{2.3}$$

with $W_\mu = \frac{\tau^l}{2} W^l_{\mu'} W^l_\mu$ being an isotriplet of gauge fields and $\frac{\tau^l}{2}$ being the generators of the weak symmetry group SU(2), where τ^l denotes the Pauli matrices. The field tensor $F_{\mu\nu} = \partial_\mu B_\nu - \partial_\mu B_\nu$ where B_μ is the vector field associated with the U(1) hypercharge Y.

Interactions between fermions and gauge bosons can be described by the covariant derivatives

$$D_\mu \psi_k = \left(\partial_\mu + ig \frac{\tau^l}{2} W^l_\mu + ig' \frac{1}{2} y_k B_\mu \right) \psi_k \tag{2.4}$$

where y_k is the hypercharge of ψ_k, g is the coupling strength of the weak isotriplet gauge field W^l_μ and g' is the coupling strength of the vector field B_μ.

The following equations identify the terms in the Lagrangian of Eq. 2.2, W^l_μ and B_μ, with the gauge bosons, $W^\pm$ and Z_μ, and the photon field A_μ:

$$W^\pm_\mu = \frac{1}{\sqrt{2}} \left(W^l_\mu \pm W^2_\mu \right) \tag{2.5}$$

$$Z_\mu = -\sin\theta_W B_\mu + \cos\theta_W W^3_\mu \tag{2.6}$$

$$A_\mu = \cos\theta_W B_\mu + \sin\theta_W W^3_\mu \tag{2.7}$$

where $\cos(\theta_W) = g/\sqrt{g^2 + g'^2}$ is the weak mixing angle.

So far, the electroweak Lagrangian correctly describes the interactions between the fermions and between fermions and gauge bosons for massless particles.

But in Nature, we observe particles with masses. Therefore, this is not a perfect description of the behaviors of the interactions of the elementary particles.

2.4 The Higgs Mechanism

To solve the problem of the interactions of massless bosons and fermions, the Higgs mechanism was introduced that offers a gauge invariant way of introducing the concept of mass. Adding a simple mass term like $m_W^2 W_\mu^\dagger W^\mu$ will violate gauge invariance, therefore, we need to introduce an additional SU(2) doublet

$$\phi = \begin{pmatrix} \phi^+ \\ \phi^\circ \end{pmatrix} \tag{2.8}$$

where ϕ^+ and ϕ° are complex fields defined by their real components ϕ_1, ϕ_2, ϕ_3 and ϕ_4:

$$\phi^+ = \frac{\phi_1 + i\phi_2}{\sqrt{2}} \tag{2.9}$$

$$\phi^\circ = \frac{\phi_3 + i\phi_4}{\sqrt{2}} \tag{2.10}$$

The corresponding Lagrangian can be written as

$$\mathcal{L}_\phi = (D_\mu \phi)^\dagger (D_\mu \phi) - V(\phi) \tag{2.11}$$

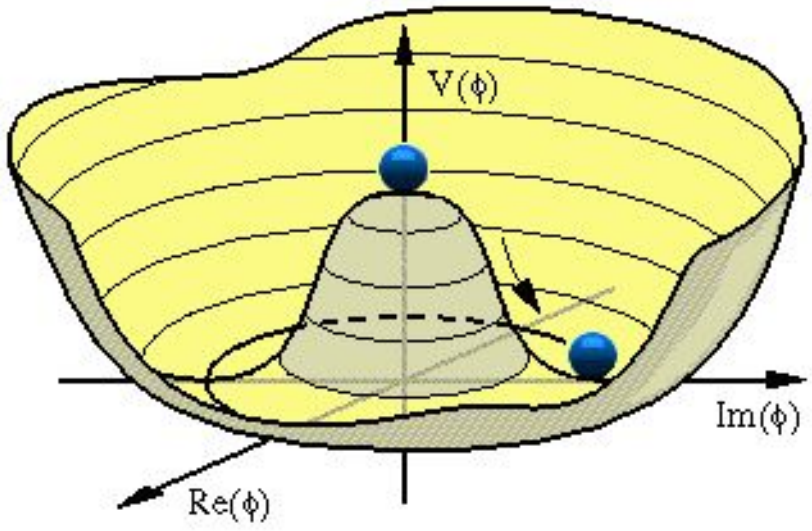

Figure 2.3: The Higgs potential function

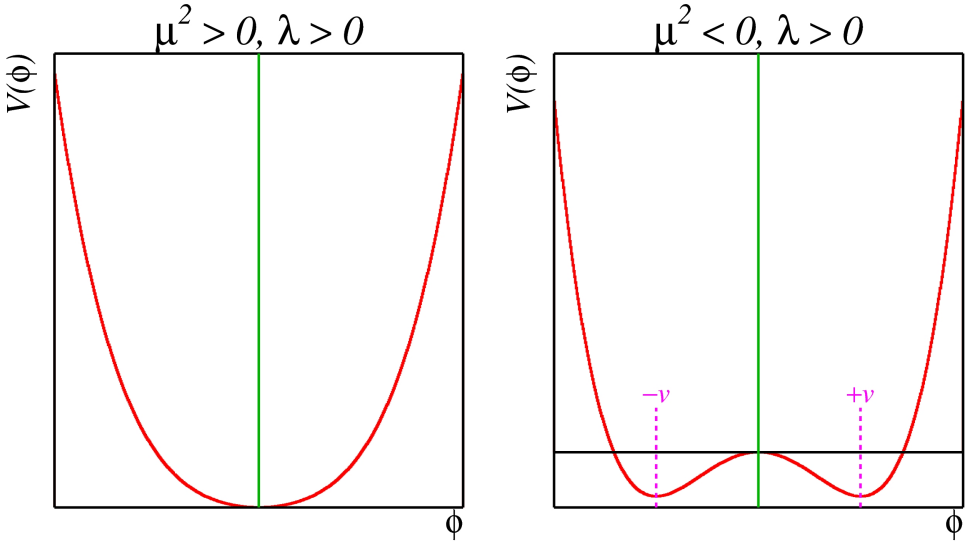

Figure 2.4: The minima of the Higgs potential for $\mu^2 > 0$ (left) and $\mu^2 < 0$ (right) for a scalar field ϕ.

where $V(\phi)$ is the potential energy of the field defined as

$$V(\phi) = \mu^2 \phi^\dagger \phi - \lambda \left(\phi^\dagger \phi\right)^2 . \tag{2.12}$$

This potential has a minimum value for $\mu^2 < 0$ and $\mu^2 > 0$ as shown in Figure 2.4.

$$\begin{aligned} \phi^\dagger \phi &= \phi^{+*} \phi^+ + \phi^{\circ *} \phi^\circ \\ &= \frac{\phi_1^2 + \phi_2^2 + \phi_3^2 + \phi_4^2}{2} \\ &= -\frac{\mu^2}{2\lambda} = \frac{\nu^2}{2}. \end{aligned} \tag{2.13}$$

As shown in Figure 2.3 and Figure 2.4, for $\mu^2 < 0$, the potential $V(\phi)$ has a minimum value at $\phi = \pm\nu$ ($\phi \neq 0$), with $\nu = \sqrt{-\mu^2/\lambda}$. Therefore, the spontaneous symmetry breaking can occur for $\mu^2 < 0$. For $\mu^2 > 0$, $V(\phi)$ has its minimum value at $\phi = 0$ and no spontaneous symmetry breaking can occur. Therefore, we will not consider $\mu^2 > 0$ anymore as we will end up with where we started, a theory of massless particles.

According to Eq. 2.13, the choice of the minimum value of ϕ is not unique, so we have to choose a direction in SU(2) space. The vacuum ground state, ϕ_0, can be written as,

$$\phi_0 = \frac{1}{\sqrt{2}} \begin{pmatrix} 0 \\ \nu \end{pmatrix} \tag{2.14}$$

where $\phi_1 = \phi_2 = \phi_4 = 0$ and $\phi_3 = \nu$.

Expanding Eq. 2.4, we get a term, which is proportional to $W_\mu^- W_\nu^+ \nu^2 g^2$, which can be identified as a mass term:

$$\nu^2 = \frac{4m_W^2}{g^2} \tag{2.15}$$

with $\nu^2 = 246$ GeV.

The full Lagrangian of the electroweak theory incorporating the Higgs mechanism can be written as [11]:

$$\begin{aligned}
\mathcal{L}_{EW} = & -\frac{1}{4} G^{\mu\nu} . G_{\mu\nu} - \frac{1}{4} F^{\mu\nu} F_{\mu\nu} \\
& + m_W^2 W_\mu^\dagger W^\mu (1 + \frac{\phi}{\nu})^2 \\
& + m_Z^2 Z_\mu Z^\mu (1 + \frac{\phi}{\nu})^2 \\
& + \sum_k \psi_k i\gamma^\mu D_\mu \psi_k + \mathcal{L}_Y \\
& + \frac{1}{2} (\partial^\mu \phi)(\partial_\mu \phi) \\
& - \frac{1}{2} m_H^2 \phi^2 (1 + \frac{\phi}{\nu} + \frac{1}{4}(1 + \frac{\phi}{\nu})^2)
\end{aligned} \tag{2.16}$$

where m_W and m_Z are the masses of the W and Z bosons respectively. ϕ is the scalar Higgs field and ν is its vacuum expectation value. $F_{\mu\nu}$ is the electromagnetic field $F_{\mu\nu} = \partial_\mu A_\nu - \partial_\nu A_\mu$. $\mathcal{L}_Y$ is the Yukawa term that generates

the Fermion masses by coupling to the Higgs field:

$$\begin{aligned}\mathcal{L}_Y = -(&g_e\bar{e}_R e_L + g_\mu\bar{\mu}_R\mu_L + g_\tau\bar{\tau}_R\tau_L \\ &+ g_d\bar{d}_R d_L + g_s\bar{s}_R s_L + g_b\bar{b}_R b_L \\ &+ g_u\bar{u}_R u_L + g_c\bar{c}_R c_L + g_t\bar{t}_R t_L \\ &+ h.c.)\frac{\nu}{\sqrt{2}}(1+\frac{\phi}{\nu})\end{aligned} \tag{2.17}$$

2.5 Standard Model

The Standard Model is the combination of the previously discussed theories of electroweak and strong interactions without including the gravitational force. The Lagrangian of the SM has the symmetry group of $SU(3)_c \otimes SU(2)_L \otimes U(1)_Y$ where c denotes the color index of QCD, L implies that only left-handed fermions participate in the weak interaction and Y is the hypercharge. After spontaneous symmetry breaking at energies smaller than 100 GeV, $SU(2)_L \otimes U(1)_Y$ becomes $U(1)_{em}$ which is the usual group of classical QED.

The Standard Model has 19 free parameters and it does not take into account gravity. Therefore, it is very difficult to accept it as a truly fundamental theory. The Standard Model introduces the existence of the scalar Higgs Boson without giving its mass since mass itself is a parameter in the Standard Model! Finding the Higgs Boson at Large Hadron Collider (LHC) is one of the crucial steps necessary to validate The Standard Model. If we find the Higgs Boson, it will be a challenge to identify whether it is the Standard Model Higgs Boson or a

Supersymmetric Higgs Boson.

The vacuum expectation value of the field can be written as

$$< \phi >= \frac{1}{\sqrt{2}} \begin{pmatrix} 0 \\ \nu \end{pmatrix} \tag{2.18}$$

A space-time dependent field fluctuation ψ arises if we perturb the vacuum at $\phi = \pm\nu$.

$$\phi = \frac{1}{\sqrt{2}} \begin{pmatrix} 0 \\ \nu + \psi \end{pmatrix} \tag{2.19}$$

which can be interpreted as the Higgs boson. The Higgs potential after symmetry breaking becomes [12]

$$V(\phi) = \frac{\mu^4}{4\lambda} - \mu^2\psi^2 + \lambda\nu\psi^3 + \frac{\lambda}{4}\psi^4 \tag{2.20}$$

The tree level mass of the Higgs boson can be deduced from the potential V (second term):

$$m_H = \sqrt{-2\mu^2} = \sqrt{2\lambda\nu} \tag{2.21}$$

Since λ is a free parameter, the SM does not predict exactly the mass of the Higgs Boson.

2.6 Experimental overview for Higgs searches

This section will give an introduction into the general framework of making predictions and possibly exclusions of certain mass regions of the Higgs boson taking results from different experiments. Finally, we will give different strategies to hunt for the Higgs boson using the $H \to WW^* \to \ell\nu jj$ channel. However, the reason for choosing a specific event topology, production and decay mode for the Higgs boson search in $H \to WW^* \to \ell\nu jj$ will be presented in the later chapters of this thesis work.

2.6.1 Environment during proton-proton collision

As shown in Figure 2.5, LHC collides two beams of protons, which consist of partons which carry a certain fraction of the proton's momentum, x, shown in Figure 2.6. Partons may be either the valence quarks (uud), the gluons (which are radiated from the quarks) or the sea quarks ($q\bar{q}$ pairs which are spontaneously produced and annihilated instantaneously within the proton). Parton Distribution Functions (PDFs), $f_i(x, Q^2)$, give the probability that parton i (i.e., $u, d..., g$) has momentum fraction x of the proton's momentum at the energy scale $\sqrt{Q^2}$ of the event. It provides how likely it is to find a quark or gluon carrying a definite fraction x of the proton's energy inside an energetic proton. Using $E = \sqrt{x_1 x_2 E_b}$, we can find the total energy available to the two partons that hit each other, where E_b is the center of mass energy of the

proton-proton collision.

As shown in Figure 2.7, for the production of heavy Higgs boson like particles, the part of the event of interest is the hard scatter, where two partons interact with a high centre of mass energy to produce a new massive particle. During the hard scattering process, partons which approach towards the collision point, can emit initial state radiation. Final state radiation may occur after the hard scattering process finishes. This may lead to the presence of a number of high p_T jets in addition to the decay products of whatever is produced in the hard scatter.

Proton remnants may be present after the hard scatter. These remnants will primarily travel in the beam direction and mainly escape down the beam pipe, but some portion of the remnant particles may enter the detectors, particularly in the more forward regions. This contributes to the underlying event.

At the LHC, since extremely high energetic protons collide in bunches, it is highly probable that both multiple parton and multiple proton interactions within the same bunch crossing can occur and may have different properties such as different z position of the interaction vertices. These additional interactions lead to multiple hard scattering processes and many collision vertices. This effect is known as **pileup** and it is an increasing problem for analysis at the LHC as the center-of-mass energy of the hadron collider increases. It may be corrected for during the offline analysis and this will be addressed in Chapter 4.

Cosmic rays always pass through the detector, therefore, there will be some

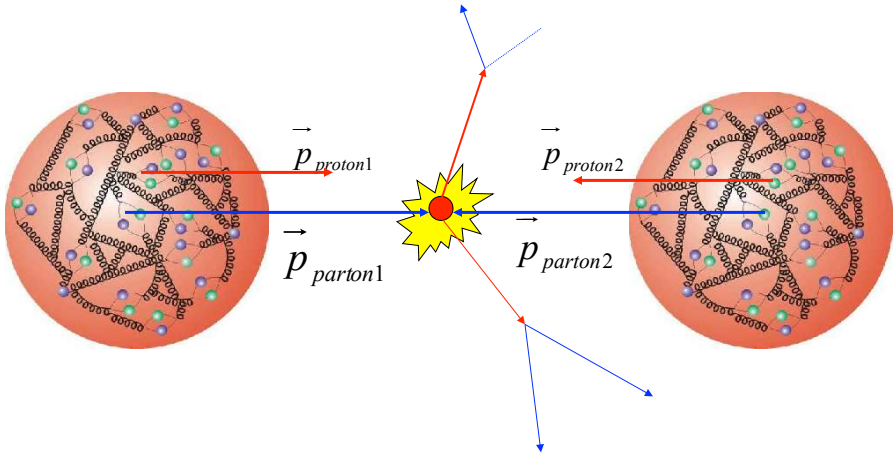

Figure 2.5: A typical proton-proton collision in a hadron collider.

ambiguity to identify real particles from the hadron collision and particles that come from cosmic rays. In order to avoid this effect, we require that the events must occur in time with the bunch crossings as well as selecting only particles which have originated from the measured primary vertex. Since it is impossible to create a complete vacuum within the LHC, there will always be backgrounds from beam halo and cavern backgrounds. There will always be a small amount of particles present which may interact with the proton beams to falsely produce a signal in the detector. However, this is a very small effect and it can be suppressed in the same way cosmic ray backgrounds are reduced.

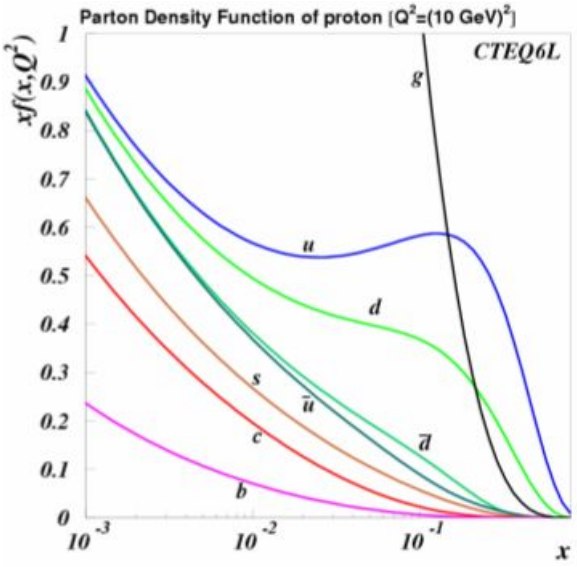

Figure 2.6: Parton distribution of proton.

2.6.2 Current limits on Higgs boson production cross-section

There are many possible ways to search for the Higgs boson experimentally at the LHC depending on the different decay channels of Higgs boson into it's final state objects. The expected production cross section for the Higgs boson is shown in Figure 2.8

For this thesis, a search is performed in $H \to WW^* \to \ell\nu jj$ using $gg \to H$ as shown in Figure 2.10 (gluon-gluon fusion, ggF) production mechanism. Table ?? shows the production cross section for the Standard Model Higgs boson production and the branching ratio (BR) for $H \to WW^* \to \ell\nu jj(\ell = e/\mu)$ as a function of m_H.

There are also many other ways the Higgs boson may decay. The Higgs boson couples to all massive particles. It may decay to any massive particle in

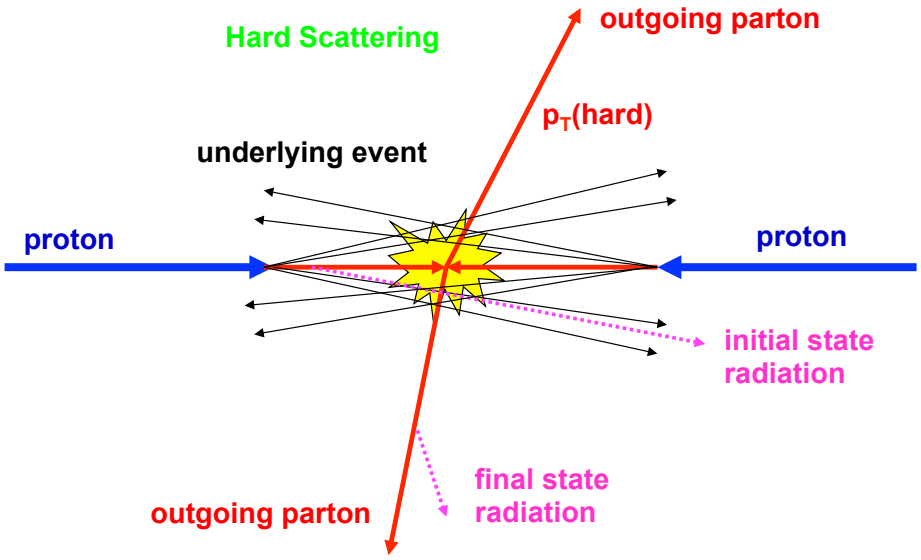

Figure 2.7: A typical hard scattering process in hadron collider.

m_H[GeV]	$\sigma(gg \to H)$ [pb]	$\sigma(qq \to H)$ [pb]	BR($H \to \ell^{\pm}\nu jj$)
300	2.4±0.4	$0.30^{+0.014}_{-0.008}$	0.202
400	$2.0^{+0.31}_{-0.34}$	$0.162^{+0.010}_{-0.005}$	0.170
500	0.85±0.15	$0.095^{+0.0068}_{-0.0032}$	0.160
600	$0.33^{+0.063}_{-0.058}$	$0.058^{+0.005}_{-0.002}$	0.164

Table 2.2: Cross section for Standard Model Higgs boson production and the branching ratio (BR) for $H \to WW^* \to \ell\nu jj$ ($\ell = e/\mu$) as a function of mass [13].

accordance to the conservation laws of the SM. For a given Higgs boson mass, m_H, its couplings to fermions and gauge bosons are fixed. Therefore, production cross sections, decay widths and branching ratios of the Higgs boson can be calculated. Figure 2.8 shows the branching ratios of the Higgs boson to various final states as a function of m_H and Figure 2.9 shows the total width of the Higgs boson.

Figure 2.8 shows that at high Higgs mass m_H, the Higgs boson decays dominantly to pairs of W bosons or to pairs of Z bosons. In the mode $H \to ZZ \to 4\ell$, the Higgs boson mass may be fully reconstructed. However, the low branching ratio of $H \to ZZ \to 4\ell$ leads to a low overall cross section so a significant amount of data must be analysed to obtain a signal.

The cross section for the basic gluon gluon fusion to Higgs process can be found in Appendix B

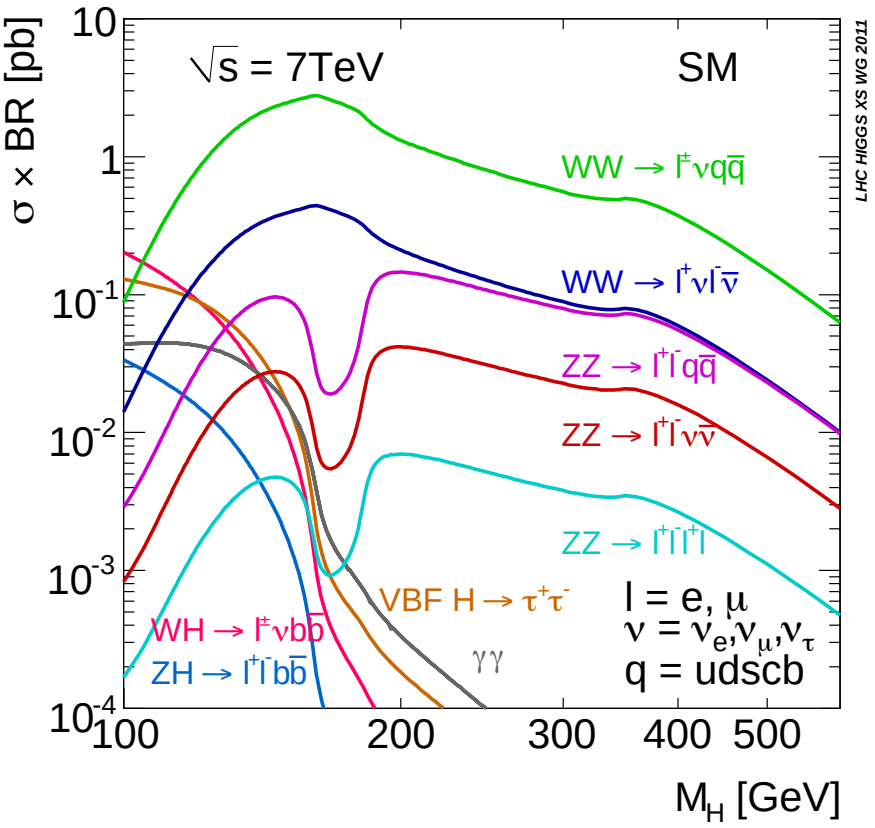

Figure 2.8: The Standard Model Higgs boson cross-section [13].

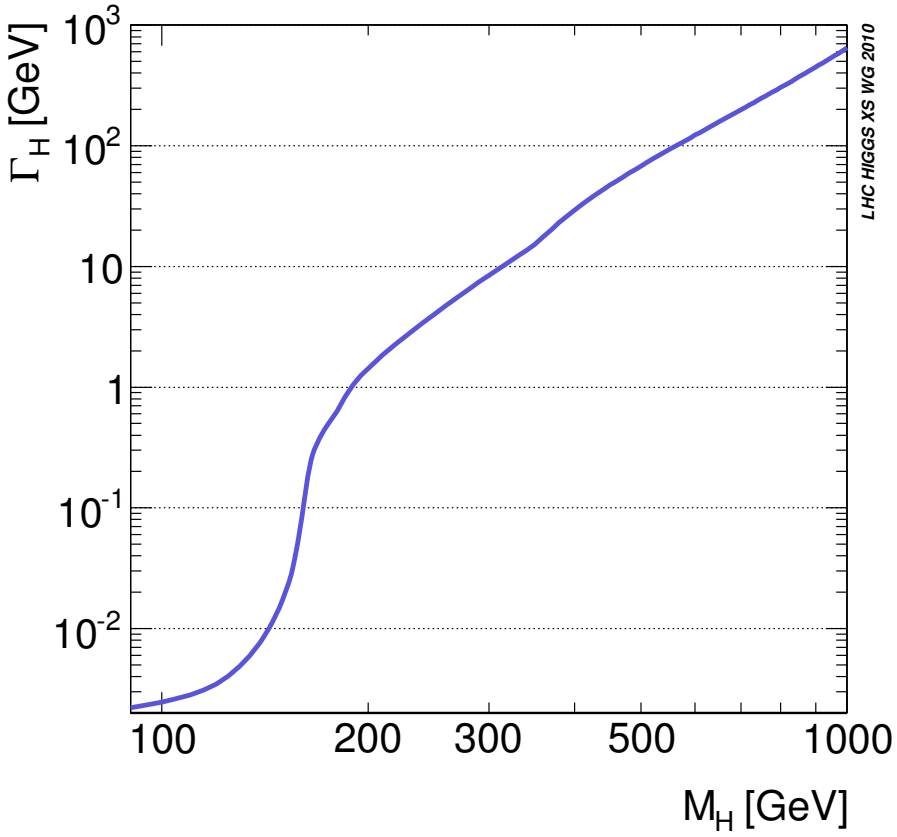

Figure 2.9: Total width of the Standard Model Higgs boson [13].

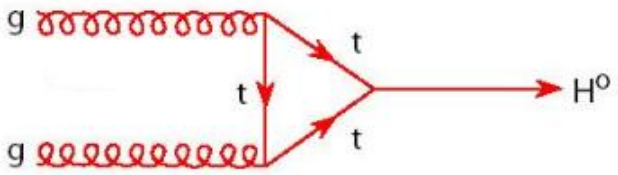

Figure 2.10: Gluon-gluon fusion [14].

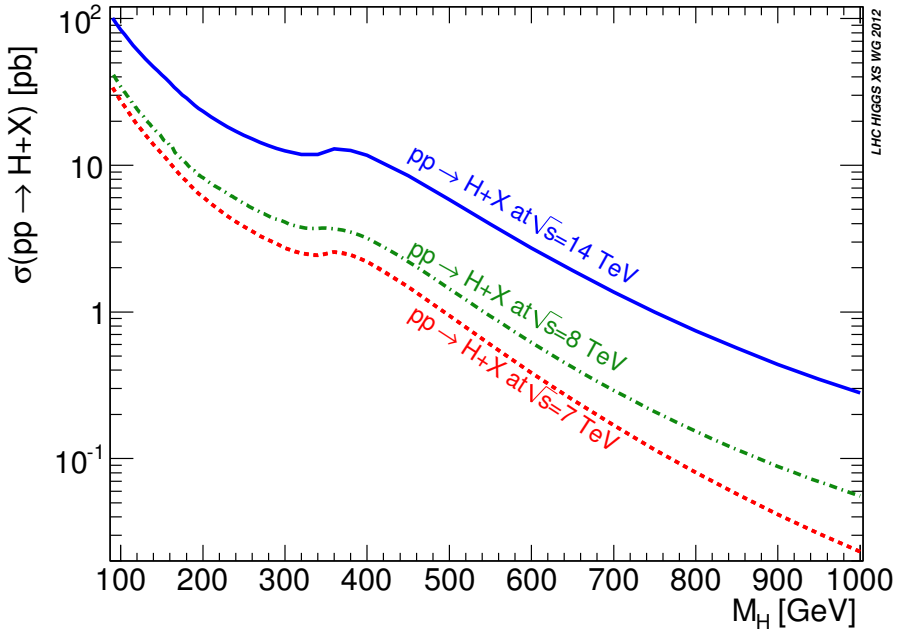

Figure 2.11: Total production cross-section of Higgs boson at $\sqrt{s} = 7, 8, 14$ TeV [13].

2.7 $H \to WW^* \to \ell\nu jj$ Analysis

This thesis work is the extension of the previous work by using 1.04 fb^{-1} of data (data recorded by the ATLAS detector until July 2011) at $\sqrt{s} = 7$ TeV which was presented in "The XXV International Symposium on Lepton Photon Interactions at High Energies (Lepton Photon 11)" [15], [16], Appendix A. We subsequently published the result in Nov. 2011 [17]. We collected data for few more months until Dec 2011 where we received 4.7 fb^{-1} and we published the result in 2012 [18]. A search for a SM Higgs boson was done in this thesis using 4.7 fb^{-1} at $\sqrt{s} = 7$ TeV in the $H \to WW^* \to \ell\nu jj$ decay channel. An ATLAS internal document related to this thesis and the published result can be found here [19].

Chapter 3

Large Hadron Collider and The ATLAS Detector

3.1 The Large Hadron Collider

The Large Hadron Collider (LHC) [20] located just outside Geneva, Switzerland, beneath the French-Swiss border, is the world's most powerful tool for frontline research in particle physics. It is designed to collide protons at a centre of mass energy ($\sqrt{s}$) of 14 TeV once it has been fully commissioned. Commissioning began in September 2008 and the highest energy collisions to date have been at a centre of mass energy of 8 TeV. For this thesis, data collected at $\sqrt{s} = 7$ TeV in 2011 will be considered.

The LHC is installed in a circular tunnel, 26.7 km in circumference, which was initially constructed for the Large Electron Positron (LEP) collider. Figure 3.1 is a schematic diagram of the LHC. Two general purpose detectors designed to search for physics beyond the Standard Model, A Toroidal LHC ApparatuS (ATLAS) [21] and the Compact Muon Solenoid Experiment (CMS) [22] are located at Point 1 and Point 5, respectively. Two smaller specialised experiments, A Large Ion Collider Experiment (ALICE) [23], investigates quark-plasma soup in the lead-lead nuclei collisions, and the Large Hadron Collider Beauty Experiment (LHCb) [24], designed to study physics using bottom quarks (b), are located

at Point 2 and Point 8, respectively. Points 3 and 7 contain equipment used for beam cleaning, Point 4 contains radio-frequency cavities and Point 6 is the location of the beam dump.

Two proton beams travel in opposite directions around the ring. Therefore the two beams need independent magnet systems, because the particles in the beams have the same charge[1]. The 3.7 m diameter of curved sections of the tunnel is not large enough to contain two completely separate rings, therefore a twin-bore magnet system was designed in which the two rings share the same cold mass. Particle physics experiments need accelerators that can produce collisions at the highest possible rate at the highest possible energy in order to maximise the discovery potential for new physics. The number of events of a interesting signal process is determined by:

$$N_{event} = L \times \sigma_{event} \tag{3.1}$$

where L is the luminosity of the accelerator, in number of particles per unit area per unit time, and σ is the cross-section, or interaction probability. So, the study of rare processes with low cross-sections requires the highest possible luminosity. The luminosity depends on the parameters of the proton beam and

[1]This is in contrast to the Tevatron collider at Fermilab, which used to collide protons and anti-protons. Since proton and anti-proton have opposite charge and move in the opposite direction, both beams require a magnetic field in the same orientation. A different choice was made for the LHC to avoid the technical challenges in producing and storing antiprotons.

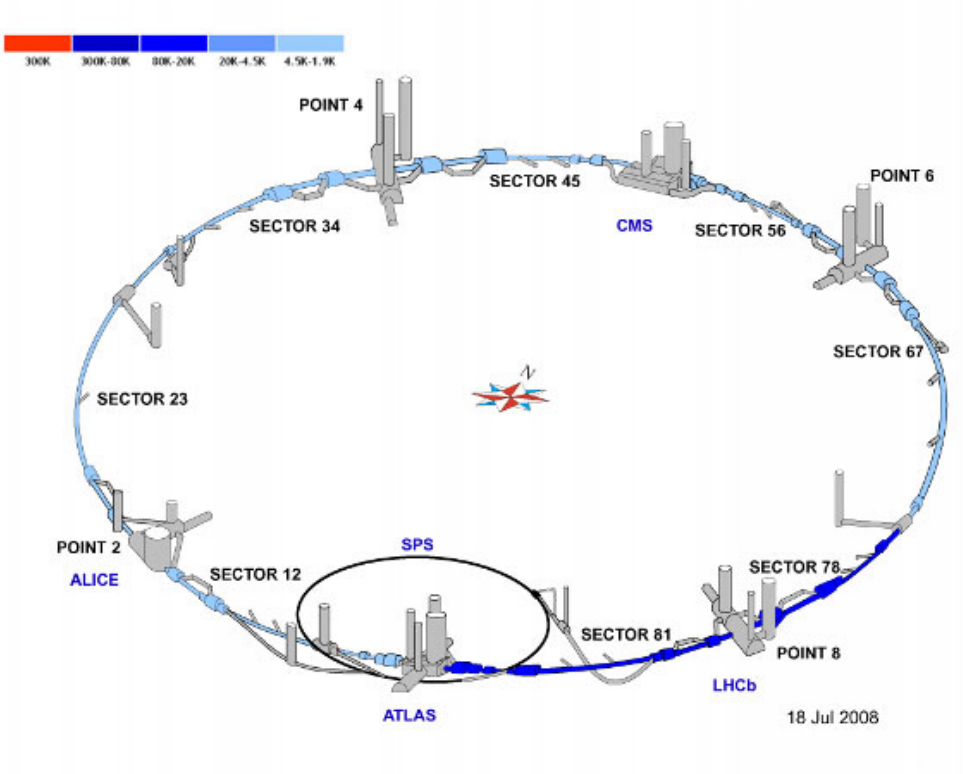

Figure 3.1: The Large Hadron Collider (LHC) [21].

Figure 3.2: Author is in tunnel of the Large Hadron Collider.

can be written as:

$$L = \frac{N_b^2 n_b f_{rev} \gamma_r}{4\pi\sigma_x\sigma_y} \tag{3.2}$$

where

- N_b is the number of particles per bunch
- n_b is the number of bunches per beam
- f_{rev} is the frequency at which the beams circulate the ring
- γ_r is the relativistic gamma-factor
- σ_x, σ_y represent the width of the beam in the transverse direction where the shape is assumed to be approximated by a Gaussian distribution

The LHC has been designed for a luminosity of 10^{34} $/cm^2 s$. Safe commissioning of the LHC requires slowly increasing the collision energy and the luminosity. At present the highest instantaneous luminosity is $5.1 \times 10^{32} / cm^2 s$. The luminosity was increased by increasing the number of particles per bunch by an order of magnitude, the number of bunches per beam, and by decreasing the transverse width of the beam at the interaction points.

The cross-sections of many physics processes increase with the proton beam energy. The energy at which particles in the proton beam collide is determined

by

$$B\rho = \frac{p}{e} \tag{3.3}$$

where B is the field of the dipole magnets used to bend the proton beam around the ring, ρ is the bending radius, p is the proton momentum and e is the proton charge. For a fixed accelerator size, the maximum energy is limited by the magnetic field of the dipoles. An energy of 7 TeV per proton in the LHC requires a high magnetic field in the dipoles of 8.33 T. Such an extreme magnetic field is obtained by using superconducting dipole magnets, which operate at a temperature of 1.9 K. For the dipoles, it takes ∼six weeks to be cooled from room temperature to 1.9 K. In addition to the 1232 dipole magnets, 392 quadrupole magnets are used to focus the beams.

The first proton-proton beam was injected in the LHC on the 10^{th} September 2008. Unfortunately, just over a week later on 19^{th} September, during powering tests of the main dipole circuit of Sector 3-4 of the LHC, a fault occurred in the electrical bus connection between a dipole and a quadrupole magnet. Few magnets underwent mechanical damage and a significant amount of helium was released into the LHC tunnel. This incident delayed in the LHC operation of more than a year while the magnets were repaired and a system was developed to detect abnormal electrical resistance in bus bars and the interconnections between magnets.

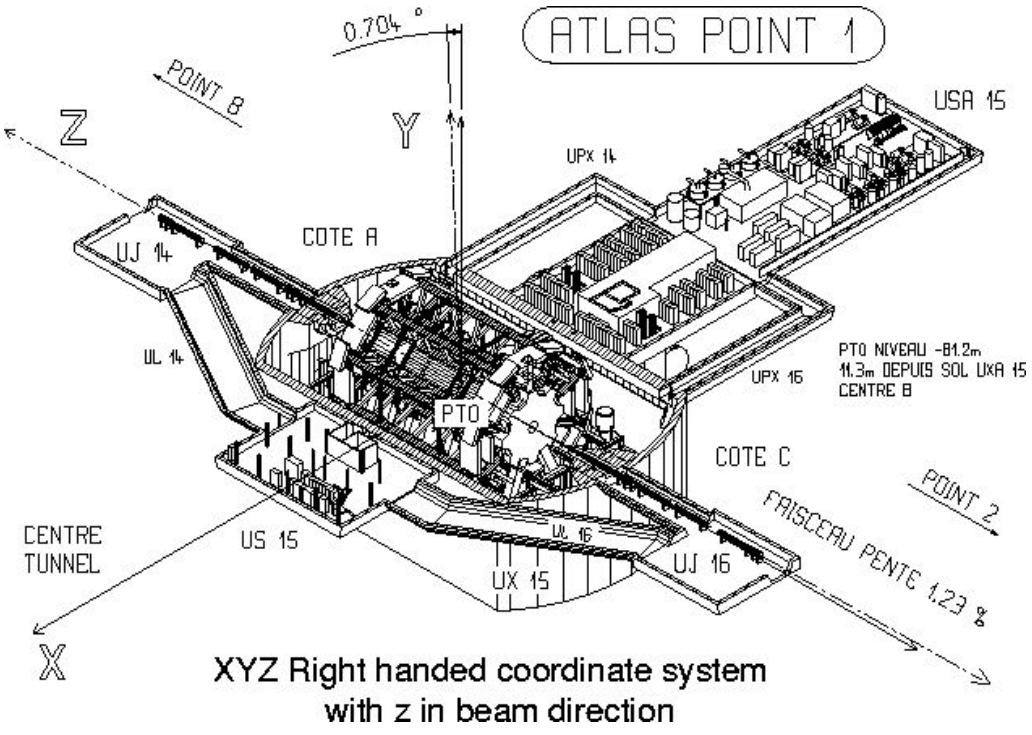

Figure 3.3: The ATLAS Coordinate System [14].

3.2 A Toroidal LHC Apparatus (ATLAS) Detector

ATLAS (A Toroidal LHC ApparatuS) is one of the four multi-purpose high energy physics detectors at the Large Hadron Collider, designed to measure the largest possible variety of physics processes [21]. ATLAS is located 92.5 m below the ground at point 1 of the LHC (CERN site). As shown in Figure 3.4, it is cylindrical in shape, 25 m in diameter, and 44 m long, and it weighs approximately 7000 tons. Many high-resolution subsystem detectors within the ATLAS detector help identification and reconstruction of particles such as electrons, muons, jets and missing transverse energy.

ATLAS is the largest of the four LHC experiments and has been designed to measure a wide range of physics processes. Fast, radiation hard-electronics and sensor elements and high detector granularity are used to cope with the high particle flux from the LHC. ATLAS has full azimuthal coverage and a large acceptance in pseudorapidity. The coordinate system used by ATLAS is discussed in Section 3.2.1. The detector is 44 m long and 25 m high, cylindrical in shape and symmetric about z with respect to the interaction point.

3.2.1 The ATLAS coordinate system and Nomenclature

The coordinate system used within the ATLAS experiment is shown in Figure 3.3. The origin of the coordinate system is defined by the nominal interaction point with the beams traveling in the z-direction as shown in Figure 3.3. The positive

Detector Component	Required resolution	η coverage
Tracking	$\sigma_{p_T}/p_T = 0.05\% p_T \pm 1\%$	± 2.5
EM calorimetry	$\sigma_E/E = 10\%/\sqrt{E} \pm 0.7\%$	± 3.2
Hadronic calorimetry (jets)		
barrel and end-cap	$\sigma_E/E = 50\%/\sqrt{E} \pm 3\%$	± 3.2
forward	$\sigma_E/E = 100\%/\sqrt{E} \pm 10\%$	$3.1 < \lvert\eta\rvert < 4.9$
Muon spectrometer	$\sigma_{p_T}/p_T = 10\%$ at $p_T = 1$ TeV	± 2.7

Table 3.1: Approximate resolution of the different components of the ATLAS detector.

x-axis is defined as pointing towards the centre of the LHC ring from the center of the interaction point and the positive y-axis is pointing upwards, away from the centre of the earth. The azimuthal angle ϕ is measured around the beam axis in the x-y plane and the polar angle θ is the angle from the beam axis, i.e., measured between the z-axis and the x-y plane [25].

The partons within two colliding proton beams have wide range of longitudinal momentum determined by parton distribution function (PDF) shown in Figure 2.6. Since we have 7 TeV center of mass energy of the colliding proton beams, the center of mass of the parton-parton collision is longitudinally boosted with respect to the center of mass of the colliding proton. Therefore, we have to find out variables to describe a collision event which are invariant under longitudinal boosts. The rapidity y, the transverse momentum p_T and

the azimuthal angle ϕ are some of those variables.

The four-momentum p^μ of a particle of mass m can be written as

$$p^\mu = \left(\sqrt{p_T^2 + m^2}\cosh(y), p_T \sin\phi, p_T \cos\phi, \sqrt{p_T^2 + m^2}\sinh(y)\right) \tag{3.4}$$

where y is the rapidity, defined as

$$\begin{aligned} y &= \frac{1}{2} \times \ln\left(\frac{E + p_z}{E - p_z}\right) \\ &= -\frac{1}{2}\ln\left(\frac{E - p_z}{E + p_z}\right) \\ &= -\ln\left(\sqrt{\frac{E - p_z}{E + p_z}}\right) \end{aligned} \tag{3.5}$$

where E is the energy of the object and p_z is its momentum along the direction of the incoming proton beams. It is evident from Equation 3.5 that if we have a boost along z-direction, rapidity is going to be additive under Lorentz transformations. However, rapidity differences are Lorentz invariant.

For massless objects, $E = |\overrightarrow{p}|$, we can further simplify y

$$\begin{aligned} y &= -\ln\left(\sqrt{\frac{|\overrightarrow{p}| - p_z}{|\overrightarrow{p}| + p_z}}\right) \\ &= -\ln\left(\sqrt{\frac{1 - \frac{p_z}{|\overrightarrow{p}|}}{1 + \frac{p_z}{|\overrightarrow{p}|}}}\right) \\ &= -\ln\left(\sqrt{\frac{1 - \cos(\theta)}{1 + \cos(\theta)}}\right) \end{aligned} \tag{3.6}$$

Therefore,

$$y = -\ln\left(\tan\left(\frac{\theta}{2}\right)\right) \equiv \eta \tag{3.7}$$

where η is the pseudo-rapidity which is easier to measure experimentally because of its relation to the polar angle θ. Rapidity has a more physical meaning for massive objects. Since pseudo-rapidity is the same for all objects (i.e. objects of any mass), it can be used to define the coordinate system in a particle detector instead of using the azimuthal angle θ. Unless otherwise stated, η will is used through out the thesis.

The transverse momentum p_T, the transverse energy E_T, missing transverse energy $E_{\mathrm{T}}^{\mathrm{miss}}$ and other transverse variables, are defined in the x-y plane unless otherwise stated. The distance ΔR in the pseudo-rapidity (η)-azimuthal angle (ϕ) space is defined as $\Delta R = \sqrt{(\Delta\eta)^2 + (\Delta\phi)^2}$.

Trajectories of charged particles in an ideal uniform magnetic field can be described by the following helix parameters, measured at the point of closest approach to the nominal beam axis $x = 0, y = 0$. Parameters in x-y plane are:

- p_T : Transverse momentum with respect to the beam-axis.
- ϕ : Azimuthal angle with $\tan\phi = \frac{p_y}{p_x}$.
- d_0 : Transverse impact parameter, defined as the transverse distance to the beam axis at the point of closest approach.

- z_0 : Longitudinal impact parameter, defined as the z position of the track at the point of closest approach.

3.2.2 Magnet System

ATLAS features a striking hybrid system of four large superconducting magnets. The magnet system is 22 m in diameter and 26 m long and has a total stored energy of 1.6 GJ. A central solenoid provides a 2 T axial magnetic field for the Inner Detector and a barrel toroid and two end-cap toroids provides a toroidal magnetic field of 0.5 T in the barrel and 1 T in the end-caps. The solenoid is a single-layer coil made of a Niobium-Titanium superconductor and is operated at 4.5 K with a current of 7.7 kA. The toroids operate at a temperature of 4.6 K with a current of 20.5 kA. The finite number of coils in the toroids mean that the field is not perfectly toroidal but follows a regular eight fold pattern shown in Figure 3.5 and Figure 3.6. The largest variations in the field strength are in the region between the barrel and the end-cap. Accurate knowledge of the magnetic field is vital for precise track measurements, therefore the muon spectrometer is equipped with approximately 1730 Hall cards to measure the magnetic field to an accuracy of 0.3%. The design of the ATLAS magnet system is significantly different to the single 4 T solenoid used by CMS. The choice of design for the magnet system, once made, was the driving force behind the further choices in the detector design.

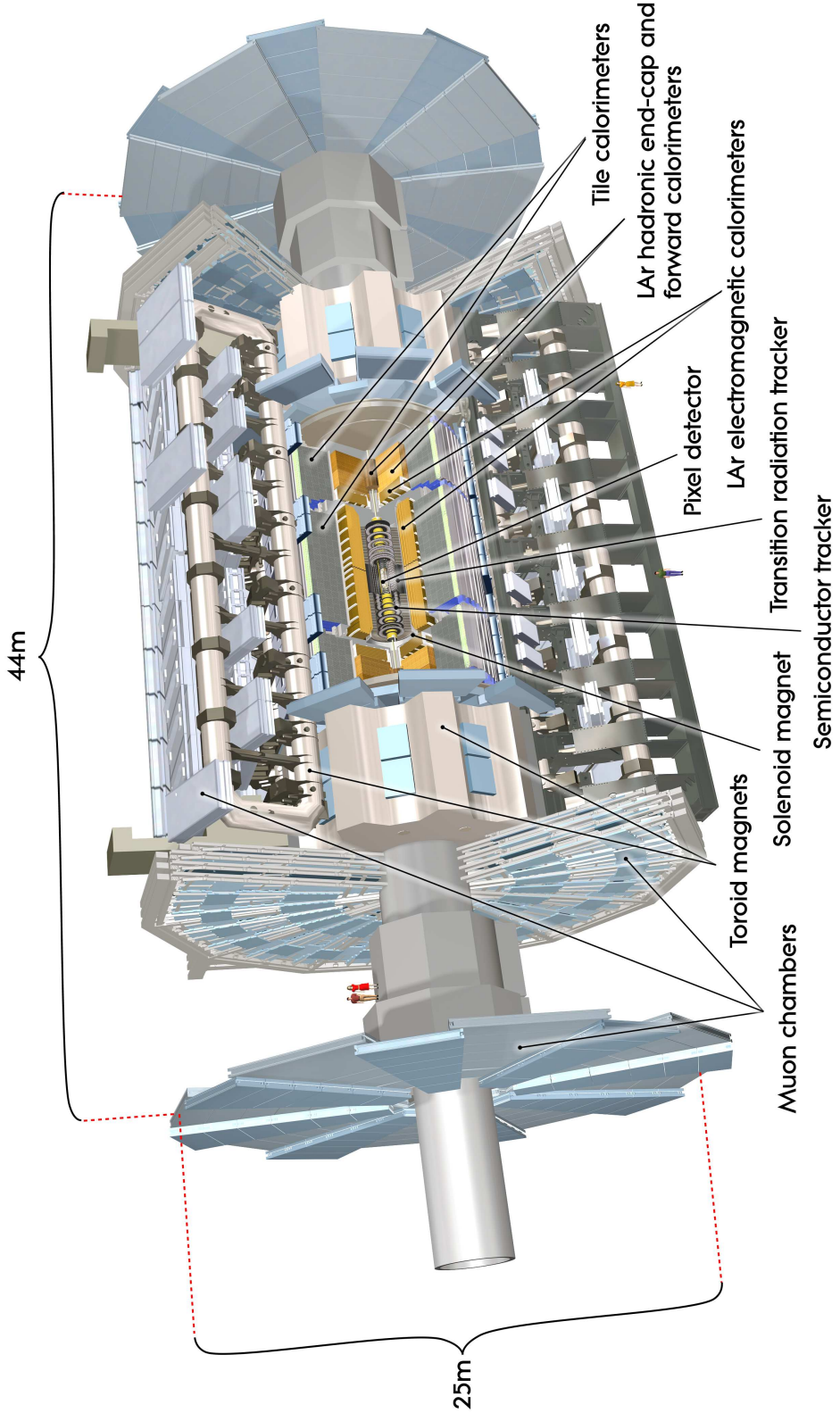

Figure 3.4: The ATLAS detector [21].

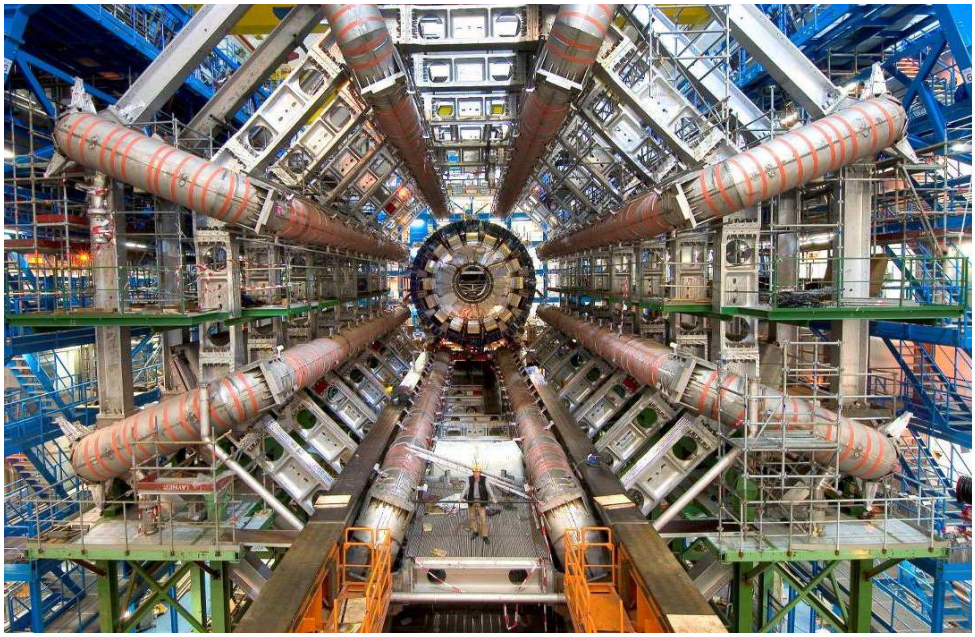

Figure 3.5: The Barrel Toroid assembled from eight coils and sixteen supporting rings linking the coils. The length is 25.3 m, the inner diameter is 9.4 m and the outer diameter is 20.1 m. The scale is indicated by the person standing in between the two bottom coils [21].

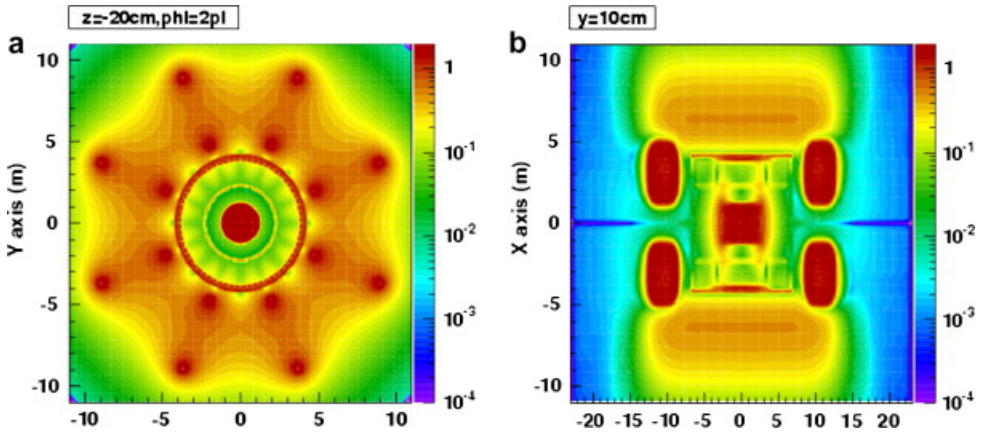

Figure 3.6: Magnetic field configuration in the (a) transverse cross section in the center of the magnet system (thus End Cap Toroid field not present) and (b) longitudinal section. One can clearly recognize the peak magnetic field of 4 T in the windings of the eight Barrel Toroid coils (in a) and both End Cap Toroids (in b); the 2 T in the Central Solenoid and in the iron shell, part of the calorimeter, surrounding the solenoid and acting as a return yoke (in a) [26].

3.2.3 Inner detector

The function of the inner detector (ID) is primarily to provide excellent momentum resolution and precision pattern recognition, providing the ability to reconstruct both primary and secondary vertices. Charged particles within the region $|\eta| < 2.5$ leave hits as they traverse the ID. Multiple hits may be joined up to reconstruct the path of a charged particle through the volume of the ID, from which the momentum and origin of the particle may be calculated. In order to accurately reconstruct these charged particle tracks, fine granularity detectors are required. Within ATLAS, pixel and silicon microstrip tracking detectors, as well as the transition radiation tracker (TRT), are used to achieve the required accuracy. Figure 3.7 shows the three sub-detectors of the Inner Detector: the silicon pixel detector, semiconductor tracker (SCT) and the Transition Radiation Tracker (TRT). As the solenoid deflects particles in the transverse plane, each sub-detector has the highest precision in this plane to obtain the best possible momentum measurement. Figure 3.8 shows an ATLAS pixel module.

Silicon detector measures the passage of charged particles to very high spatial precision. Therefore, they should be placed close to the interaction point where the particle density is the highest. Since the first layer of the silicon detector is very close to the interaction point, it has better track parameter resolution but it experiences higher radiation dose. Therefore the optimal detector placement involves balancing the performance of the detector and the detector lifetime.

The pixel detector is built directly onto the beryllium beam pipe in order to provide the best possible primary and secondary vertex resolution. It comprises three layers in the barrel at radii of 50.5 mm, 88.5 mm, and 122.5 mm, and three end-cap disks on either side of the center at positions $|z| = 495$ mm, 580 mm, and 650 mm. The 250 μm thick silicon sensor modules are divided into 50 μm wide and 400 μm long pixels, with 47232 pixels on each of the 1744 modules. With over 80 million pixels, the pixel detector makes up almost 90% of the total read out channels of the ATLAS detector. A typical track with $|\eta| < 2.5$ will leave 3-4 hits in the pixel detector.

The pixel sensors are essentially doped semiconductors with a high reverse bias voltage. When an ionising particle (i.e., charged pion or a muon) propagates through a silicon detector, it ionises the silicon atoms and produces pairs of electrons and holes along its trajectory. The number of electron-hole pairs produced along its trajectory is proportional to the energy lost by the particle. Electrons and holes move in opposite directions and reach to the sensor surface due to the external applied electric field. The charge drifts to the surface and produces a pulse of current, which is being detected using charge sensitive electronics. A typical minimum ionizing particle passing through the sensor module will free 2×10^4 electrons. To reduce the number of hits coming from electronics noise, this analog signal is compared to a threshold and the time over threshold is recorded. In some cases several neighboring pixels may register a signal above threshold. These pixels are grouped into a single 'cluster', which

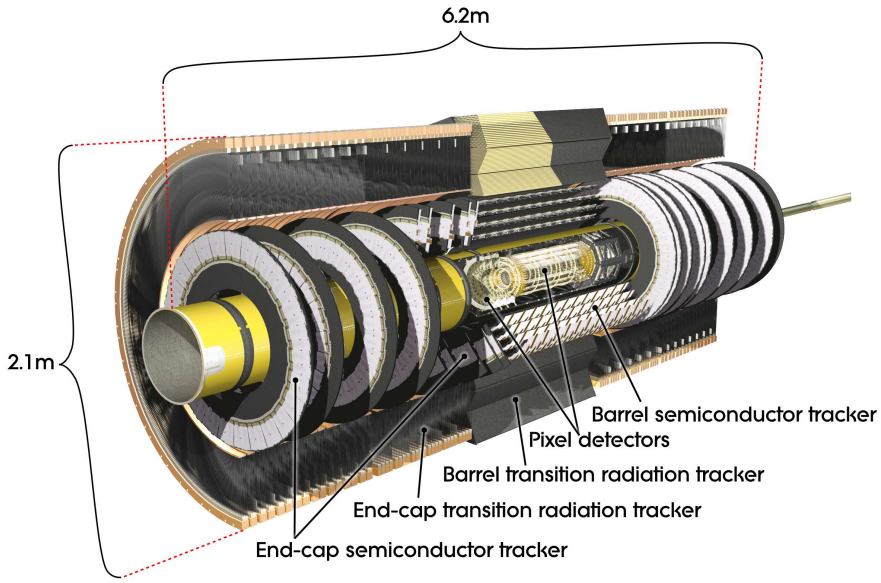

Figure 3.7: ATLAS inner detector system [21].

is treated as a single hit by the track reconstruction software. Clusters from noise typically have low time over threshold ($\sim$ 125 ns), whereas clusters from a typical minimum ionizing charged particles are expected to have a time over threshold of $\sim$ 750 ns. Within the geometric acceptance of the pixel detector, the hit efficiency was more than 99%, but 2.5% of the modules in the detector were disabled during data-taking.

Semiconductor tracker (SCT), lying immediately outside the pixel detector, consists of silicon strips. Conceptually the SCT is similar to the pixel detector, but it uses 80 μm wide, 12 cm long silicon microstrips rather than pixels. The entire SCT detector comprises 15912 sensor modules in four radial layers in the barrel, with radii of 299 mm, 371 mm, 443 mm, and 514 mm, and six end-cap

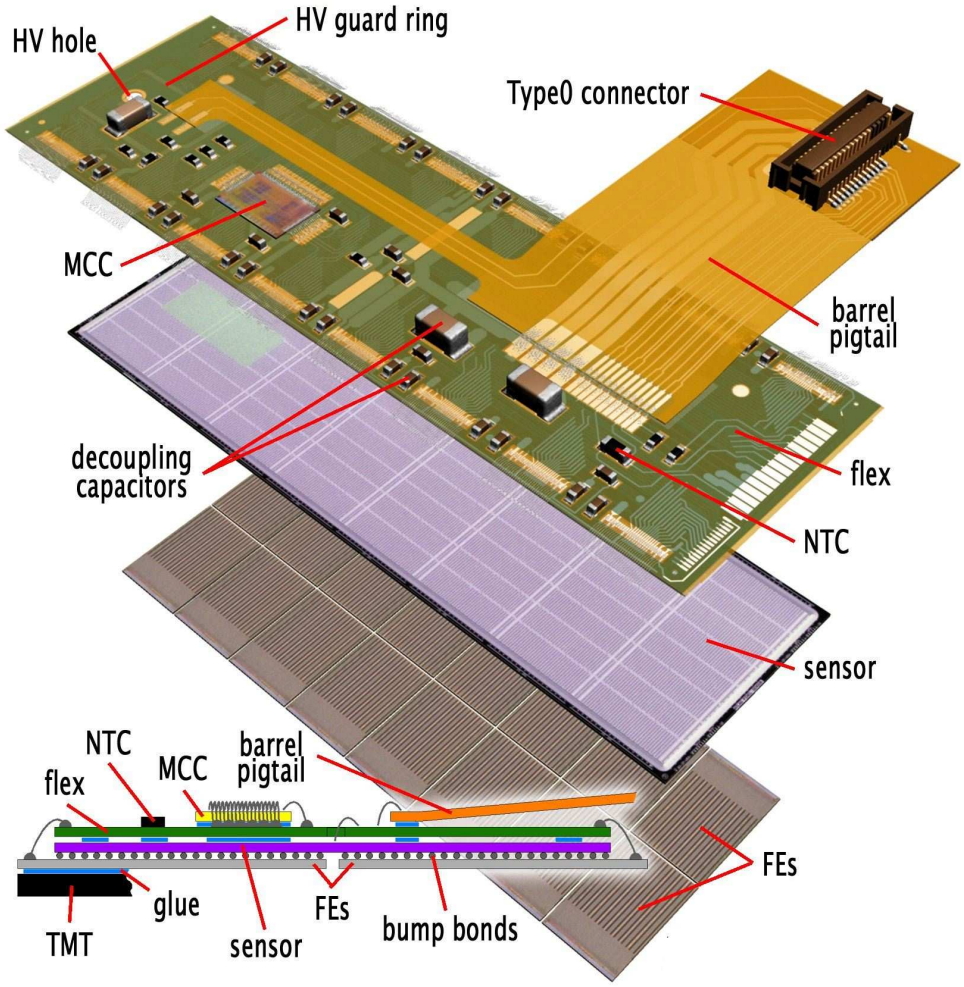

Figure 3.8: Schematic view of a barrel pixel module (top) illustrating the major pixel hybrid and sensor elements, including the MCC (module-control chip), the front-end (FE) chips, the NTC thermistors, the high-voltage (HV) elements and the Type0 signal connector. Also shown (middle) is a plan view showing the bump-bonding of the silicon pixel sensors to the polyimide electronics substrate. The photograph at the bottom shows a barrel pixel module [21].

disks on either side of the interaction point at $|z| = 890$ mm, 1091 mm, 1350 mm, 1771 mm, 2115 mm, and 2608 mm. The four barrel layers, as well as the first, third, and sixth disks are all "double-layers". For detectors that are strip-like, this double-layering is a common method to improve the spatial resolution in the long dimension. The angle between the two layers is optimized for resolving "ghost" ambiguities when several charged particles traverse one double-layer [21]. The single-hit efficiency for the SCT is quite high and only 0.97% of the modules were disabled during data-taking.

The final part of the ID is the transition radiation tracker (TRT), also known as "straw tube tracker". This is made up of cylindrical polyimide drift tubes (straws) with a diameter of 4 mm straws filled with a mixture of CO_2 and xenon. The straws contain a gold wire at their center. The straws act as the cathode and gold wire acts as anode of a drift tube and passes through the center of the straw. As charged particles pass through the straws, they ionize some of the gas. A high voltage is applied across the straw, so that the charge is collected on the anode after some drift time. The drift time provides precise measurement of the impact parameter of the track in the tube, but there is no resolution in the direction parallel to the wire. Charged particles passing through the straw tubes also emit low-energy transition radiation photons which are absorbed by the gas. This transition radiation provides discrimination between electrons and hadrons.

Both the pixels and SCT detectors are cooled to $\sim -10\,^{\circ}\mathrm{C}$ using C_3F_8 as the coolant. The cooling is necessary inorder to reduce the radiation damage to the

silicon. Because the TRT operates at room temperature, a set of insulators and heaters isolate the silicon detectors from the environment of rest of the ATLAS detector. In order to prevent condensation, dry nitrogen is blown through the cooled portion of the inner detector (pixels and SCT). The TRT is operated in a dry CO2 environment since nitrogen can reduce the transition radiation signal in the TRT .

Beam conditions monitor (BCM) is attached next to the pixel system to detect the surge of charge. The BCM consists of eight diamond sensors 184 mm on either side of the interaction point. These sensors have very good time resolution. Thus it is able to distinguish particles arriving from the collision point and those arriving along the beam line. In the case of a beam incident, a dangerously high flux of particles could be sent through ATLAS. The BCM detects the high flux of particles that are not coming from the collision point and triggers the dump of the LHC beams. Once a beam dump signal has been sent, the beam is completely ejected from the main ring of the LHC in about three turns ($\sim 250\ \mu$ s). BCM is the only subdetector in ATLAS that is allowed to trigger a beam dump automatically.

3.2.4 Calorimeter

The ATLAS calorimeters (shown in Figure 3.9) cover the range $|\eta| < 4.9$ and provide precise measurement of the energy of electrons, photons and hadrons using an electromagnetic calorimeter for electron and photon reconstruction

and a hadronic calorimeter to improve the measurement of jets and $E_{\mathrm{T}}^{\mathrm{miss}}$. A forward calorimeter (FCal) is used for particles at $3.1 < |\eta| < 4.9$.

All of the ATLAS calorimeters are sampling calorimeters. Sampling calorimeters consist of sheets of absorbers alternated with layers of active material to perform the energy measurement of the incident particles. The incident particle on the calorimeter produces a shower of particles. At each stage in the showering, the particles will have less and less energy until the shower is completely absorbed. Energy of the incident particles is deposited within the calorimeter components which may be summed to provide a measurement of the energy of the of the incident particle. The calorimeter is designed to absorb completely the energy of the incident particles so that no energy is lost by escaping particles. This helps to reduce the radiation damage to the muon chambers due to high energy hadrons.

The first part of the calorimeter system is the **liquid argon (LAr) electromagnetic (EM) calorimeter**, which measures the energy of incoming electrons and photons. It provides coverage up to $|\eta| < 3.2$ and is split into a barrel part within $|\eta| < 1.475$ and two endcap parts for the remaining coverage. The active material within the calorimeter is liquid argon, while lead helps to absorb electrons and photons. The thickness of lead in the absorber plates is optimised as a function of $|\eta|$ to provide the best energy resolution. By using a presampler detector consisting of an active LAr layer within the central region of $|\eta| < 1.8$, the energy lost by electrons and photons before reaching the calorimeter is

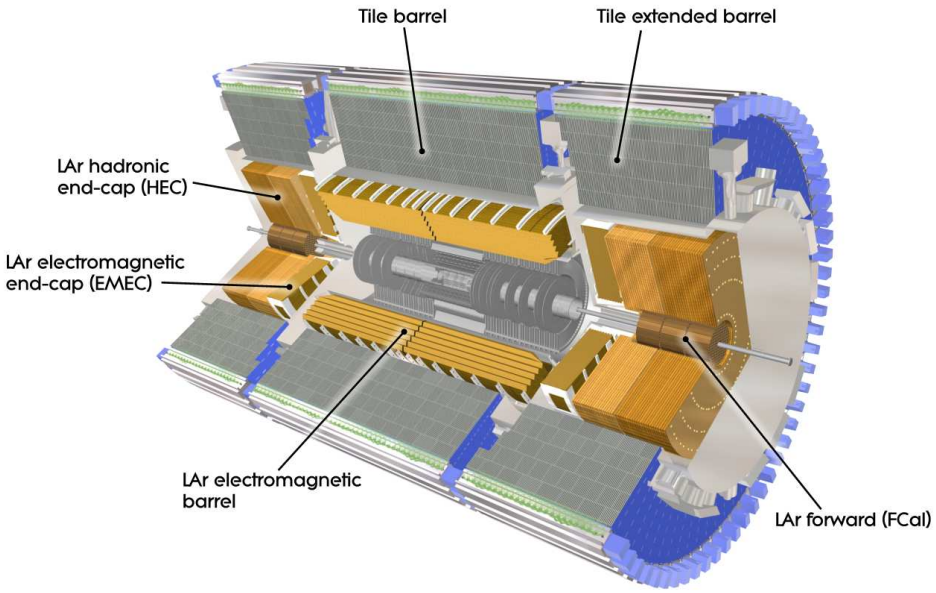

Figure 3.9: Cut-away view of the ATLAS calorimeter system [21].

corrected.

Directly outside the EM calorimeter are the **hadronic calorimeters**, which are designed to determine precisely the energy of hadrons. The hadronic calorimeters consist of the **tile calorimeter** which uses steel as the absorber and **scintillating tiles** as the active material and it covers $|\eta| < 1.7$. Additional coverage up to $|\eta| < 3.2$ is provided by the **LAr hadronic endcap calorimeter**. The **LAr forward calorimeter**, uses the same technology as the EM calorimeter, gives coverage in the very forward region which extends to $|\eta| < 4.9$. Figure 3.9 shows cut-away view of the ATLAS calorimeter system.

Both the LAr and the scintillating tile calorimeter measure the energy of particle showers. Particles passing through the LAr calorimeter ionize the liquid

argon. A high voltage is applied across the liquid argon, and the charge deposition is collected as a current in the cell. Because the LAr flows continuously, there is no reduction in the signal strength due to the radiation damage over the lifetime of the LHC. Scintillation light is produced in the tiles as they absorb radiation. The tiles signal is transferred through optical fibers to **photomultiplier tubes (PMTs)** located behind the active volume of the calorimeter. Due to radiation damage, the signal from the scintillating tiles is expected to decrease by several percent over the lifetime of the LHC. For calibration between runs, cesium sources can scan across the detector to check its response (the ratio of the reconstructed signal to the "true" signal). Charge can be injected into a single cell to test and calibrate the read-out electronics. Lasers can provide light to test the optical connections and PMT response.

3.2.5 Muon system

The muon spectrometer (Figure 3.10) is the outermost component of the ATLAS detector which surrounds the calorimeters. It is a high precision tracking detector designed to detect and measure the momentum of charged particles in the pseudorapidity range of $|\eta| < 2.7$. Due to the structure of the toroidal magnet system, the spectrometer follows an eight-fold azimuthal symmetry. Muon momenta up to ~ 3 TeV can be measured using the muon spectrometer alone.

The momentum is measured using the magnetic deflection of muons by the

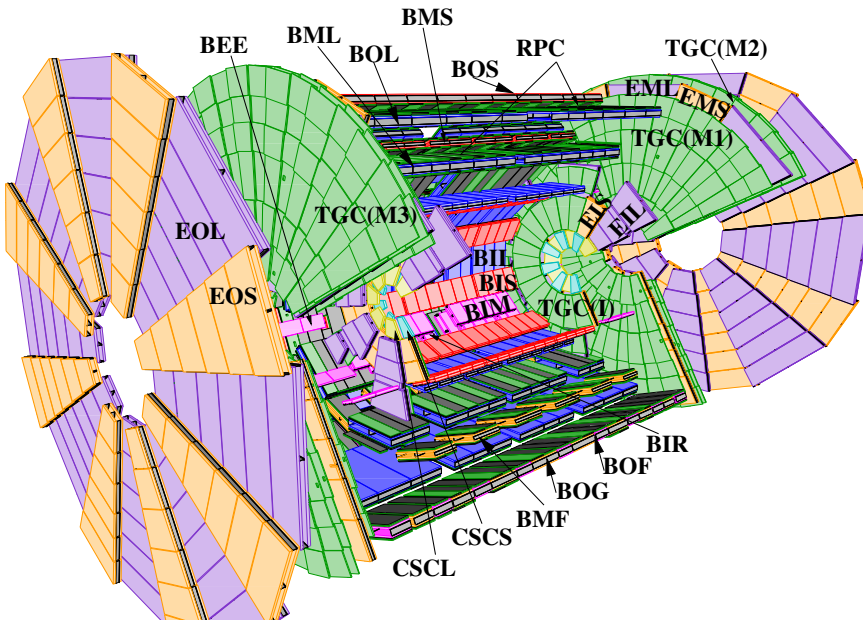

Figure 3.10: Configuration of the muon spectrometer with its four chamber sub-systems: the precision-measurement tracking chambers (MDTs and CSCs) and the trigger chambers (RPCs and TGCs). The first letter (B and E) of the MDT naming scheme refers to barrel and end-cap chambers, respectively. The second and third letters refer to layer (inner, middle, and outer) and sector (large and small) types, respectively [21].

large superconducting toroid magnets. The magnet configuration provides a field orthogonal to the muon trajectories. The three layers of chambers in the barrel are arranged concentrically around the beam axis and the three planes of chambers in the end-caps are perpendicular to the beam axis.

The **Monitored Drift Tubes (MDTs)** provide precision tracking for $|\eta| < 2.7$. An MDT is a gas filled aluminium tube with a tungsten wire at the centre. A single aluminium tube has a radial resolution of 80 μm, but no longitudinal measurement. An MDT chamber consists of between three and eight layers of drift tubes so that an average resolution of ~ 35 μm per chamber is obtained. In the forward regions with $2.0 < |\eta| < 2.7$, the innermost MDT layer was replaced by **Cathode Strip Chambers (CSCs)** because they have finer granularity and a 7 ns timing resolution for the higher track density. The CSCs are muliti-wire proportional chambers with the cathode planes divided into strips in orthogonal directions. The resolution of CSC chamber is 40 μm in the plane in which the tracks are bent by the magnetic field and 5 mm in the plane in the transverse direction. Both the MDTs and the CSCs use an Ar/CO_2 gas mixture.

The **muon trigger chambers** provide a momentum-dependent muon trigger. **Resistive Plate Chambers (RPCs)** are used in the barrel for $|\eta| < 1.05$ and **Thin Gap Chambers (TGCs)** are used in the end-cap for $1.05 < |\eta| < 2.4$. The RPCs consist of four Bakelite plates filled with a gas mixture of 97% tetrafluorethane ($C_2H_2F_2$) and 3% isobutane (C_4H_{10}). The RPCs have a spatial resolution of 10 mm and a timing resolution of 1.5 ns. The TGCs are similar to

multi-wire proportional chambers, but with an anode pitch much larger than the distance between the cathode and the anode. The TGCs are mostly used in the end-caps because they can handle high rates with better resolution than the RPCs. TGCs use Carbon dioxide (CO_2) and n-pentane (n-C_5H_{12}) as gas mixtures. The spatial resolution of the TGC is 2-6 mm and the timing resolution is 4 ns. The RPCs were used in the barrel because they were less expensive compared to TGCs and are sufficient to trigger on the lower muon flux. In total, there are 339k MDT, 30.7k CSC, 359k RPC and 318k TGC chambers in the muon spectrometer system.

3.3 Data Acquisition System and Trigger

At even moderate luminosities in the LHC, protons will collide in ATLAS every 25 ns. About 100 million channels in the ATLAS detector must be read out by the data acquisition (DAQ) software during LHC operation, resulting in $\sim$ 1.5 MB of events. Without any filtering, ATLAS would need to process and record $\sim$ 60 TB of data every second. Because only a small fraction of the events can be recorded, these events must be quickly searched for interesting signatures. This presents a significant challenge to the ATLAS trigger and data acquisition system. A rapid decision must be made for each event making sure that we are not throwing any interesting events.

The rate at which ATLAS can record events is actually limited by its ability

to transfer the events away from point 1 at CERN site. A steady transfer can be maintained at ∼700 MB/s from point 1 to the data processing center at CERN (Tier0), implying an ideal output rate of ∼400 Hz. At Tier0, there is sufficient computing power to process 200 Hz of data with the LHC providing collisions ∼70% of the time. Using on-site buffering capability, ATLAS can write at the normal rate of 200 Hz for up to 24 hours without any connection to the Tier0. If ATLAS were to record a float (eight bytes) for every channel in the detector, each event would require ∼800 MB of disk space. To make minimum disk space use, most detectors apply zero-suppression (only reading out channels with a signal above some threshold). For pixel detector, the expected number of hits per event is six orders of magnitude lower than the number of channels in the detector. This zero-suppression can be disabled for special runs, for example to understand data acquisition problems or monitor detector noise below threshold.

As shown in Figure 3.11 the ATLAS trigger system consists of three stages: the hardware-based **Level 1 (L1)** trigger and the **software-based Level 2 (L2)** and **Event Filter (EF)** triggers. L2 and EF triggers collectively known as the High Level Trigger (HLT).

The L1 trigger is designed to make a decision on each event in under 2.5 μs and provide output at a rate up to 75 kHz. No inner detector information is used at this stage, and only very simple calorimetric and muon reconstruction information is available. The L1 trigger selects events containing specific physics objects in the regions of interest (**RoIs**) of the detector. For events with

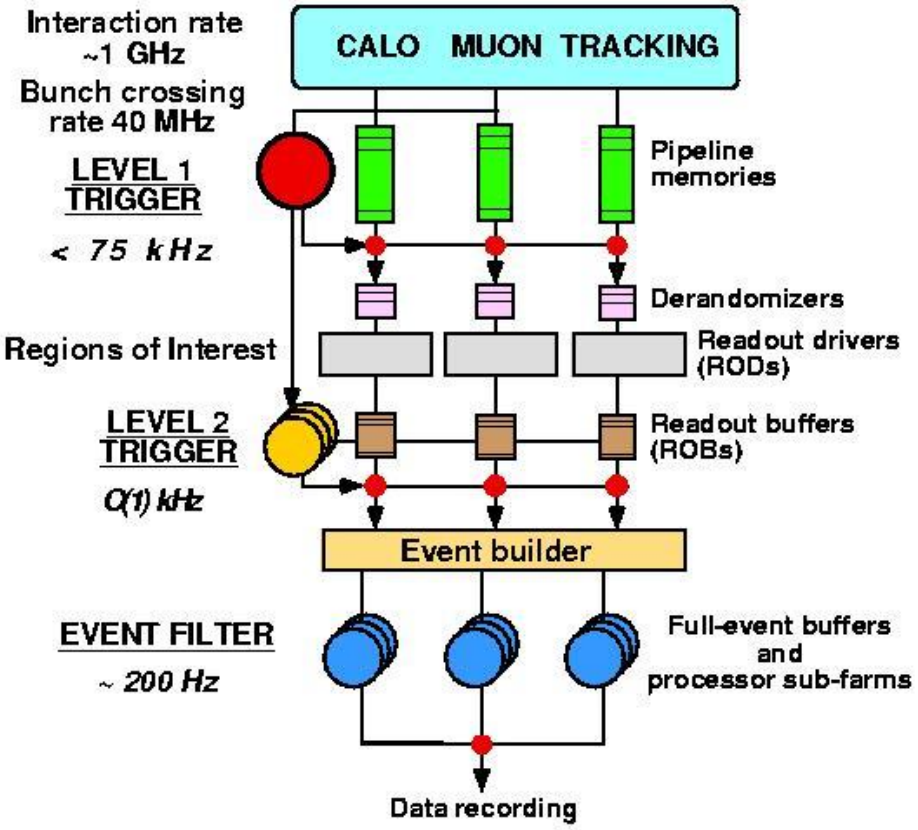

Figure 3.11: The ATLAS Trigger System [27].

electromagnetic clusters, the E_T is measured at L1 by trigger towers in a region of 0.1×0.1 in $\Delta\eta \times \Delta\phi$. These towers are shown in Figure 3.16. The L1 muon trigger utilises a measurement of particle trajectories made by two parts of the muon detector: the resistive plate chambers (RPCs) in the barrel region and the thin gap chambers (TGCs) in the endcap region. The L1 muon trigger uses different detectors systems from the offline muon detectors. This is because the L1 trigger must make rapid decision about whether an event should be stored or discarded but the MDTs and CSCs, used for offline muon reconstruction, are not fast enough for this purpose. However, the MDTs and CSCs are extremely precise. The RPCs and TGCs used for the L1 muon trigger are less accurate, but it is fast enough to cope with the high bunch crossing rate and it provides a precision which is adequate for trigger purposes. The RoIs identified by the L1 trigger are used to seed L2 trigger. The L2 triggers are designed to make a decision in under 40 ms and provide output at rates up to 3.5 kHz. The L2 triggers run a simplified version of the event reconstruction software in the RoIs defined by the calorimeter and muon systems. Improved selection criteria (such as distinguishing electrons from photons by track matching) and improved calibrations are applied. Some limited identification of b-jets is done and $E_{\mathrm{T}}^{\mathrm{miss}}$ measurement is also refined. Events passing the L2 trigger are then passed to the EF trigger, which performs a full offline analysis selecting interesting events. EF makes an event reconstruction decision in under 4 s and provides output at 200-400 Hz. At L2 and EF, further requirements on the $E_{\mathrm{T}}^{\mathrm{miss}}$ of the objects

must be satisfied and electron candidates must pass additional quality criteria for final physics analysis. After the EF, the events are divided into different "streams", depending on different trigger chains. A single stream may include, for example, all events passing any photon or electron trigger or muon trigger. All of the events passing the L1 calorimeter triggers (including jet, electron, photon, and τ-lepton triggers) were put into the L1Calo stream. Triggers used for this thesis have been discussed in details in chapter 4.

Most sub-detectors have the ability to remove in part or whole without stopping the data taking, in case a single section becomes problematic for either the trigger or the data read-out chain. In case of such transitions, a luminosity block is introduced in order to provide a clear division between data taken prior to, during, and after the transition. For security reasons, at the beginning of an LHC fill, the pixel detector operates with both module high voltage and signal preamplification off, and the SCT operates at a lowered high voltage. These conditions are changed during the run after the beams have been declared stable.

One of the most important challenges to the data acquisition system (DAQ) in ATLAS is ensuring that all triggers and detectors are in sync with each other. Most detectors operate on a 40 MHz clock. Phases of all the systems must be adjusted to make sure a given clock cycle in all the subsystems corresponds to the same bunch crossing. Subdetectors may associate a signal to the incorrect collision, or miss a collisions signal all together without this important timing.

3.4 Offline Software and Data Processing

Data sets of ATLAS are far too large to be contained and processed entirely at the Tier0. Instead, the worldwide Large Computing Grid (LCG) [28] is used to distribute the data around the world for processing. Several copies of the data sets can be maintained, so that if any single processing site is unavailable, the data can still be accessed.

In order to understand detector effects in the data, ATLAS has implemented a detailed detector simulation [29] based on the Geant4 toolkit [30, 31]. The detector simulation has been tuned to agree with test beam data from both standalone test beams and a "combined" test beam with a complete wedge of the detector. Simple validation of the simulation is also performed.

Each of the detector signals produced in the simulation step is reconstructed via complex algorithms to produce particles (electrons, muons, photons, taus, etc.) with an established energy, momenta, position in θ and ϕ, vertex, impact parameter, and more. During this step, MC and data are saved into the following file formats:

- Event Summary Data (ESD) which has the most complete information on tracks, hits in the detector, and more. It is also the largest (in file size) format; accessible by the ATLAS software framework - ATHENA.

- Analysis Object Data (AOD) a slimmer version of the ESD format, has less information, making it unsuitable for analyses in which standard particles

are not used. This format is accessible by ATHENA and by the software analysis package ROOT.

- N-tuples the most commonly used format that is slimmed to only contain what is needed in particle physics analyses. Users have the option of creating their own N-tuples from ESDs or AODs or using official N-tuples. In some cases, extra information is added or recalculations are added to minimize algorithms needed in the analysis. This is the smallest file format and can be reduced even more by stripping more information from the file. In general, file-size reduction is critical because ATLAS produces several Petabytes of data per year.

3.5 DataQuality and Luminosity determination

In order to provide useful information about the quality of data for each physics run, ATLAS has implemented a set of data quality flags. These flags take one of several values: green (good), yellow, red (bad), black (detector off during the run), and gray (undefined). Generally, it is left to the detector group to define the precise meaning of the flags. For the calorimetry, in general, a red flag means that something changed during the luminosity block (e.g. a portion of the detector was disabled for part of that luminosity block) or that there was some unrecoverable data acquisition problem. A green flag means that problems with the detector were understood. A yellow or gray flag means that the quality

of the data is uncertain, and a detector expert needs to check the run. A yellow flag may also indicate that the data needs to be reprocessed, for example to mask noisy channels.

The number of read-out channels for each subdetector and the fraction of the detector providing useful data during 2011 is given in Figure 3.13. Figure 3.13 also shows the fraction of the data taken with each detector that was considered "good" after offline reprocessing. The integrated luminosity as a function of day of the 2011 run is shown in Figure 3.12, separately for the delivered integrated luminosity, and recorded integrated luminosity with all subdetectors enabled. The total recorded luminosity for this data sample is 5.2 fb^{-1}.

Van der Meer scans are used to determine the luminosity at ATLAS [32]. During these scans, the position of one beam is moved in steps with respect to the other and the hit rates in a detector in the forward region, LUCID (luminosity measurement using a Cerenkov integrating detector) [33], are measured. LUCID is located at 17m from the interaction point and counts the average number of particles per bunch crossing to determine the number of inelastic pp interactions per bunch crossing providing a measurement of the instantaneous luminosity at a given time. LUCID consists of sixteen C_4F_{10} gas filled aluminium tubes with reflective walls. When charged particles enter the gas, Cerenkov photons are created and reflected by the walls until they reach PMTs at the back of the tubes. If the signal measured by the PMTs is larger than a given threshold, a 'hit' is recorded. Timing signals are received from the LHC clock allowing the number

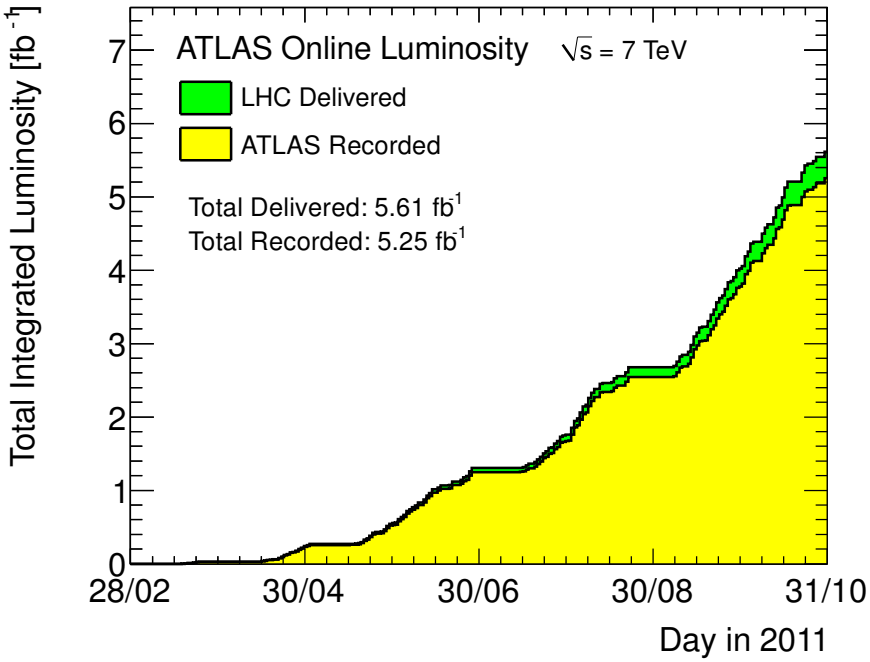

Figure 3.12: The integrated luminosity recorded by ATLAS in 2011 that was used in this analysis. All luminosity estimates have a systematic error of 3.9%.

of hits to be counted for each bunch crossing. In addition to LUCID, there is a beam conditions monitor (BCM) which is located 2m away from the interaction point and monitors beam losses and provides feedback to the team operating the LHC. The BCM makes histograms of the single-sided and coincidence rate per bunch crossing. It has excellent timing resolution of 0.7 ns, ensuring accurate determination of the bunch-by-bunch rates.

Figure 3.13 shows Luminosity weighted relative fraction of good quality data delivery by the various ATLAS subsystems during LHC fills with stable beams in pp collisions at $\sqrt{s} = 7$ TeV, and after switching the tracking detectors on.

Detector	Sub-detector	Good quality data delivery (%)
Inner Tracking	Pixel SCT TRT	99.8 99.6 99.2
Calorimeters	EM Lar Had Lar FWD Lar Tile	97.5 99.2 99.5 99.2
Muon Detector	MDT RPC CSC TGC	99.4 98.8 99.4 99.1
Magnets	Solenoid Toroid	99.8 99.3

Figure 3.13: Luminosity weighted relative fraction of good quality data delivery by the various ATLAS subdetector systems during LHC fills with stable beams in pp collisions at $\sqrt{s} = 7$ TeV. Runs between March 13th and October 30th, corresponding to a preliminary recorded integrated luminosity of 5.23 fb^{-1} , are included.

Runs between March 13th and October 30th, corresponding to a preliminary recorded integrated luminosity of 5.23 fb^{-1}, are accounted.

When the stable beam flag is raised, the tracking detectors undergo a socalled "warm start", which includes a ramp of the high-voltage and, for the pixel system, turning on the preamplifiers. The inefficiency due to this, as well as the DAQ inefficiency, are not included in the table above, but accounted for in the ATLAS data taking efficiency. This table reflects the data quality after the reprocessing.

3.6 Event Reconstruction

The measurements performed by the ATLAS detector as described in the previous sections produce raw electrical signals which must be processed in order to reconstruct the objects required for physics analysis, including tracks, particles, $E_{\mathrm{T}}^{\mathrm{miss}}$ and vertices. This section describes the methods used to reconstruct these objects from the raw data obtained by the ATLAS detector.

3.6.1 Particle Identification

Figure 3.14 shows a schematic diagram of how particles interact with the ATLAS detector. Muons are weakly interacting charged particles that may pass through the entire ATLAS detector. This leaves tracks in the inner tracking detector and muon spectrometer and deposits a small amount of energy in the electromagnetic and hadronic calorimeters. Electrons are electromagnetically charged particles that will pass through the inner tracking detector and will deposit their energy

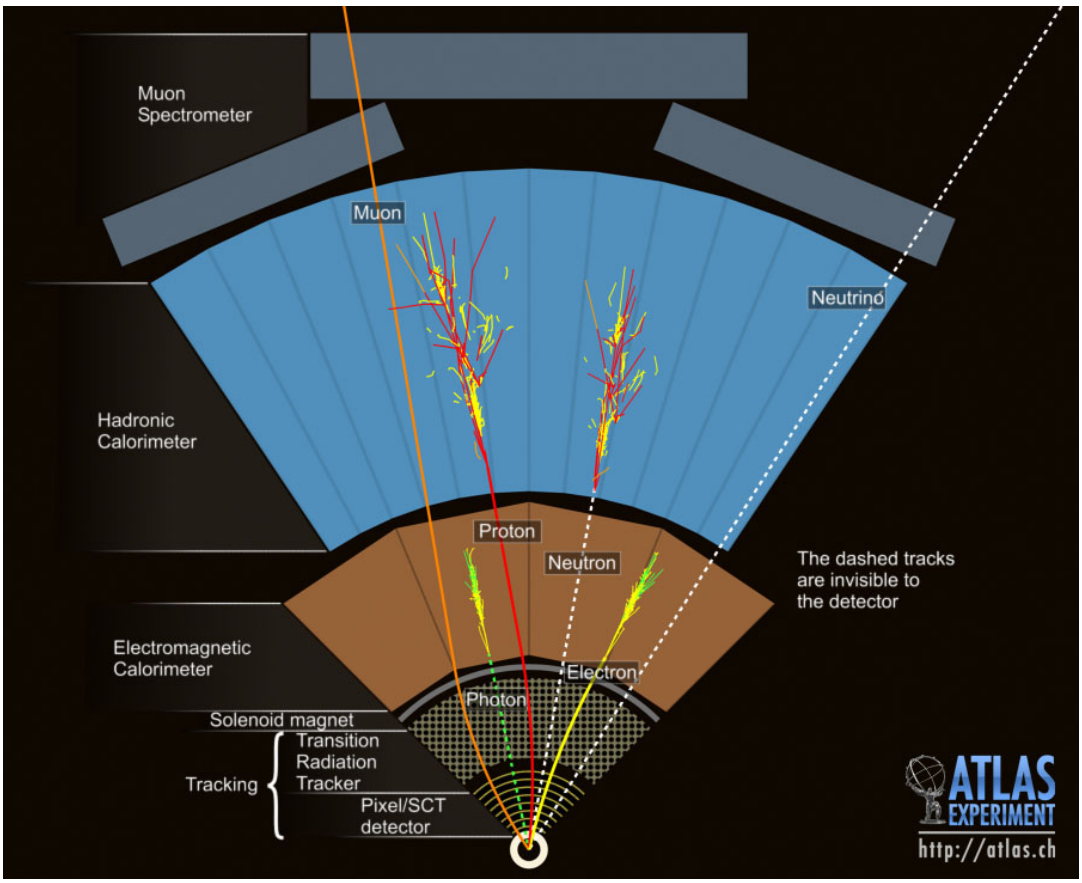

Figure 3.14: The ATLAS Particle Interactions.

in the electromagnetic calorimeter producing a track in the tracking detector. Photons are electromagnetically interacting particles that pass through the inner tracking detector and deposit their energy in the electromagnetic calorimeter, without leaving any track since it is charge neutral. Protons and neutrons deposit most of their energy in the hadronic calorimeter. Only protons will leave tracks in the inner tracking detector and a small amounts of energy deposited in the electromagnetic calorimeter. Being charge neutral, neutrons leave no tracking information. Neutrinos are invisible to the detector, but it can be identified using energy and momentum conservation laws. It is generally represented by missing energy $E_{\mathrm{T}}^{\mathrm{miss}}$.

3.6.2 Track reconstruction

The reconstruction of tracks at ATLAS is performed using data obtained by the inner detector described in Section 3.2.3. The different stages of the track reconstruction sequence are illustrated in Figure 3.15. Reconstruction of tracks occurs in three steps:

- Raw data from the pixel and SCT detectors are converted into clusters and then converted into space-points. Timing information from the TRT is converted into calibrated drift circles.

- The next step involves running various track-finding algorithms which can find tracks arising from the interaction region. Space-points from three

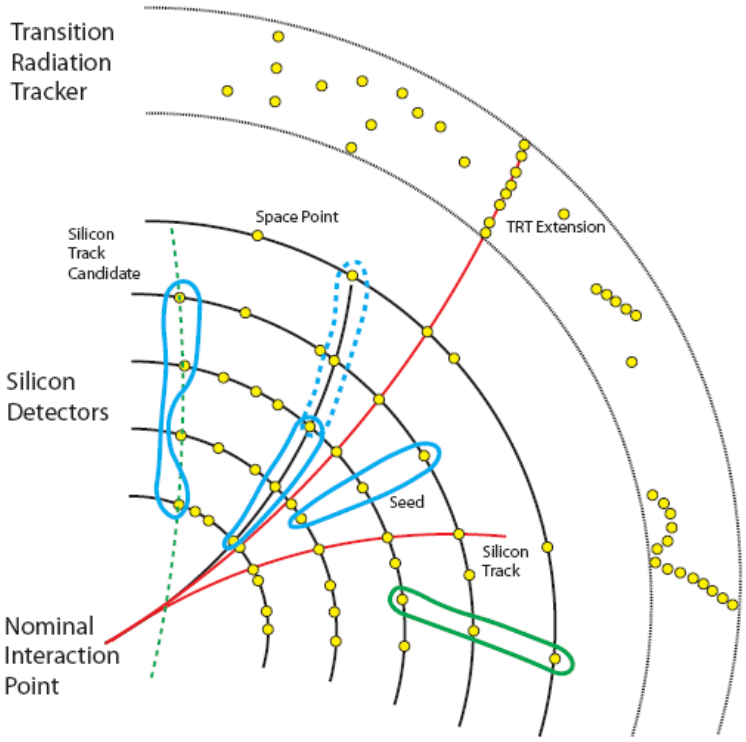

Figure 3.15: The track pattern recognition is illustrated in a simplified model of the Inner Detector. The space points are shown in yellow. The seeds (blue) are reconstructed from combinations of space points. The dashed blue seed shows two seeds correspond to the trajectory of the same charged particle. Lines show the track candidates. A track reconstructed using all three inner subdetectors is shown in black [34].

pixel layers and the first SCT layer are combined to form track seeds. These seeds are then extended, outliers are removed and by applying various quality cuts, fake tracks are rejected. These selected track candidates are extended into the TRT and using information from the pixels, SCT and TRT, a final refitting is performed to reconstruct the tracks. The converse strategy, extending TRT tracks back into the SCT and pixel detectors is used in addition to search for tracks arising from particles which may not necessarily have been produced at the primary vertex (those produced by the decay of long-lived particles).

- A vertex finding algorithm is used to reconstruct the primary vertices in the event, once these tracks have been reconstructed.

3.6.3 Electron reconstruction

Electrons traversing the LAr calorimeter, described in Section 3.2.4, deposit their energy in calorimeter cells. The summed energy in these various cells must give the total measurement of the electrons energy. This is done using "sliding window" algorithm [35].

The first step is to divide the $\eta - \phi$ space of the EM calorimeter into a grid of $N_\eta \times N_\phi$ "tower" elements with size $\Delta\eta \times \Delta\phi = 0.025 \times 0.025$ as indicated in Figure 3.16. The transverse energy of each cell of an element is summed to give a tower E_T. A window with fixed size $N_\eta^{window} \times N_\phi^{window} = 5 \times 5$ in units of tower size is moved across each element of the tower grid in steps of

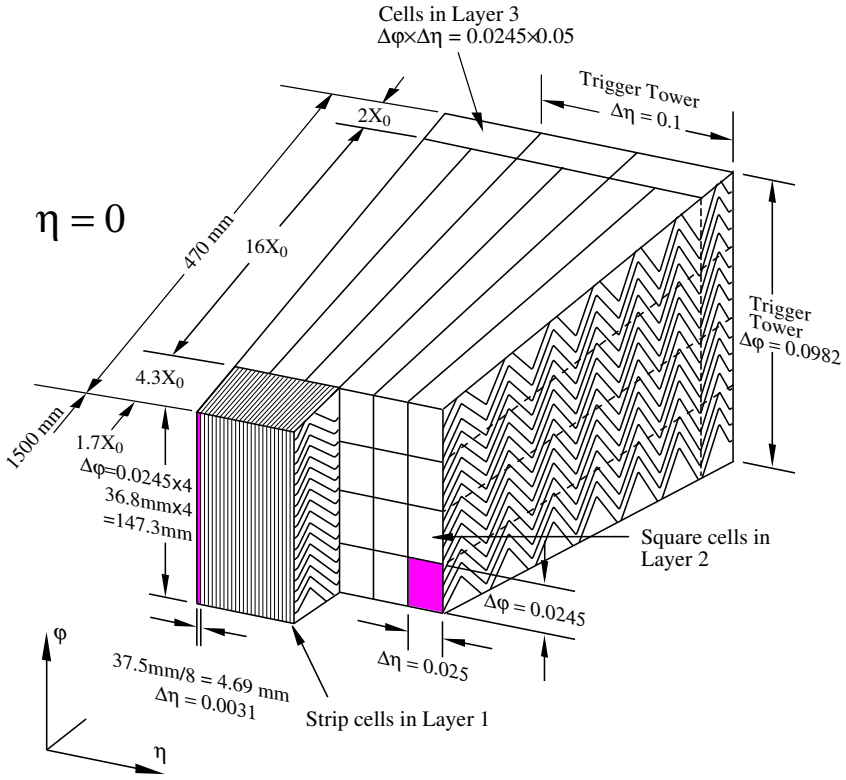

Figure 3.16: Diagram showing the structure of a barrel module of the electromagnetic calorimeter. An electromagnetic trigger tower is shown as shaded, with its η and ϕ dimensions indicated [21].

Particle type	Barrel	Endcap
Electron	3×7	5×5
Converted photon	3×7	5×5
Unconverted photon	3×5	5×5

Table 3.2: Sizes of sliding windows used in electron and photon reconstruction in terms of $N_{\eta}^{window} \times N_{\phi}^{window}$, where $\Delta\eta \times \Delta\phi = 0.025 \times 0.025$ gives the dimensions of $N_{\eta}^{window} \times N_{\phi}^{window} = 1 \times 1$.

$\Delta\eta$ and $\Delta\phi$. If the window E_T is larger than the threshold value of 3 GeV and is a local maximum, a precluster is formed. Seeds are formed from these preclusters, with electromagnetic clusters centred on these seeds. The clusters contain the energy deposited within a window size which depends on the incident particle type and the location of the seed. Table ?? shows the window sizes used for different particle types. The windows are larger in the ϕ direction in the barrel for electrons and photon conversions than for unconverted photons due to the curvature of the charged electrons and positrons in the magnetic field which causes their energy to be deposited in a larger ϕ region. The effect of the magnetic field is smaller in the endcaps, therefore all the particles have the same window size in this region.

Finally, corrections are applied to take into account for various effects including the ϕ-dependence of the amount of absorber material traversed by incident

particles, the finite granularity of the cells and the possibility that the shower is not entirely contained within the cluster window. To identify electromagnetic clusters arising from electrons rather than photons, matching is performed between the electromagnetic cluster and inner detector tracks. If $\Delta\eta < 0.5$ and $\Delta\phi < 0.1$ between a track and cluster, the cluster is considered to be matched and is, therefore, identified as an electron candidate. This has the effect of suppressing the incorrect reconstruction of photons as electrons. There may be cases where converted photons are identified as electron candidates. In these cases, the application of further identification criteria at the trigger and offline stages, tailored to select electrons arising from high momentum transfer processes rather than those originating from photon conversions, help separate converted photons from original electron candidates.

The electron identification selections are based on criteria using calorimeter and tracker information and have been optimized in 10 bins in η and 11 bins in E_T. Three reference sets of requirements "loose", "medium", and "tight" provide progressively stronger jet rejection at the expense of some identification efficiency loss. Each set adds additional constraints to the previous requirements:

"Loose" is a basic selection that uses electromagnetic shower shape information from the second layer of the electromagnetic calorimeter within the detector acceptance $|\eta| < 2.47$:

- the ratio of the energy in 3×7 cells over the energy in 7×7 cells centered

at the electron cluster position

- lateral width of the shower, and
- energy leakage into the hadronic calorimeters

as discriminant variables. This set of requirements provides high and uniform identification efficiency but a low background rejection.

The "medium" selection provides additional rejection against hadrons by evaluating the energy deposit patterns in the first layer of the EM calorimeter:

- the difference between the energy associated with the second largest energy deposit and the energy associated with the minimal value between the first and second maxima,
- second largest energy deposit normalized to the cluster energy,
- total shower width,
- shower width for three strips around the maximum strip,
- fraction of energy outside the core of three central strips but within seven strips.

Strip-based cuts are effective in the rejection of $\pi^0 \to \gamma\gamma$ decays, since the energy deposit pattern from π^0's is often found to have two maxima. Further cuts on track quality variables are also applied

- the number of hits in the pixel detector ≥ 1,
- the number of hits in the pixel and the semiconductor tracker ≥ 9,
- transverse impact parameter of the track < 1 mm,
- and a cut on the cluster track matching variable, that is $\delta\eta$ between the cluster and the track extrapolated to the first layer of the electromagnetic calorimeter.

The "medium" cuts increase the jet rejection by a factor of three to four with respect to the loose cuts, while reducing the identification efficiency at a level of ten percent.

The "tight" selection further rejects charged hadrons and secondary electrons from conversions by fully exploiting the electron identification potential of the ATLAS detector. It makes requirements on:

- the ratio of cluster energy to track momentum,
- and the number of hits in the transition radiation tracker.
- electrons from conversions are rejected by requiring at least one hit in the b- layer, the innermost layer of the pixel detector. A conversion-flagging algorithm is also used to further reduce this contribution.
- the impact-parameter requirement applied in the medium selection is further tightened at this level, as well as

- the matching criteria between the track and the cluster.

- the imposed isolation criteria demands a cut on the ratio of transverse energy in a cone of $\Delta R < 0.2$, excluding the cluster associated with the electron, to the total cluster transverse energy.

3.6.4 Muon reconstruction

There are multiple ways in which muons are reconstructed at ATLAS. These are described below.

- Standalone muons produce tracks in the muon spectrometer, which is described in Section 3.2.5. These tracks are formed from track segments in various parts of the muon spectrometer. The tracks are extrapolated back to the collision point so that the initial momentum and energy of the muon can be calculated, accounting for multiple scattering and energy loss as the muon traverses the inner detector and calorimeters in order to give an accurate measurement.

- Muons in the inner detector produce tracks solely in the inner detector. These tracks are reconstructed using the method described in Section3.6.2.

- Combined muons are formed using the muons from the combination of inner detector and muon spectrometer. This combination is performed using a statistical combination algorithm, Staco [36], which calculates the match χ^2 to determine if the match between the standalone and inner detector

muon candidate tracks is significant enough to identify the candidate as a combined muon. If so, the inner detector and muon spectrometer tracks are combined to form a combined muon track. Combined muons are used in this thesis.

3.6.5 Jet reconstruction

The ATLAS jet candidate reconstruction provides several cone and clustering jet algorithms based on signal towers or topological clusters that are constructed from the measurements in the calorimeters described in 3.2.4. Jets at ATLAS may be reconstructed in different ways with the following theoretical constraints:

- **Infrared safety:** Additional low p_T radiation between high p_T jets or, lack of such radiation between jets, should not affect the reconstruction of the jets.

- **Collinear safety:** A jet should be reconstructed in the same way regardless of whether it remains as one jet or splits into more jets.

In addition to the above constraints, the jet algorithm should not depend on the exact detector geometry, should be highly efficient and the same underlying process should be reconstructed at parton level, particle level or detector level.

Bearing these constraints in mind, the jet algorithm used in this thesis is the anti-k_T algorithm [37, 38, 39] where k_T is the transverse momentum of the particles. However, ATLAS uses p_T as the transverse momentum. Anti-k_T

algorithm is a sequential recombination algorithm. For all possible pairs of input objects, we define d_{ij}, d_i as follows :

$$d_{ij} = min\left(\frac{1}{p_{T_i}^2}, \frac{1}{p_{T_j}^2}\right)\frac{\Delta R_{ij}^2}{R^2}$$
$$d_i = \frac{1}{p_{T_i}^2} \tag{3.8}$$

where p_{T_i} is the transverse momentum of object i, $\Delta R_{ij}^2 = \Delta\eta_{ij}^2 + \Delta\phi_{ij}^2$ and R is a fixed cone size of 0.4. d_{ij} and d_i are calculated for all objects and d_{min} is found. Objects i and j are combined into a new object if $d_{min} = d_{ij}$. If $d_{min} = d_i$, object i is considered to be a jet and is removed from the list of objects. This iterative process continues until all objects are combined into jets. Therefore, all the objects are either combined together to form jets or are already considered to be a jet. This procedure is entirely infrared and collinear safe.

This algorithm may be understood better by considering certain cases. If an event has a few well-separated high-p_T and low-p_T particles, the d_{1j} between a high-p_T particle 1 and a low-p_T particle j depends on the p_T of particle 1 and the ΔR of the particles. For two low-p_T particles with a similar ΔR, the d_{ij} will be larger than the d_{1j} between a high-p_T particle and low-p_T particle. Therefore, low-p_T particles will try to cluster preferentially with high-p_T particles rather than amongst themselves. If there are no high-p_T particles within $2R$ of particle 1, the algorithm will try to combine particle 1 with all the low-p_T particles surrounding it to form a perfectly conical jet. If there is another high-p_T particle in the event (particle 2), this will be combined with particle 1 to form a single jet

if $d_{12} < R$. Particle 1 and 2 will form separate jets if $d_{12} > 2R$. If $R < d_{12} < 2R$, there will be two jets which will share a boundary. The calorimeters at ATLAS contain around 200,000 cells. In order to reconstruct jets, it is necessary to combine these cells into larger objects with larger momentum. Topological cell clusters are used as an input to the anti-k_T algorithm. These clusters are reconstructed from seed cells with a signal to noise ratio above a certain threshold. All neighbouring cells are included and neighbours of neighbours are also included if they have a signal to noise ratio above a second lower threshold. If these clusters contain local signal maxima, they are subject to a splitting algorithm which further splits the clusters. The anti-k_T algorithm is then applied to these clusters to reconstruct the final jets.

The ATLAS calorimeter has been calibrated using test-beam measurements with electrons and muons to make sure that the response of the calorimeter is correct for electromagnetic showers. Hadrons have a lower response than electrons, so explicit calibration must be applied to jets reconstructed in the calorimeter to determine the original parton energy.

There are two different schemes to calibrate jets: global calibration (calculates corrections at the jet level) and local calibration (correct the topological clusters before the jets are reconstructed). For the results described here, the local calibration scheme is used, which involves the following three steps:

- Topological cell clusters are identified as either electromagnetic or hadronic.

Electromagnetic clusters only use calibration from the test-beam data. The cells within hadronic clusters are weighted to obtain the total calibrated energy deposit. These weights are dependent on location, energy and signal.

- Corrections are applied to take into account for energy of the cluster which may not be included if it lies just below the threshold.

- To take into account for energy deposited outside the calorimeter (i.e., gap regions), a further correction is applied. After this calibration is applied, jets are formed from the clusters using the anti-k_T algorithm.

Through the use of tracking and vertexing information or the identification, selection and scale-correction of jets originating in the hard-scatter interaction can be determined. We define a discriminant, the **Jet-Vertex Fraction (or JVF)** shown in Figure 3.17, which measures the probability that a jet originated from a particular vertex, by combining tracks and their primary vertices with calorimeter jets.

Jet selection based on JVF is insensitive to the contributions from simultaneous uncorrelated soft collisions that occur during pile-up and shows good performance in a range of instantaneous luminosities.

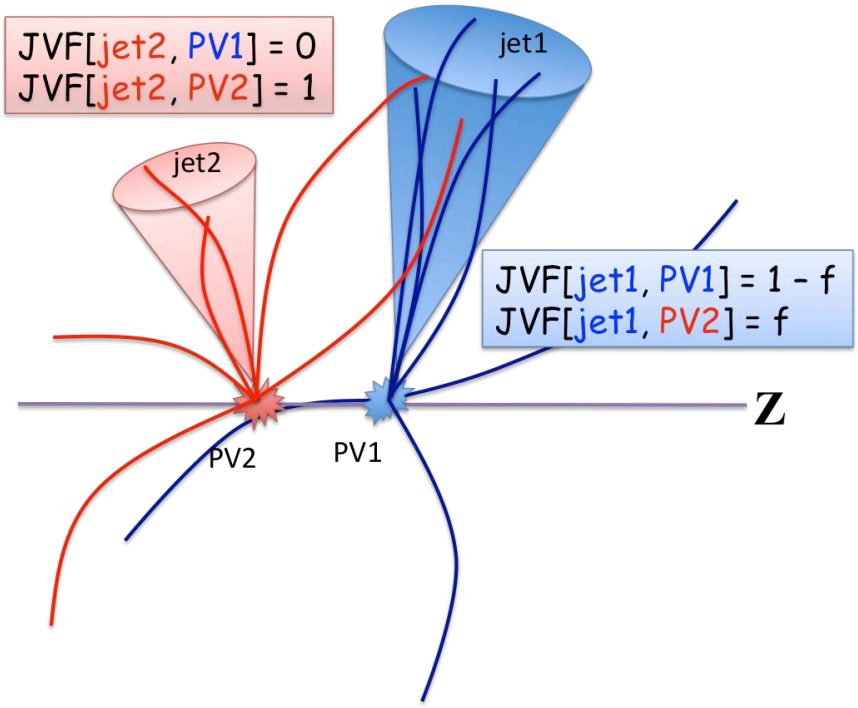

Figure 3.17: Depiction of the jet-vertex fraction (JVF) discriminant.

3.6.6 $E_{\mathrm{T}}^{\mathrm{miss}}$ reconstruction

The partons participating in the collisions at the LHC carry less momentum in the transverse plane. Energy in the collision should be conserved and in the center of mass system, the sum of energy should be 0. So the total transverse momentum of the system is expected to be *zero*. If the total transverse momentum of the system is non-zero, a quantity known as $E_{\mathrm{T}}^{\mathrm{miss}}$ is assumed to be equal and opposite to the measured system p_T such that the total p_T is zero. Neutrinos do not interact with the detector; their existence must be inferred by observing large $E_{\mathrm{T}}^{\mathrm{miss}}$. $E_{\mathrm{T}}^{\mathrm{miss}}$ is reconstructed using the energy deposited in the electromagnetic and hadronic calorimeters. There are many other possible sources of extra energy deposition by particles arising from the high momentum transfer process, detector noise, the underlying event and pileup interactions. If high-p_T objects pass through gaps in the calorimeters, this could also lead to the mismeasurement of $E_{\mathrm{T}}^{\mathrm{miss}}$. For accurate calculation of the $E_{\mathrm{T}}^{\mathrm{miss}}$, it is essential that the calculation of the energy deposited in the calorimeter is as precise as possible. The calorimeter calibrations improve the accuracy of the energy measurements in the calorimeters. In addition to calibration, noise suppression is also applied to reduce the effect of noise contributing to the measured $E_{\mathrm{T}}^{\mathrm{miss}}$. The topological cell clustering method, which is used to create clusters that may be merged into jets, helps to suppress noise since only cells with energies above a certain threshold are selected.

Chapter 4

Higgs Analysis

4.1 Standard Model Higgs Production

At high Higgs mass m_H, the Higgs boson decays dominantly to pairs of W bosons, shown in Figure 2.8. A search for resonances in the WW^* invariant mass spectrum is one of the major physics goals of the LHC. This thesis uses 4.7 fb^{-1} of $\sqrt{s}$ =7 TeV pp collision data taken by the ATLAS detector during the LHC run of 2011 to search for Higgs signals in the mass range 300 GeV$< m_{WW^*} <$ 600 GeV [18] in $H \to WW^* \to \ell\nu jj$ channel where ℓ is electron or muon. As shown in Figure 4.1, gluon-gluon fusion process is the dominant Higgs production channel at the LHC. Gluon-gluon fusion contributes $\sim 98\%$ to the total Higgs boson signal yield in $H \to WW^* \to \ell\nu jj$ decay channel. We have considered Higgs production using only gluon$-$gluon fusion process for this analysis. Higgs boson production in the gluon-gluon fusion mechanism is mediated by triangular loops of heavy quarks. In the SM, only the top quark and, to a lesser extent, the bottom quark will contribute to the amplitude, as shown in Figure 2.10.

4.2 Trigger Selection

In this Section, we detail the selection of physics objects (electrons, muons, jets, $E_{\mathrm{T}}^{\mathrm{miss}}$) and triggering criteria. The basic signature of a $H \to WW^* \to \ell\nu jj$

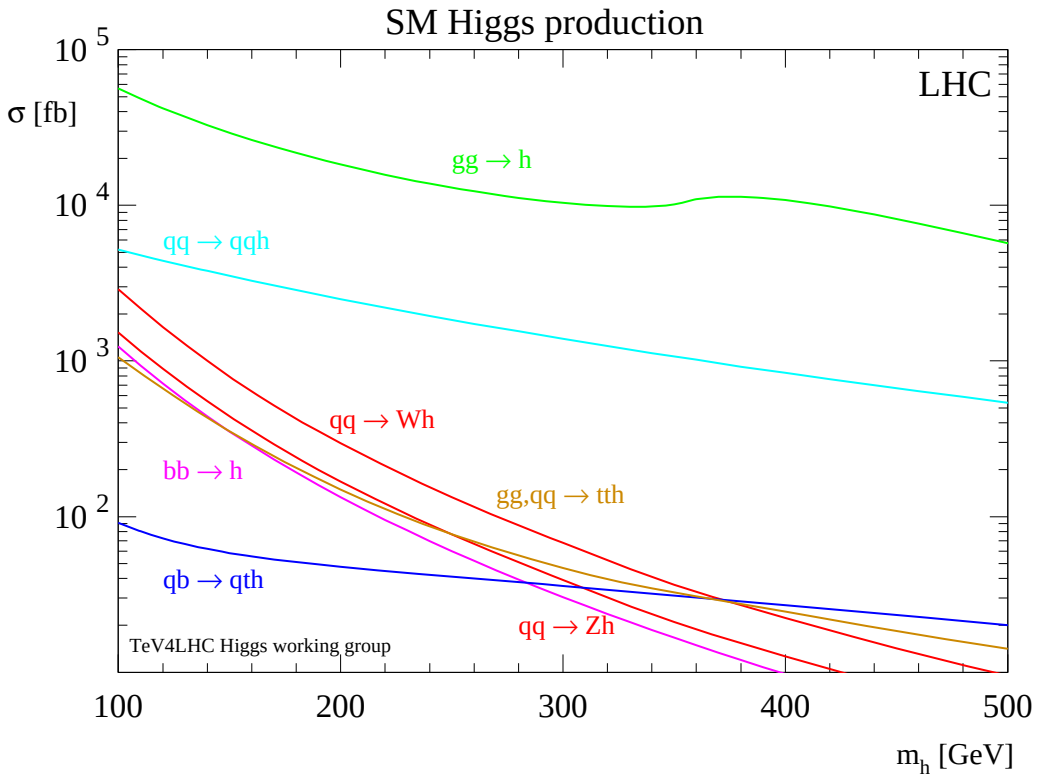

Figure 4.1: Higgs boson production at LHC [40].

Period	e channel	μ channel
B - I	EF_e20_medium	EF_mu18_MG
J	EF_e20_medium	EF_mu18_MG_medium
K	EF_e22_medium	EF_mu18_MG_medium
L - M	EF_e22vh_medium1	EF_mu18_MG_medium

Table 4.1: Period dependent trigger setup used in the analysis.

candidate event is the presence of a high p_{T} electron or muon, two (or more) jets, and large $E_{\mathrm{T}}^{\mathrm{miss}}$. The candidate events are recorded with unprescaled single lepton triggers and reconstructed offline using the official software of the experiment.

Table 4.1 shows the list of triggers used in each period. As the period changes, the number of pileup [41] collisions in each bunch crossing also increases. This increasing number of pileup results in rising event rate. To address this rising event rate, the trigger threshold for primary single lepton triggers has been gradually tightened.

EF_e20_medium, EF_e22_medium and EF_e22vh_medium1 electron triggers are used in the analysis. The numbers after EF_e in the names represent the nominal p_{T} threshold values for these triggers in GeV, medium, medium1 indicate the tightness in the electron identification and vh means that the trigger has both η dependent p_{T} thresholds and a hadronic leakage cut in Level 1. The single electron trigger required the transverse momentum (p_T threshold of the

electron varied from 20 GeV to 22 GeV). For signal electrons with $p_T > 25$ GeV, the trigger efficiency in the plateau region ranges between 95% and 97% depending on η of the electron.

The single muon triggers used in the analysis are EF_mu18_MG and EF_mu18_MG_medium. The nominal p_{T} threshold for these triggers are set to 18 GeV. with $p_T > 20$ GeV, the trigger efficiency in the plateau region ranges from about 70% for $|\eta| < 1.05$ to 88% for $1.05 < |\eta| < 2.4$.

4.3 Object Selection

4.3.1 Electrons

Electron candidates are reconstructed from clustered energy deposited in the electro-magnetic calorimeter with an associated track. Electrons are required to satisfy a tight set of identification cuts [42] with an efficiency of approximately 80% for electrons from $W \to e\nu$ with transverse energy $20 < E_{\mathrm{T}} < 50$ GeV [42]. The energy measurement is taken from the electro-magnetic calorimeter. The pseudorapidity η and azimuthal angle ϕ are taken from the associated track. The cluster is required to be in the range $|\eta| < 2.47$, excluding the transition region between barrel and endcap calorimeters, $1.37 < |\eta| < 1.52$. The track associated with the electron candidate is reconstructed from the primary vertex with a transverse impact parameter significance $|d_0/\sigma_{d_0}| < 10$ and an impact parameter along the beam direction $|z_0| < 1$ mm. Electrons are required to be isolated:

the sum of the transverse energies (excluding the electron itself) in cells inside a cone $\Delta R \equiv \sqrt{\phi^2 + \eta^2} < 0.3$ around the cluster must satisfy $\Sigma(E_{\mathrm{T}}^{calo})/p_{\mathrm{T}}^{e} < 0.14$ and the sum of the transverse momenta of all tracks with $p_{\mathrm{T}} > 1$ GeV from the primary vertex in the same cone must satisfy $\Sigma(p_{\mathrm{T}}^{track})/p_{\mathrm{T}}^{e} < 0.13$. The isolation for electrons is corrected for the impact of pile-up and the isolation cuts were optimized for the $H \to WW^* \to \ell\nu jj$ analysis.

4.3.2 Muons

Muons are reconstructed by combining tracks in the inner detector and muon spectrometer, with efficiency $92.8 \pm 0.2\%$ for muons from $W \to \mu\nu$ decays with transverse momentum $p_{\mathrm{T}} > 20$ GeV [43]. To reduce mis-identifications and improve on the muon momentum resolution, we apply quality requirements on the muon track reconstruction. Muon tracks are required to have at least two hits in the pixel detector, one of them in the first layer, and six or more hits in the SCT. Tracks are vetoed if they have more than two holes in the SCT and pixel detectors, as well as tracks with an excessive amount of outlier hits in the TRT. They must lie within the pseudorapidity range $|\eta| < 2.4$. The muons must satisfy the same z_0 cut as electrons and transverse impact parameter significance $|d_0/\sigma_{d_0}| < 3$. They must also be isolated, with the sum of the transverse energies (excluding those attributed to the muon itself) in calorimeter cells inside a cone $\Delta R < 0.3$ around the muon satisfying $\Sigma(E_{\mathrm{T}}^{calo})/p_{\mathrm{T}}^{\mu} < 0.14$ and the sum of the transverse momenta of all tracks with $p_{\mathrm{T}} > 1$ GeV from the primary vertex in a

cone $\Delta R < 0.4$ around the muon satisfying $\Sigma(p_{\mathrm{T}}^{track})/p_{\mathrm{T}}^{\mu} < 0.15$. The isolation for muons is corrected for the impact of pile-up using the same procedure as described for electrons.

4.3.3 Jet Selection

Jets are reconstructed from topological clusters using the anti-k_t algorithm [37, 38, 39] with radius parameter $R = 0.4$ and with the requirement on the jet vertex fraction (JVF, described in Section 3.6.5) ($|JVF| \geq 0.75$) which is needed to reduce contribution from pileup (Section 2.6.1) jets in central region. The reconstructed jets are calibrated using p_{T} and η dependent correction factors based on MC simulation and validated with data [44]. The selected jets are required to have $p_{\mathrm{T}} > 25$ GeV and $|\eta| < 4.5$. Jets are considered b-tagged if they are consistent with having originated from the decay of a b-quark. This is determined by a dedicated b-tagging algorithm which uses a combination of impact parameter significance and secondary vertexing information and exploits the topology of weak b- and c-hadron decays. The algorithm is tuned to achieve an 80% b-jet identification efficiency while yielding a light-jet tagging rate of approximately 6% [45].

4.4 Event Selection

In this section, we describe the event selection used in the $H \to WW^* \to \ell\nu jj$ analysis which includes the following cuts:

- The very first step in the data selection criteria is use of the GoodRunList (GRL) package. The GRL package uses XML files produced by the combined performance and physics groups to determine which LumiBlocks[1] in data runs have good detector performance. By applying separate GRLs to each of the final states, the integrated luminosity of the $H \to WW^* \to \ell\nu jj$ analysis is maximized per final state.

- As the $H \to WW^* \to \ell\nu jj$ analysis heavily relies on the LAr calorimeter, an additional cut is placed on data to ensure that an event does not suffer from a noise burst or data corruption after bulk (re)processing, e.g. software or detector problems occurring during data collection [46].

- There must be at least one reconstructed primary vertex with three associated tracks in each event. This requirement ensures that collision candidates are selected. During vertex finding/reconstruction, a beam spot constraint is applied, ensuring that the size of the beam spot is compatible with each primary vertex candidate.

- There must be exactly one reconstructed lepton candidate (electron or muon) with $p_T > 40$ GeV.

- The event must have $E_{\mathrm{T}}^{\mathrm{miss}} > 40$ GeV.

- There must be exactly two or three jets with $p_T > 25$ GeV in $|\eta| < 4.5$.

[1] A luminosity block is a 1 or 2-minute block of data as recorded by ATLAS spanning several selected events.

The two jets with invariant mass closest to the mass of the W boson are required to satisfy $71 < M_{jj} < 91$ GeV. These jets are taken as the W decay jets.

- One of these two jets must satisfy $p_T > 60$ GeV and the other must satisfy $p_T > 40$ GeV.

- The two W decay jets are required to lie in the the range $|\eta| < 2.8$ where the jet energy scale uncertainty is $\sim 5\%$ or less for $p_T > 40$ GeV [44].

- To suppress W+ jets background, the selected two jets must satisfy $\Delta R < 1.3$ where $\Delta R = \sqrt{(\Delta\eta)^2 + (\Delta\phi)^2}$.

- In order to reject backgrounds from top quark production, events are rejected if any of the jets are b-tagged. b-tagging algorithm uses a combination of impact parameter significance and secondary vertex information and exploits the topology of weak decays of b- and c-hadrons. The algorithm is tuned to achieve a 80% b-jet identification efficiency [47], which results in a tagging rate for light quark jets of approximately 6% [48].

- We define $\ell\nu jj + 0j$ channel in which one lepton (electron or muon), two jets and $E_{\mathrm{T}}^{\mathrm{miss}}$ are in the final state. For $\ell\nu jj + 1j$ channel in which one lepton (electron or muon), three jets and $E_{\mathrm{T}}^{\mathrm{miss}}$ are in the final state.

- The gluon-gluon fusion process is expected to contribute $\sim 98\%$ for $\ell\nu jj$+$0j$ and $\sim 92\%$ for $\ell\nu jj + 1j$ to the total signal yield, with the remainder

primarily due to the weak boson fusion process.

4.5 Higgs Mass Reconstruction

In this Section, we describe the calculation of the Higgs invariant mass which is used to extract the observed Higgs signal yield.

In order to reconstruct the invariant mass $m(\ell\nu jj)$ of the WW^* system, the mass constraint equation $M_{l\nu} = M_W$ for the unmeasured z-momentum of the neutrino was used, taking the transverse components of the neutrino momentum to be the x and y components of the measured $E_{\mathrm{T}}^{\mathrm{miss}}$. To reconstruct the neutrino longitudinal momentum (p_z^ν), the mass of the lepton (e or μ) + neutrino (ν) has to be exactly equal to the PDG W mass (80.4 GeV). p_z^ν can be written as

$$p_z^\nu = \frac{(M_W^2 - M_\ell^2 + 2p_{\ell T}.p_T^\nu)\, p_{\ell z} \pm \sqrt{D}}{2\,(E_\ell^2 - p_{\ell z}^2)} \tag{4.1}$$

with

$$D = E_\ell^2\{\left(M_W^2 - M_\ell^2 + 2p_{\ell T}\right)^2 - 4\,(E_T^\nu)^2\left(E_\ell^2 - p_{\ell z}^2\right)\} \tag{4.2}$$

where ℓ = electron or muon.

For negative values of D, p_z^ν has complex solution. In the case of complex p_z^ν solutions, the event is rejected. This rejects $(20 \pm 1)\%$ of MC signal events with $m_H = 400$ GeV, while for MC W+jets the corresponding value is $(30 \pm 1)\%$. Larger fractions of events are rejected in $\ell\nu jj + 1j$ than $\ell\nu jj + 0j$ independent

of lepton flavor. In collision data $(30 \pm 1)\%$ of the events are rejected by this requirement, consistent with the expectations from W+jets background simulation. In the case of two real solutions, the solution with smaller neutrino longitudinal momentum $|p_z^\nu|$ is taken, based on simulation studies. Table **??** shows the observed and expected numbers of events for signal and background after this full selection.

The hadronically decaying W candidate is reconstructed by selecting the pair of jets whose dijet invariant mass is closest to the W mass.

4.6 Background Estimation

In this Section, we describe the background estimation for the analysis.

Although the MC is not used to model the background in the final fit used to obtain limits, a combination of MC and data-driven methods is used to better understand the background yields at this intermediate stage. Backgrounds due to W/Z+jets, $t\bar{t}$, and diboson production are modeled using the ALPGEN [49], MC@NLO [50], and HERWIG [51] generators, respectively. A small contribution from $W/Z + \gamma$ events is generated using MadEvent [52].

The W/Z+jets cross sections as a function of jet multiplicity is not known precisely. Due to this reason, W/Z+jets events obtained from MC need to be normalized using a scale factor obtained from data. The scale factor is obtained from a fit to $E_{\mathrm{T}}^{\mathrm{miss}}$ distribution [19], and the resulting scale factors are then used

Process	Generator	cross-section σ (pb) [$\times$ BR]
Inclusive $W \to \ell\nu$	ALPGEN	10.5×10^3
Inclusive $W \to \tau\nu$	PYTHIA	10.5×10^3
Inclusive $Z/\gamma^* \to \ell\ell$	ALPGEN	10.7×10^2
Inclusive $Z/\gamma^* \to \tau\tau$	PYTHIA	9.9×10^2
Inclusive $Z/\gamma^* \to \ell\ell$	ALPGEN	3.9×10^3
Inclusive $Z/\gamma^* \to \tau\tau$	PYTHIA	4.0×10^3
$t\bar{t}$	MC@NLO	164.6
Single top Wt	MC@NLO	13.1
Single top s-channel	MC@NLO	3.9
Single top t-channel	MC@NLO	58.7
WW	HERWIG	45.0
WZ	HERWIG	18.0
ZZ	HERWIG	5.96
$\gamma W \to \ell\nu(\ell = e, \mu, \tau)$	PYTHIA,MADGRAPH	135.4
Dijet ($8 < p_T < 1120$ GeV)	PYTHIA	1.1×10^{10}

Table 4.2: Cross-sections at the centre-of-mass energy of $\sqrt{s} = 7$ Tev for background processes. The $W \to \ell\nu$ and the $Z/\gamma^* \to \ell\ell$ cross-sections are single flavour cross-sections.

to normalize W/Z+jets processes in comparisons between data and expectations. Table **??** gives all major background contributions. QCD multi-jet backgrounds have been estimated using the data driven **Matrix Method** described in section 4.6.1. Gluon-gluon fusion signal MC production processes are simulated using the POWHEG [53] event generator interfaced to PYTHIA [54], normalizing to the NNLO cross sections [13] shown in Table **??**.

4.6.1 QCD Background Estimation using Matrix Method

QCD events can enter the sample when one of the jets fakes a charged lepton and the $E_{\mathrm{T}}^{\mathrm{miss}}$ is mis-reconstructed. Due to the large cross-section of the multi-jet events, we need to simulate multi-jet events. We use a data-driven method to estimate the QCD background that enters our signal region.

The Matrix Method is used to validate the QCD event yields in the nominal analysis that is presented here. Multi-jet production ("QCD") is the dominant process by which events with a mis-reconstructed lepton appear in the selected sample. We use data-driven methods, as the mis-reconstruction of a lepton is difficult to simulate accurately. We use the matrix method to measure the fraction of the sample that comes from fake leptons.

The matrix method (MM) exploits differences in lepton identification-related properties between prompt isolated leptons from W and Z decays (referred to as "real leptons" below) and those where the leptons are either non-isolated or result from misidentification of photons/jets (referred to as "fake leptons" below). For

this purpose, two samples are defined after requiring the final kinematic selection criteria, differing only in the lepton identification criteria: a "tight" sample and a "loose" sample, the former being a subset of the latter. The tight selection typically employs the final lepton identification criteria used in the analysis, whereas the loose selection is adjusted in order to satisfy basic requirements for the method to work, which are outline below.

The method assumes that the number of selected events in each sample (N^l and N^t) can be expressed as a linear combination of the numbers of events with real and fake leptons, in such a way that the following system of equations can be defined:

$$\begin{aligned} N^{\text{loose}} &= N^{\text{loose}}_{\text{real}} + N^{\text{loose}}_{\text{fake}}, \\ N^{\text{tight}} &= \epsilon_{\text{real}} N^{\text{loose}}_{\text{real}} + \epsilon_{\text{fake}} N^{\text{loose}}_{\text{fake}}, \end{aligned} \tag{4.3}$$

where $\epsilon_{\text{real}}(\epsilon_{\text{fake}})$ represents the probability for a real (fake) lepton that satisfies the loose criteria, to also satisfy the tight ones. Therefore, these efficiencies are defined as:

$$\epsilon_{\text{real}} = \frac{N^{\text{tight}}_{\text{real}}}{N^{\text{loose}}_{\text{real}}}, \tag{4.4}$$

$$\epsilon_{\text{fake}} = \frac{N^{\text{tight}}_{\text{fake}}}{N^{\text{loose}}_{\text{fake}}}. \tag{4.5}$$

Assuming ϵ_{real} and ϵ_{fake} can be estimated in control samples, the system of equations in Eq. 4.3 can be solved yielding the estimated number of events with a fake lepton in the tight sample:

$$N_{fake}^{\text{tight}} = \frac{\epsilon_{\text{fake}}}{\epsilon_{\text{real}} - \epsilon_{\text{fake}}}(N^{\text{loose}}\epsilon_{\text{real}} - N^{\text{tight}}) \tag{4.6}$$

The matrix method determines the QCD background from the difference in efficiency to reconstruct leptons with "loose" and "tight" criteria. The matrix method provides the weight and error in weight for each event for fake leptons and QCD background is the sum of all these weights. Using the matrix method, QCD background can be obtained as a function of any desired variables.

Channel	Real Efficiency (%)	FakeRate (%)
μ	97.33 $\pm$ 0.01	19.02 $\pm$ 0.03
e	93.5 $\pm$ 0.01	45.43 $\pm$ 0.01

Table 4.3: Data driven fake and real lepton reconstruction efficiency measurement.

The following definitions were used:

- Loose electrons

  No calorimeter isolation requirement

  No d_0 requirement.

- Loose muons

  No calorimeter isolation requirement

  No track isolaion requirement

  No $d0$ requirement.

We define a control region:

- Exactly two leptons (electrons or muons, either loose or tight) with opposite sign (OS)

- $|m_{\ell\ell} - m_Z| < 15$ GeV

The fake rates are measured in QCD-enriched control regions defined by:

- Exactly 1 loose lepton

- $E_{\mathrm{T}}^{\mathrm{miss}} < 30$ GeV

- $N_{jet} \geq 1$

The determination of fake lepton efficiency and real lepton efficiency is based on the same triggers and same data streams used for the main analysis. The real lepton efficiency is measured for both electrons and muons using the **Tag and Probe** method. We require the tag lepton to be tight and the probe lepton to be loose, and then check how often the probe lepton is in addition tight.

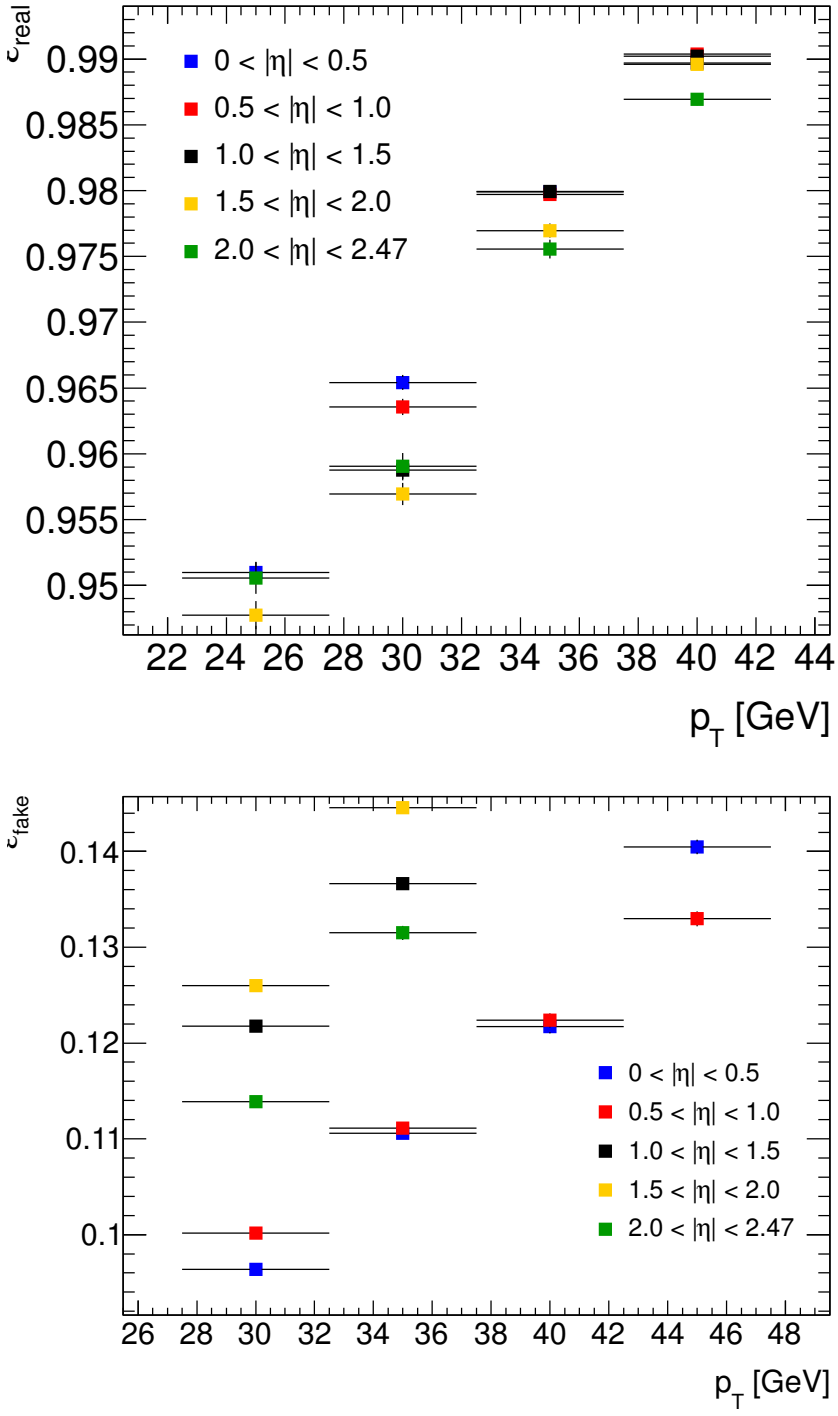

Figure 4.2: Real μ efficiency measured using Tag and Probe Method as a function of η_μ and p_T (top); Measured μ fake rate as a function of η_μ and p_T (bottom).

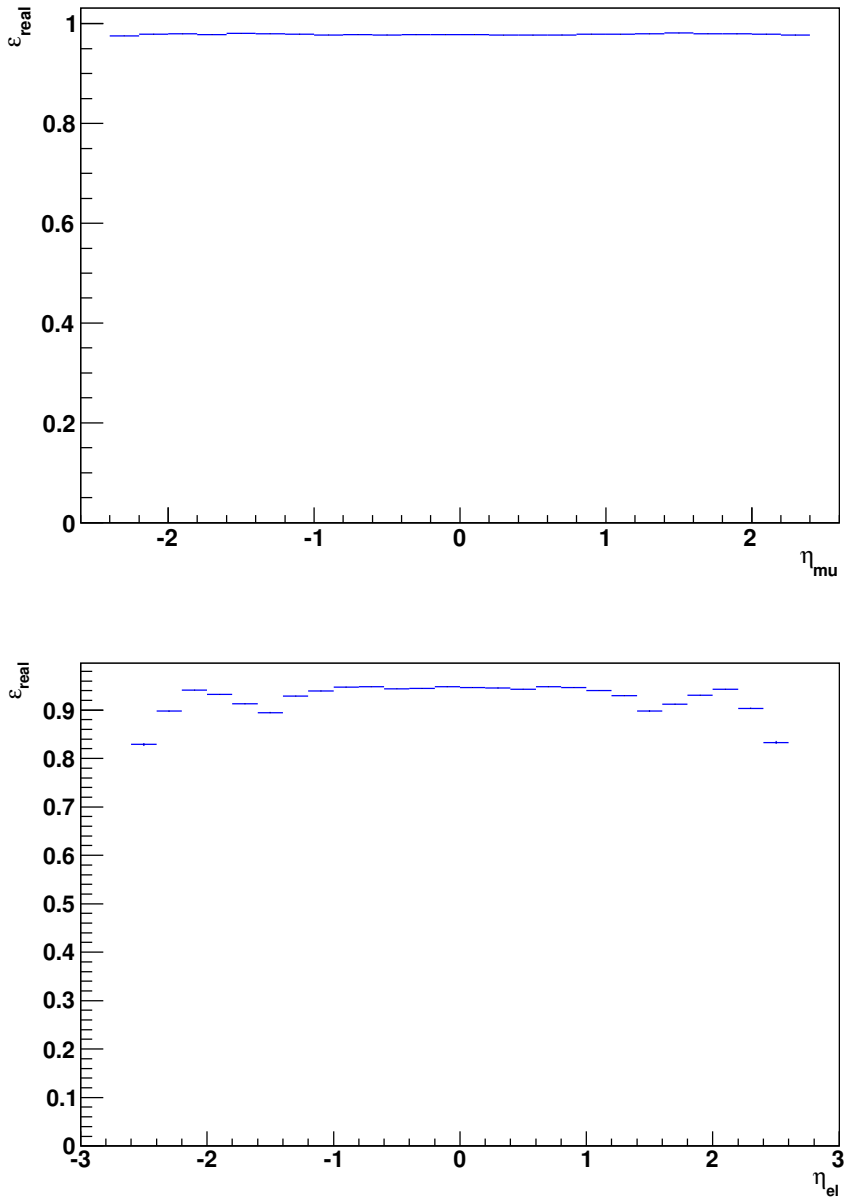

Figure 4.3: Real efficiency measured using Tag and Probe Method as a function of η. top : μ channel, bottom : electron channel.

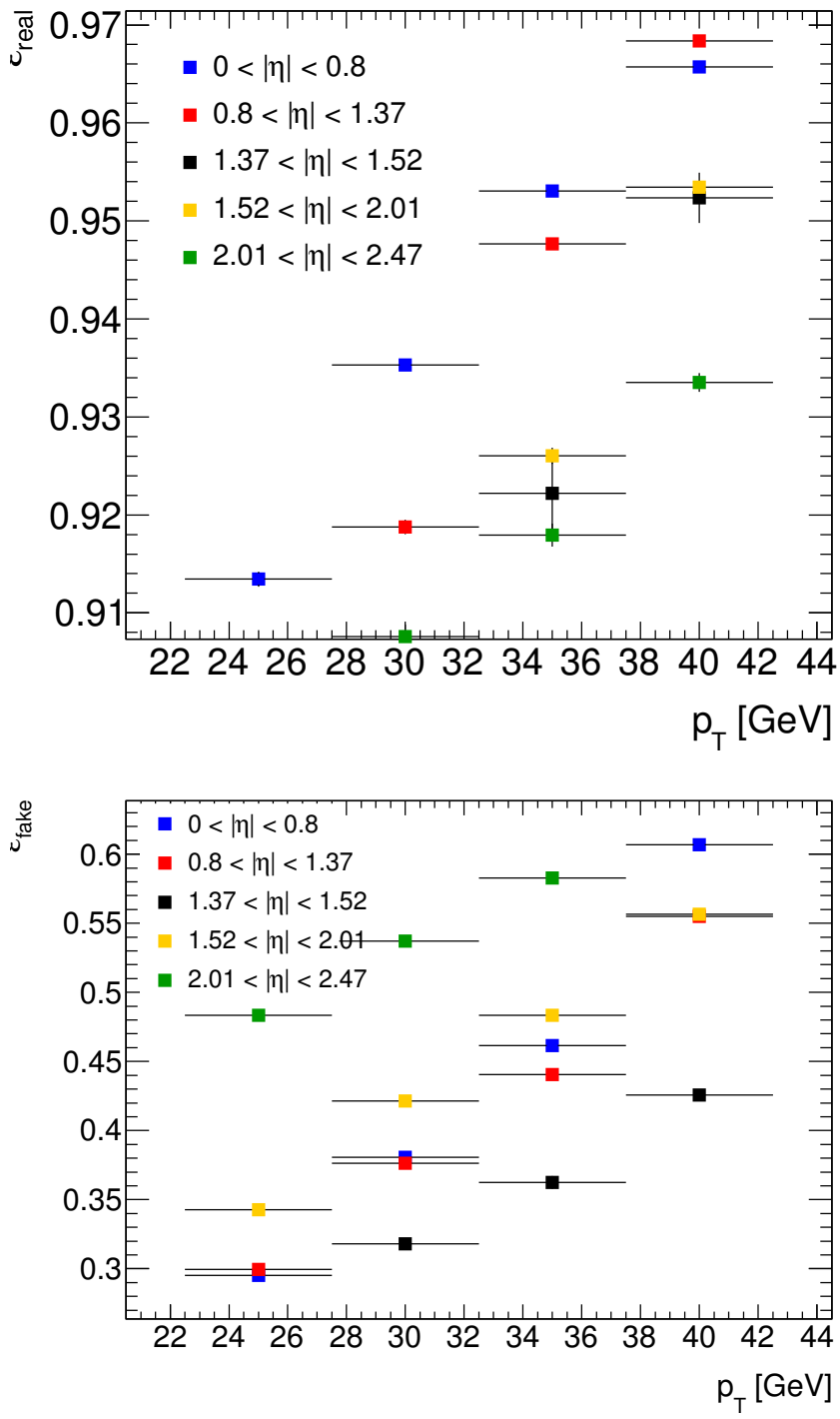

Figure 4.4: Top: real electron efficiency measured using Tag and Probe Method as a function of η_{el} and p_T; Bottom: measured electron fake rate as a function of η_{el} and p_T.

Figure 4.2 shows the real efficiency of leptons measured using Tag and Probe method as a function of lepton η and p_T. Figure 4.3 shows real efficiency as a function of lepton η only.

4.7 Expected and Observed Yields

In this Section, we present comparisons between the background expectations and data in terms of yields and kinematic distributions.

Table 4.4 and 4.5 show the observed and expected numbers of events for signal and background for the $H + 0/1j$ analysis for electron and muon channel respectively. For the W/Z+jets and QCD backgrounds, the uncertainties are taken from the fit to the $E_{\mathrm{T}}^{\mathrm{miss}}$ distribution used to normalize these backgrounds. For signal, top and diboson, the quoted uncertainties are JES ($\pm$8%), JER ($\pm$7%) cross section ($\pm$10% for both top and diboson, and $\pm$ 19.4% for signal), and luminosity ($\pm$3.9%), added in quadrature. Figure 4.5 and Figure 4.6 show reconstructed invariant mass distribution of M_{WW^*} for H+0j. Figure 4.7 and Figure 4.8 show reconstructed invariant mass distribution of M_{WW^*} for H+1j. Figure 4.9 and Figure 4.10 show the event display of two Higgs like events in the ATLAS detector.

	H($e\nu jj$) + 0j	H($e\nu jj$) + 1j
W/Z + LF jets	819 ± 184	631 ± 142
W/Z + HF jets	107 ± 31	131 ± 37
QCD	24 ± 7	24 ± 7
Top	82 ± 22	363 ± 92
Dibosons	88 ± 27	39 ± 13
Expected Background	1120 ± 190	1188 ± 174
Data	1004	1156
Expected Signal ($m_H = 400$ GeV)	35 ± 7	25 ± 6

Table 4.4: The expected and observed numbers of events for an integrated luminosity of 4.7 fb^{-1} after all selection cuts for the signal and the main backgrounds in the $H \to WW^* \to e\nu jj$ analysis [19, 55].

	H($\mu\nu jj$) + 0j	H($\mu\nu jj$) + 1j
W/Z + LF jets	662 ± 149	527 ± 119
W/Z + HF jets	104 ± 30	95 ± 27
QCD	13 ± 4	79 ± 18
Top	72 ± 20	309 ± 79
Dibosons	73 ± 22	36 ± 12
Expected Background	924 ± 155	1046 ± 147
Data	851	1013
Expected Signal ($m_H = 400$ GeV)	29 ± 7	21 ± 6

Table 4.5: The expected and observed numbers of events for an integrated luminosity of 4.7 fb^{-1} after all selection cuts for the signal and the main backgrounds in the $H \to WW^* \to \mu\nu jj$ analysis [19, 55].

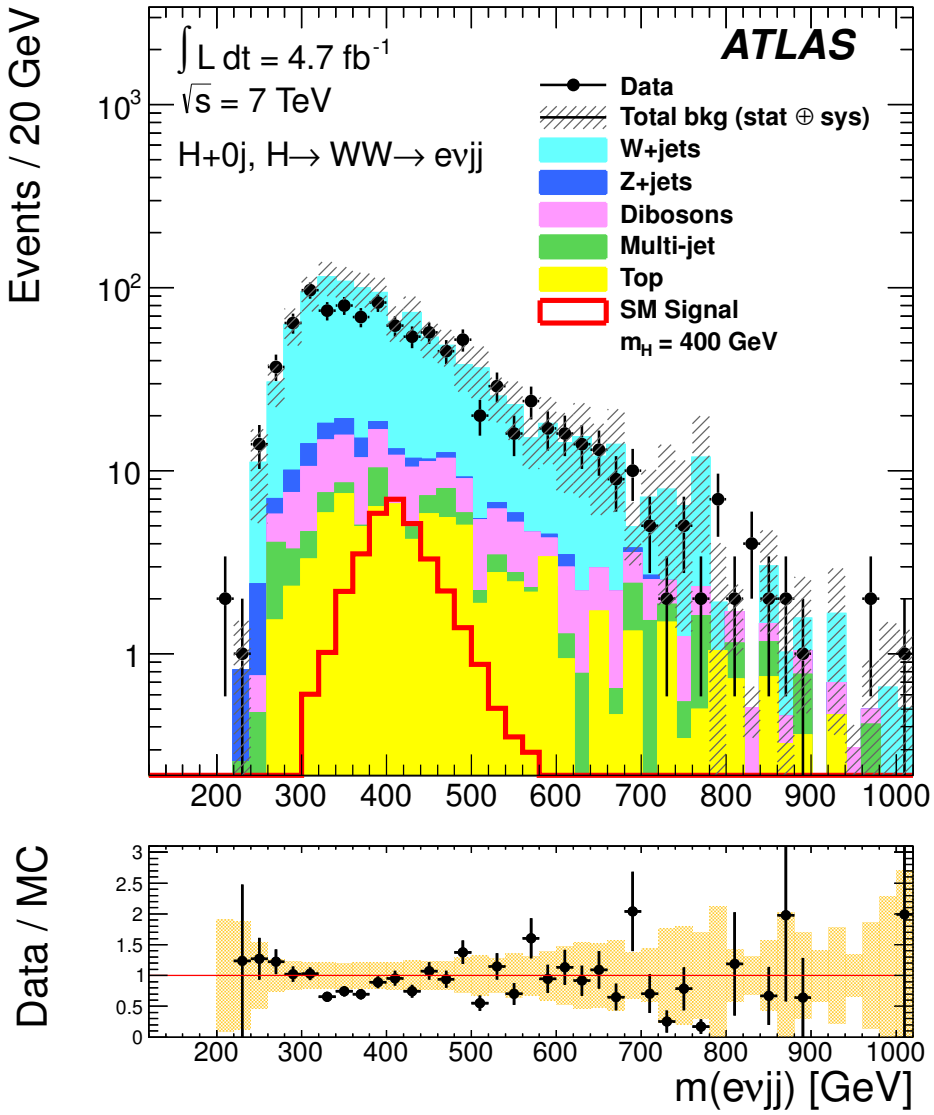

Figure 4.5: Reconstructed invariant mass $m(\ell\nu jj)$ for the $e\nu jj+0j$ selection [18].

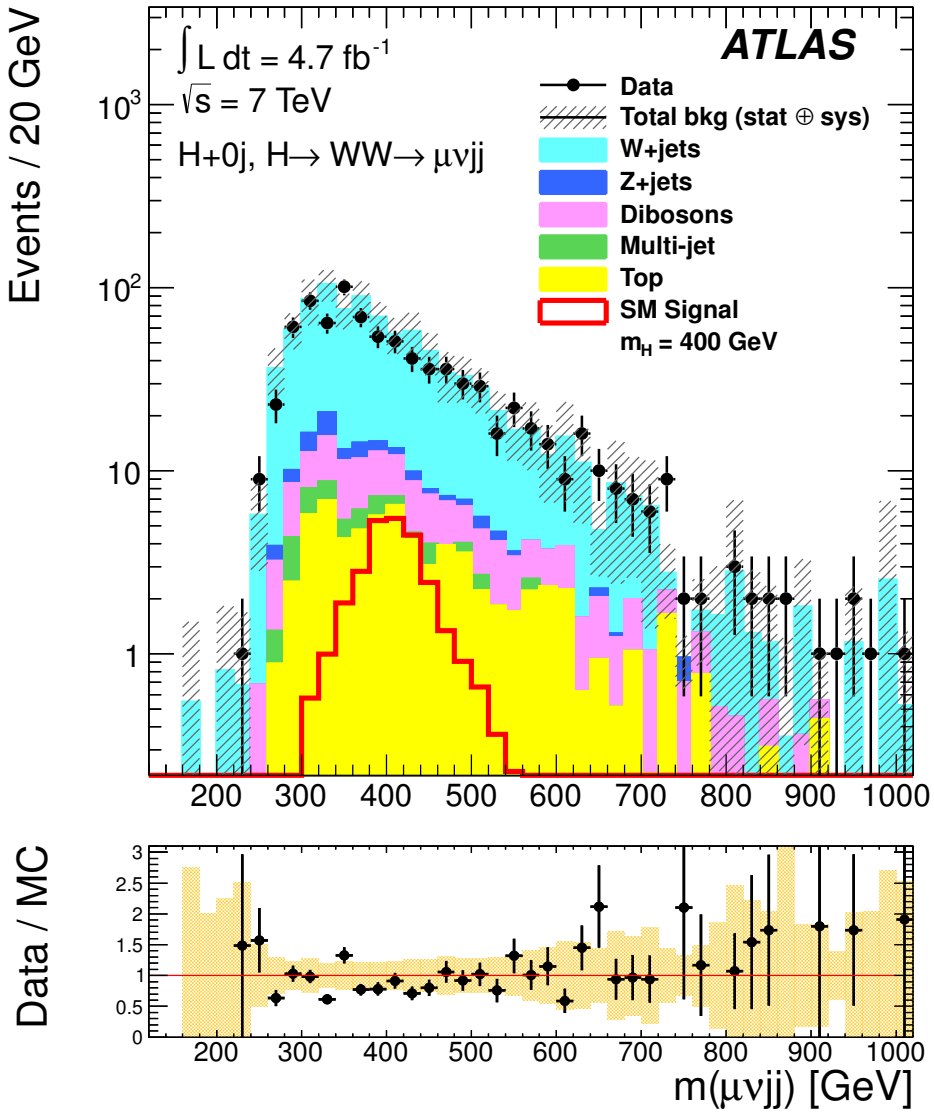

Figure 4.6: Reconstructed invariant mass $m(\ell\nu jj)$ for the $\mu\nu jj+0j$ selection [18].

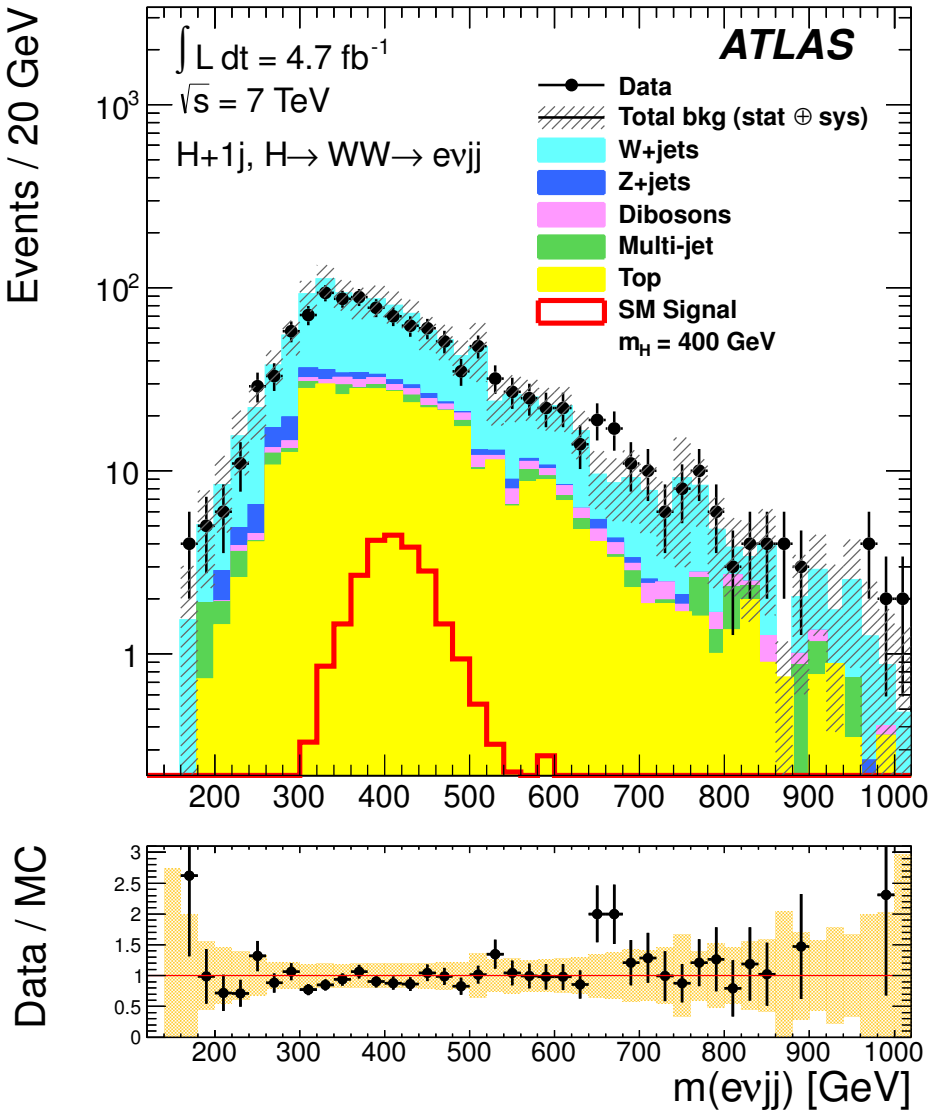

Figure 4.7: Reconstructed invariant mass $m(\ell\nu jj)$ for the $e\nu jj+1j$ selection [18].

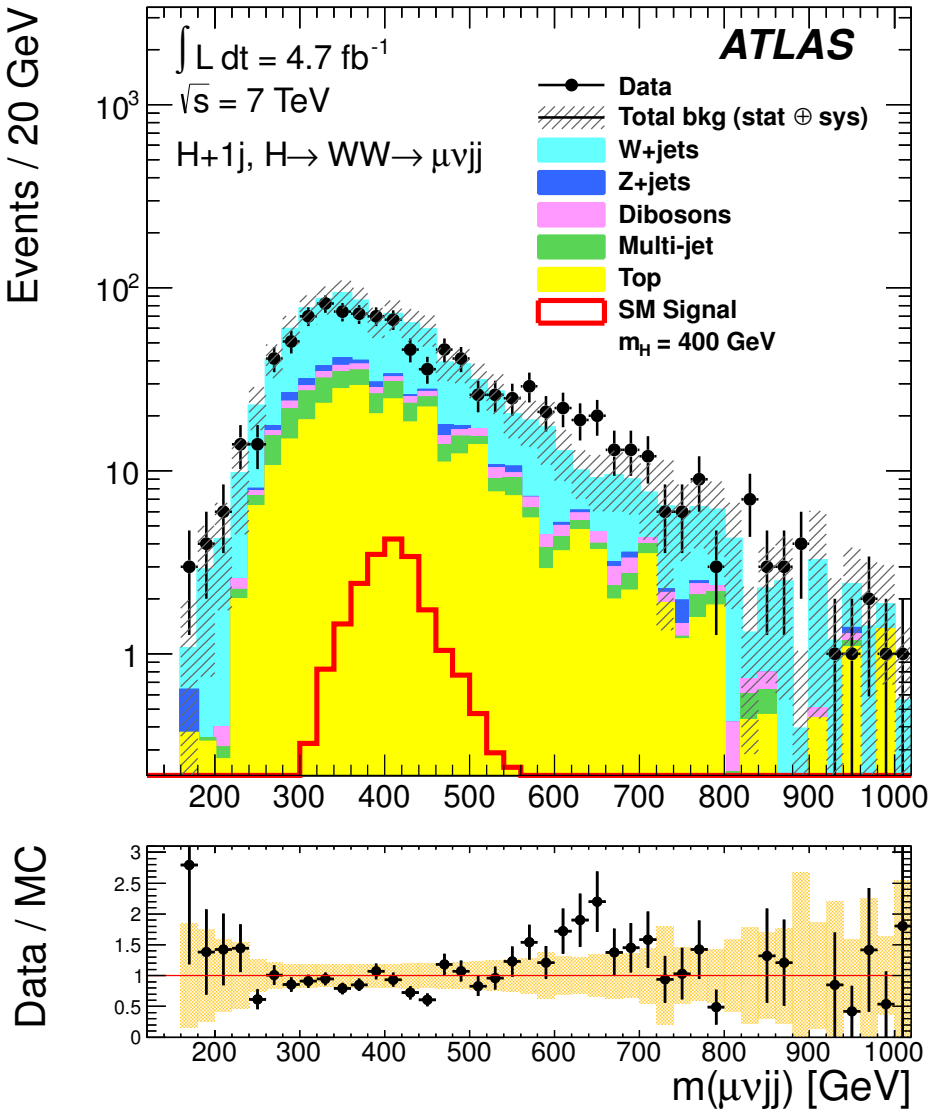

Figure 4.8: Reconstructed invariant mass $m(\ell\nu jj)$ for the $\mu\nu jj+1j$ selection [18].

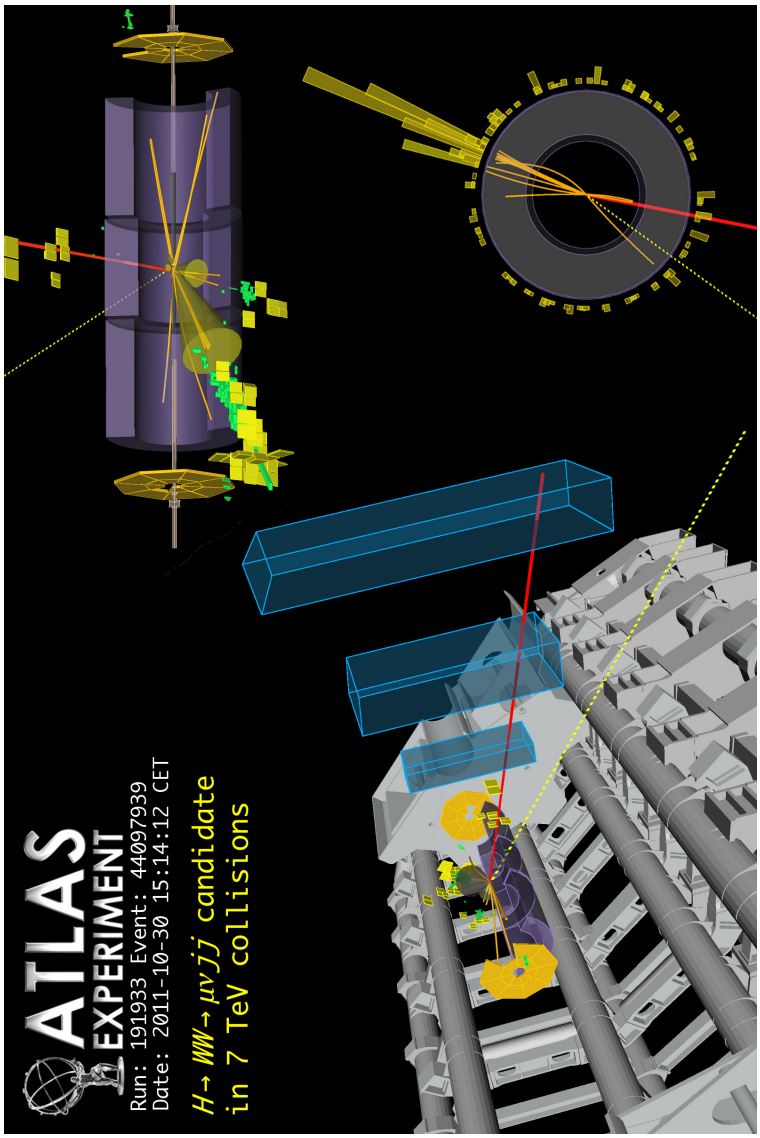

Figure 4.9: Event display of a $H \to WW^* \to \mu^+\nu jj + 0j$ candidate with invariant mass 584 GeV. The m_{jj} is 87 GeV and $m_T^{\mu\nu}$ is 47 GeV and $E_{\mathrm{T}}^{\mathrm{miss}} = 73$ GeV. The first jet has $p_{\mathrm{T}} = 197$ GeV and $\eta = -1.13$. The second jet has $p_{\mathrm{T}} = 59$ GeV and $\eta = -0.39$. The muon has $p_{\mathrm{T}} = 160$ GeV and $\eta = 0.30$.

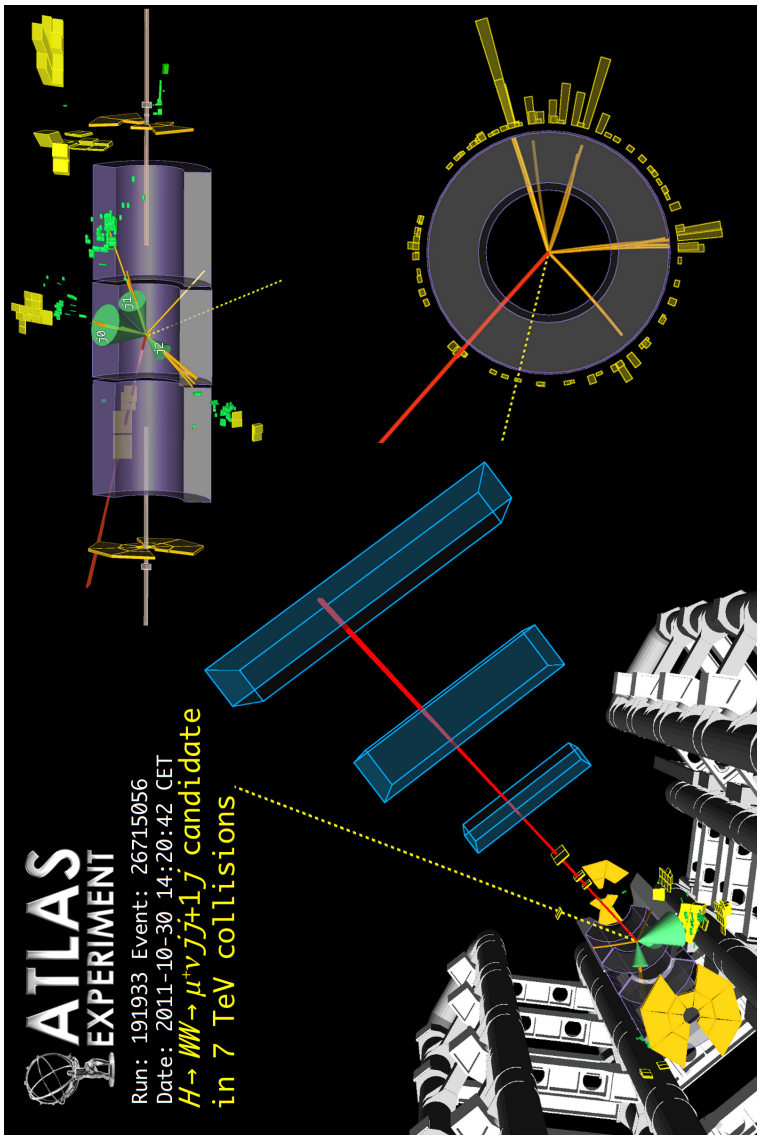

Figure 4.10: Event display of a $H \to WW^* \to \mu^+\nu jj + 1j$ candidate with invariant mass 388 GeV. The m_{jj} is 79 GeV and $m_T^{\mu\nu}$ is 39 GeV and $E_{\mathrm{T}}^{\mathrm{miss}} =$ 128 GeV. The first jet has $p_{\mathrm{T}} = 88$ GeV and $\eta = 0.32$. The second jet has $p_{\mathrm{T}} = 86$ GeV and $\eta = 1.03$. The third jet, which is *not* matched to the hadronically decaying W, has $p_{\mathrm{T}} = 45$ GeV and $\eta = -0.58$. The muon has $p_{\mathrm{T}} = 49$ GeV and $\eta = -0.57$.

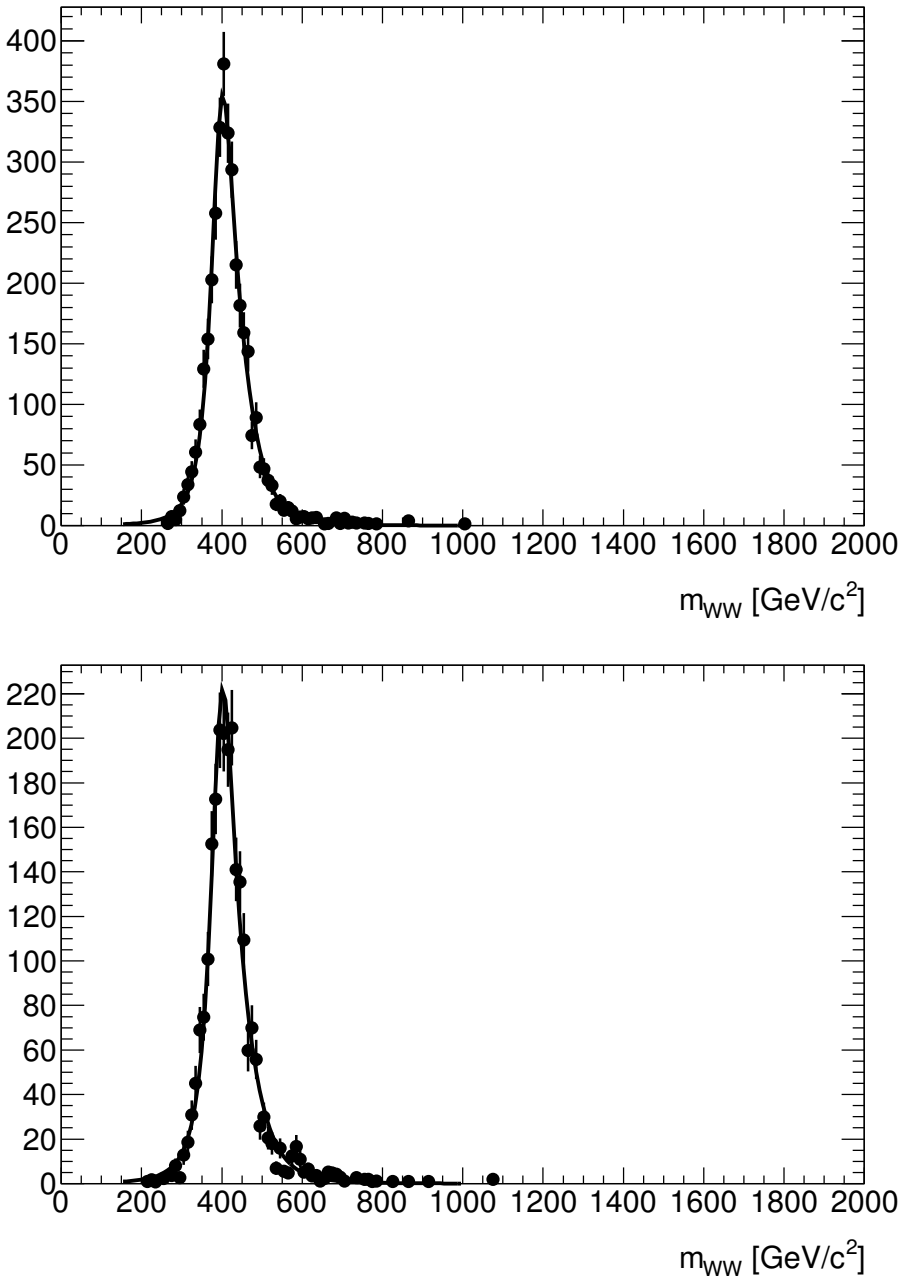

Figure 4.11: Fits of the signal model to the gluon fusion Monte Carlo in the $H + 0j$ (top) and $H + 1j$ (bottom) for $H \to WW^* \to e\nu jj$ selection. The true Higgs boson mass of the Monte Carlo sample was 400 GeV [55].

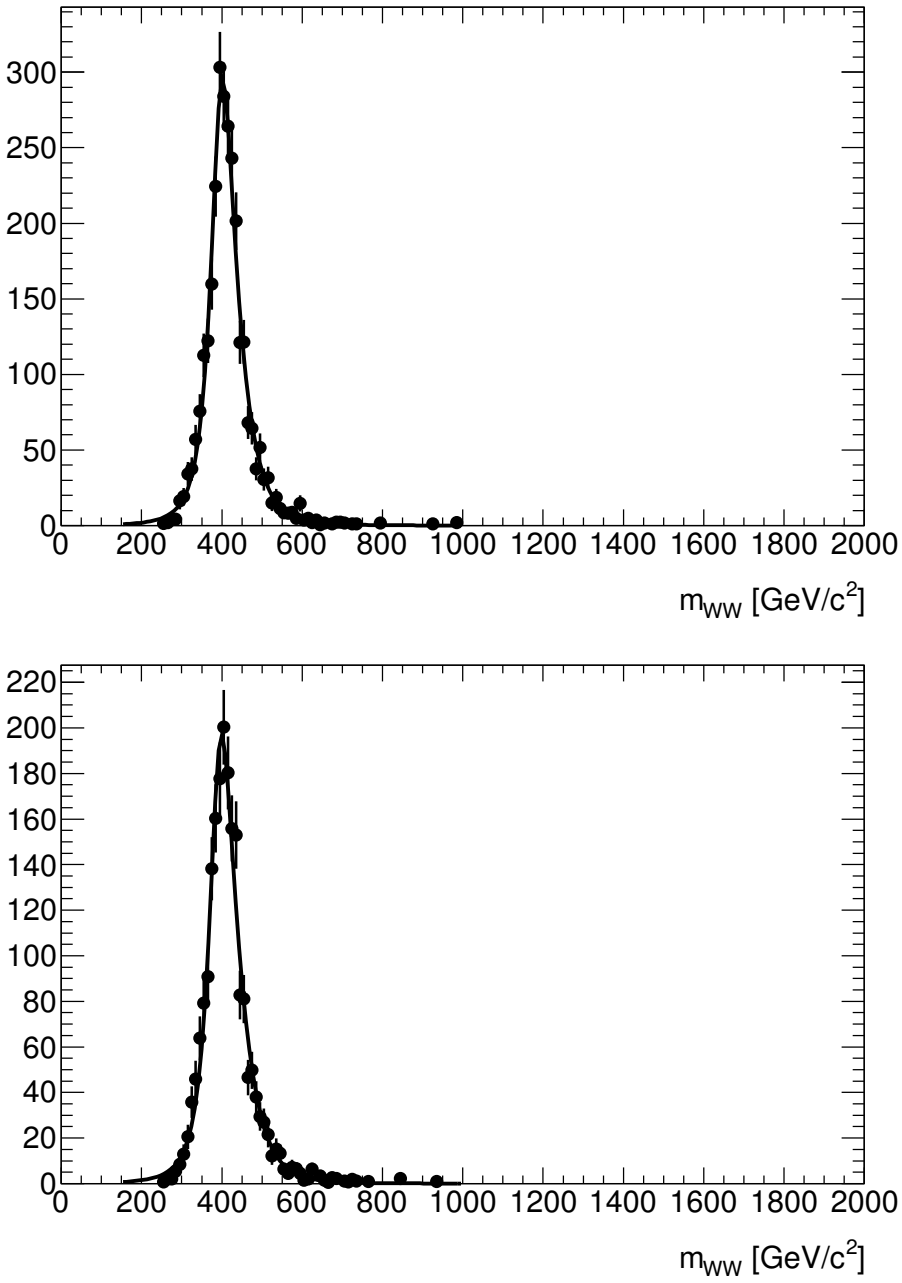

Figure 4.12: Fits of the signal model to the gluon fusion Monte Carlo in the $H + 0j$ (top) and $H + 1j$ (bottom) for $H \to WW^* \to \mu\nu jj$ selection. The true Higgs boson mass of the Monte Carlo sample was 400 GeV [55].

4.8 Statistical Interpretation

The Higgs boson signal is expected to appear as a relatively narrow peak in the $m(\ell\nu jj)$ distribution. The present search is restricted to $m_H > 300$ GeV in order to have a smoothly varying non-resonant background and limited to $m_H < 600$ GeV. For higher Higgs boson masses, the jets from $W \to jj$ decay began to overlap due to the large boost of the W boson and the natural width of the Higgs boson which exceeds 100 GeV, so this analysis is further limited to $m_H < 600$ GeV. Limits are set using a binned maximum likelihood fit to the shape of the observed $m(\ell\nu jj)$ distribution in the range $300 < m(\ell\nu jj) < 600$ GeV. Its width, before detector effects, varies from about 10 GeV at $m_H = 300$ GeV to about 70 GeV at $m_H = 550$ GeV. The non-resonant background for the $\ell\nu jj + 0/1j$ channel is modeled by a smooth function of the form $f(x) = [1/(1 + |a(x - m)|^b)] \times \exp[-c(x - 200)]$, where x is the m_{WW^*} in GeV and a, b, c and m are free parameters with the appropriate units. The parameters of the fit function in each of these models are not subjected to any external constraint. The functional form for the background is motivated by studies using Monte Carlo simulation, and is tested by fits to the $m(\ell\nu jj)$ distributions obtained by selecting events in sidebands, with m_{jj} just below ($45 < m_{jj} < 60$ GeV) or just above ($100 < m_{jj} < 115$ GeV) the W boson peak. In Figures 4.13 and 4.14, fits of these data to the background model are shown for $H + 0j$ and $H + 1j$ channels. The good χ^2 probability of these fits provides

support for the background functional form used in this analysis.

Higgs boson signal is modeled using a function of the form $1/(a+(x-m_1)^2+b(x-m_2)^4)$, where $x = m_{WW^*}$ is measured in GeV, a, b, m_1, m_2 are parameters determined from a fit to the Monte Carlo simulation of the expected Higgs boson signal at each Higgs boson mass point. The $m(l\nu jj)$ fractional resolution is $(8.8 \pm 1.3)\%$ at $m_H = 400$ GeV, the uncertainties mostly arising from $E_{\mathrm{T}}^{\mathrm{miss}}$ and jet energy scale [44] and jet energy resolution [56], and shows a $1/\sqrt{m_H}$ dependence over the range of this analysis. Figure 4.11 shows the fits to the gluon-gluon fusion signal Monte Carlo at Higgs mass point 400 GeV in the $H+0j$ and $H+1j$ channel for $H \to WW^* \to e\nu jj$ selection. Figure 4.12 shows similar result for $H \to WW^* \to \mu\nu jj$ selection. Appendix E gives the fits to the signal Monte Carlo samples at each Higgs mass point used in this analysis.

All parameters which control the shape of the background are free parameters in the fit. The data are separated into categories based on jet multiplicity and lepton flavor; the background shape parameters in all the different categories are allowed to float independently in the fit. The background normalization is described by a separate normalization parameter for each jet multiplicity bin (each of which is common to the two lepton flavor categories in that bin) and separate normalization parameters for the electron and muon efficiencies (each of which is common to all jet multiplicity bins). The relative normalization of the signal in the various jet multiplicity bins is taken from Monte Carlo, but the expected signal yield in the electron and muon categories depends on the

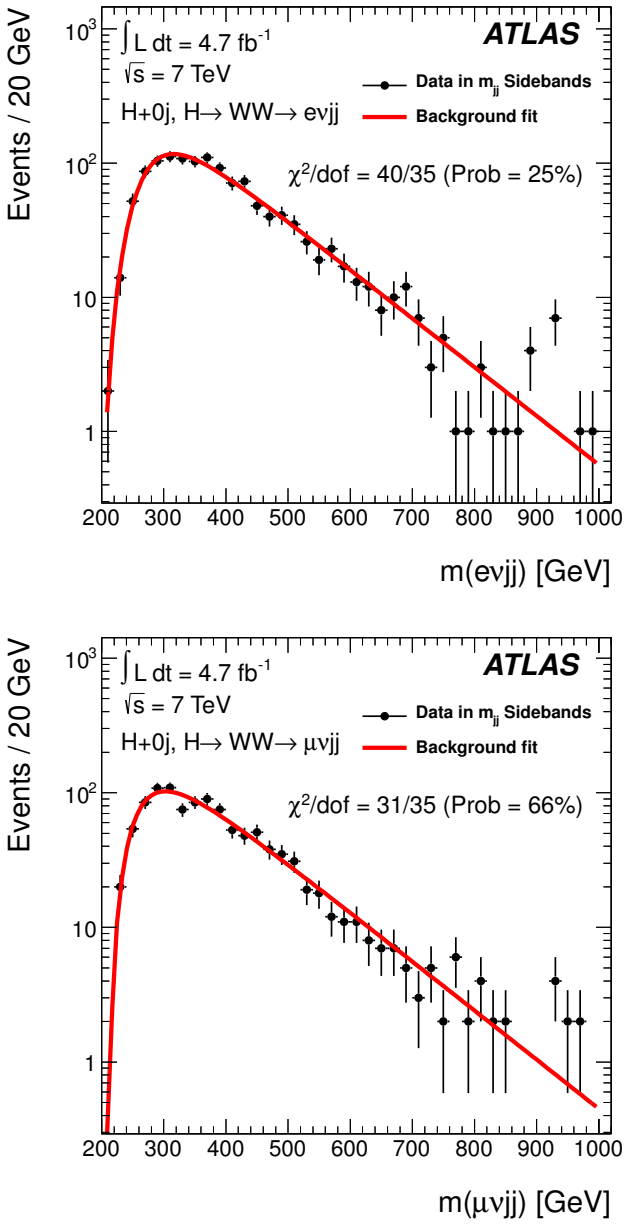

Figure 4.13: Fits of the background model described in the text to the reconstructed invariant mass $m(\ell\nu jj)$ when m_{jj} is in the W sidebands for the $\ell\nu jj+0j$ selection. The upper figure shows the electron channel distribution and lower figure shows the muon channel distribution. The χ^2/dof and χ^2 probability of these fits are also shown in the figure [18].

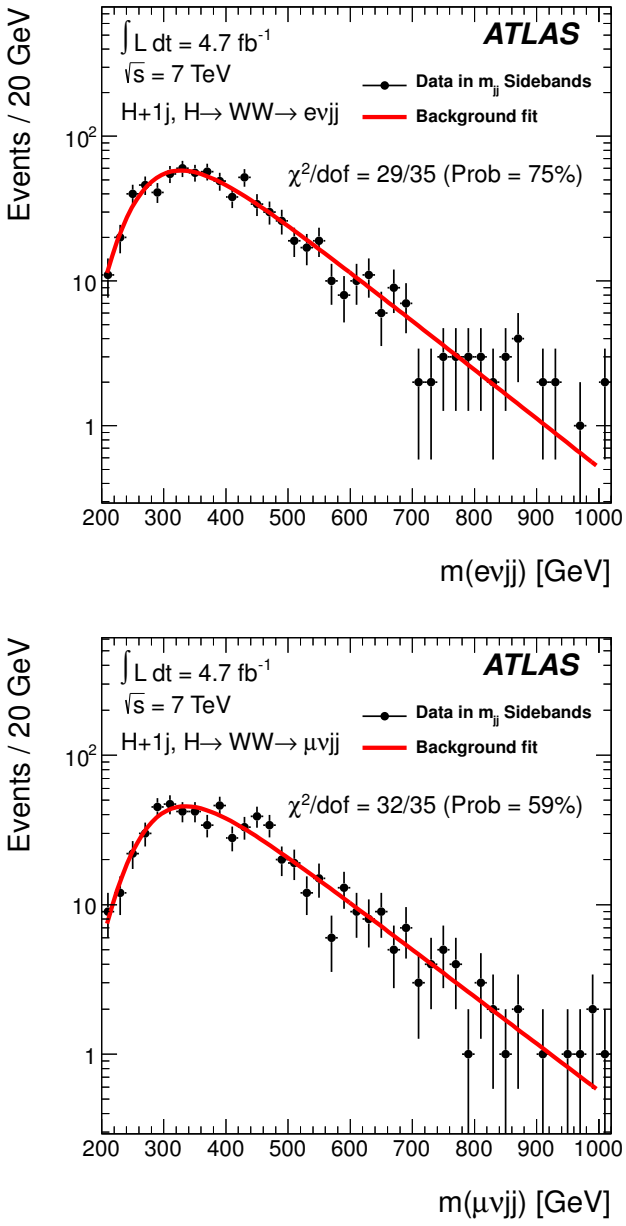

Figure 4.14: Fits of the background model described in the text to the reconstructed invariant mass $m(\ell\nu jj)$ when m_{jj} is in the W sidebands for the $\ell\nu jj+1j$ selection. The upper figure shows the electron channel distribution and lower figure shows the muon channel distribution. The χ^2/dof and χ^2 probability of these fits are also shown in the figure [18].

efficiency parameters in the same way that the background model does. A global scale factor μ multiplies the expected signal yield in all categories, and is defined so that $\mu = 1$ corresponds to the Standard Model prediction.

4.9 Systematic Uncertainties

The systematic uncertainty due to the background modelling is included by treating the uncertainties on the background model parameters resulting from fits to the data as nuisance parameters in the statistical interpretation of the data. Both the background model and the sum of signal and background models are found to be good fits to the data. For $m_H = 400$ GeV, the χ^2 probabilities are 33% and 31% for the background-only and background-plus-signal fits, respectively. Therefore, alternative parameterizations of the background expectation that are consistent with the data will also be consistent with the background model within its uncertainties. This is tested by fitting both the signal region and the sideband regions of the data with two alternative parameterizations that use polynomials of varying order to describe the decreasing background component instead of exponential functions. Differences in the fitted background yield between these parameterizations and the nominal background model are less than 5%, while the uncertainty from the nuisance parameters and statistical uncertainty is 10-12%.

The remaining systematic uncertainties are related to the Higgs boson signal.

The fit includes nuisance parameters which account for the uncertainty in the reconstruction efficiency. The trigger efficiencies, the electron and muon reconstruction efficiencies, lepton energy resolution and scale are varied within their uncertainties, giving an uncertainty in the signal efficiency of less than 1%. Varying the jet energy scale [44] within its uncertainties yields an uncertainty of up to 8% in the expected signal in the $\ell\nu jj + 0/1j$ channel for $m_H \geqslant$ 400 GeV. Smearing the jet energies within the uncertainty on their resolutions (**Appendix D**) results in a signal uncertainty of 7% for $m_H = 400$ GeV and 5% for $m_H = 600$ GeV [57]. The reconstructed $E_{\mathrm{T}}^{\mathrm{miss}}$ [58] is also affected by the uncertainties on the energy scales and resolutions of reconstructed leptons and jets. The signal uncertainties given above include the propagation of these effects to the reconstructed $E_{\mathrm{T}}^{\mathrm{miss}}$. The propagation to $E_{\mathrm{T}}^{\mathrm{miss}}$ adds a small contribution to the overall signal uncertainty. In addition, a 7% uncertainty on the degradation of the $E_{\mathrm{T}}^{\mathrm{miss}}$ resolution and scale due to pile-up effects is estimated, which results in a negligible uncertainty on the signal efficiency. The uncertainty on the b-tagging efficiency (**Appendix C**) gives a maximum uncertainty of 8% on the signal efficiency [45] and shows no strong dependence on m_H or the selection criteria.

The uncertainties on jet energy resolution and jet energy scale, which also have an impact on $E_{\mathrm{T}}^{\mathrm{miss}}$, lead to systematic uncertainties on the Higgs boson mass resolution (5%) and on the Higgs boson mass scale (2%). These uncertainties are not included since their effect on the fitted Higgs boson yield is considerably

smaller than the systematic uncertainty on the signal acceptance due to jet energy scale and resolution.

The Higgs boson signal expectation includes a 3.9% systematic uncertainty due the luminosity determination [59] and a 19.4% uncertainty on the predicted Higgs boson cross section [60], taken to be independent of the mass. Off-shell effects and interference between the signal and background processes are discussed in Refs. [60, 61, 62]. To account for the uncertainties from these effects, an uncertainty of $150\% \times m_H^3$ (m_H in TeV) on the signal cross section is included in the statistical interpretation of the data, where the m_H^3 form is motivated by the scaling of the Higgs boson width with m_H and the normalization factor of 150% is chosen to give $\sim$30% at $m_H = 600$ GeV [60].

4.10 Results

The fit, described in section 4.8, includes nuisance parameters which account for the uncertainty in the efficiency of the electron, muon, and jet reconstruction as described in section 4.9. Since no Higgs boson was found, limits on the production cross-section of the Higgs boson production have been presented below.

4.10.1 Limits on Higgs boson production

Limits are extracted using the Profile Likelihood [63] and following the CL_s procedure described in Ref. [64]. This method uses the likelihood function,

defined in Equation 4.7, as a test statistic. The limit setting procedure performs a hypothesis test between the null hypothesis, H_0, which is the background-only model and the alternative hypothesis, H_1, which is the signal plus background model. The parameter of interest (the signal cross section) in the model being considered can be determined by maximising this likelihood ratio. To determine the expected limit, this may be performed for a number of pseudo-experiments with the number of signal and background events Poisson fluctuated and for a range of different hypothesized values of the parameter of interest. From this the expected 95% C.L. limit may be extracted.

The H + 0j and H + 1j channels are treated as separate analyses and are then combined by multiplying their likelihood functions to give a combined likelihood:

$$L(\mu) = L_{global} \times L_{H+0j}(\mu) \times L_{H+1j}(\mu) \tag{4.7}$$

In this equation, L_{global} constrains the nuisance parameters which model the global systematic uncertainties (described in section 4.9) which affect all channels. μ parameterises the signal strength, which is assumed to be the same in each of the jet channels. It is this parameter which the limit setting procedure aims to extract and in this case it is expressed as a ratio of the observed cross section to the expected SM Higgs boson production cross section.

The likelihood function is maximised twice to calculate the likelihood ratio

$\tilde{\lambda}(\mu)$:

$$\tilde{\lambda}(\mu) = \begin{cases} \frac{L(\mu,\hat{\hat{\theta}}(\mu))}{L(\hat{\mu},\hat{\theta})} & \text{if } \hat{\mu} \geq 0 \\ \frac{L(\mu,\hat{\hat{\theta}}(\mu))}{L(0,\hat{\hat{\theta}}(0))} & \text{if } \hat{\mu} < 0 \end{cases} \tag{4.8}$$

Here $\hat{\hat{\theta}}(0)$ and $\hat{\hat{\theta}}(\mu)$ refer to the conditional maximum-likelihood estimators of θ for strength parameters 0 or μ, respectively. $\hat{\theta}$ represents the preferred set of nuisance parameters extracted from the fit where $\hat{\hat{\theta}}$ represents the same quantity from the second fit.

The parameters are allowed to wander freely within their uncertainties after the likelihood function is maximised and a best fit value of signal strength, $\hat{\mu}$ is extracted. The second time, the signal strength μ is constrained by $\hat{\mu}$ to give an estimator $\tilde{q}(\mu)$:

$$\tilde{q}(\mu) = \begin{cases} -2\ln\hat{\lambda}(\mu) & \text{if } \hat{\mu} < \mu \\ 0 & \text{if } \hat{\mu} > \mu \end{cases} = \begin{cases} -2\ln\frac{L(\mu,\hat{\hat{\theta}}(\mu))}{L(0,\hat{\hat{\theta}}(0))} & \text{if } \hat{\mu} < 0 \\ -2\ln\frac{L(\mu,\hat{\hat{\theta}}(\mu))}{L(\hat{\mu},\hat{\theta})} & \text{if } 0 \leq \hat{\mu} \leq \mu \\ 0 & \text{if } \hat{\mu} > 0 \end{cases} \tag{4.9}$$

The probability density function (PDF) $f(\tilde{q}_\mu|\mu,\hat{\hat{\theta}}(\mu))$ is constructed using top Monte Carlo for signal strength μ. The p-value, which expresses the probability that a given test statistic is at least as extreme as the observed test statistic under the assumption that the null hypothesis is true (and the Higgs boson does not exist), is calculated. If the Higgs boson did exist, a small p-value would

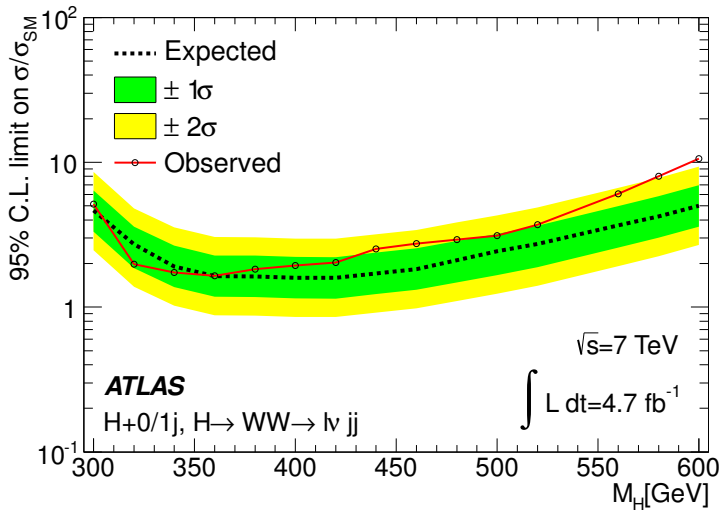

Figure 4.15: 95% C.L. limits for the $H + 0/1j$ channel in units of the Standard Model prediction for an integrated luminosity of 4.7 fb^{-1} [18].

indicate that it was extremely unlikely that the observed number of events was consistent with the SM. To quantify the level of disagreement between the data and the null hypothesis ($\mu = 0$) using the observed value of q_0, we compute the p_0-value

$$p_0 = \int_{q_0,obs}^{\infty} f(q_0|0)dq_0 \tag{4.10}$$

The p-value for signal strength μ is given by:

$$p_\mu = \int_{\tilde{q}(\mu),obs}^{\infty} f(\tilde{q}_\mu|\mu, \hat{\hat{\theta}}(\mu))d\tilde{q}(\mu) \tag{4.11}$$

To obtain a 95% C.L., iterations are performed with an assumed signal strength of μ to obtain $p_{up} \leq 5\%$ to give a value of μ_{up}. The expected median, μ_{med}, is extracted in a similar fashion using background-only toy MC. The $\pm 1\sigma$

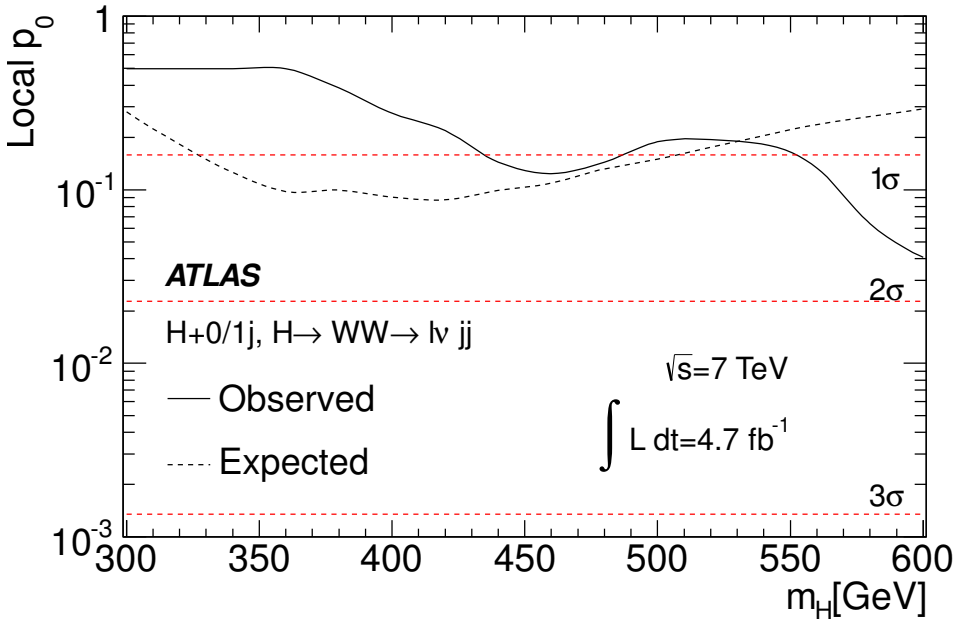

Figure 4.16: Local p_0 for the $H + 0/1j$ search [18].

and $\pm 2\sigma$ bands can also be obtained this way. There is a chance that the null hypothesis may be wrongly excluded in cases where the expected and observed number of events is very small and statistical fluctuations could have a large effect. To avoid this, if the observed limit fluctuates beneath the $\mu_{med} - 1\sigma$ band, the quoted limit is given as $\mu_{med} - 1\sigma$ instead of the observed smaller value. This is known as a Power Constrained Limit (PCL) [65, 66].

Figure 4.16 shows the expected and observed local p_0 values, i.e. the probability to observe an excess at least as significant as the observed excess (or the expected excess in the Standard Model) if there is only background. There is no indication of any significant excess. The largest deviation from the background-only expectation occurs in the $H + 0/1j$ channel at $m_H = 600$ GeV, with a local

significance of about 1.8σ.

Figure 4.15 shows the 95% CL upper bound on the cross-section times branching ratio for Higgs production with respect to the Standard Model prediction, $\sigma \times BR_{H\to WW^*}/(\sigma \times BR_{H\to WW^*})_{\mathrm{SM}}$, as a function of m_H. In the combined $H+0j$ and $H+1j$ channels, the observed limit on $H \to WW^*$ production by gluon fusion for $m_H = 400$ GeV is 2.2 pb, or 1.9 times the SM prediction.

Chapter 5

Summary and Conclusions

A search for the SM Higgs boson has been performed in the $H \to WW^* \to \ell\nu jj$ channel using 4.7 fb^{-1} of pp collisions data at $\sqrt{s} = 7$ TeV recorded by the ATLAS detector. No significant excess of events over the expected SM background has been observed [18]. Search of Higgs boson using $H \to WW^* \to \ell\nu jj$ channel is sensitive to high mass Higgs boson. In the low mass range ($m_H <$ 240 GeV), it is difficult to search for Higgs boson in this channel due to large W+Jets and QCD backgrounds.

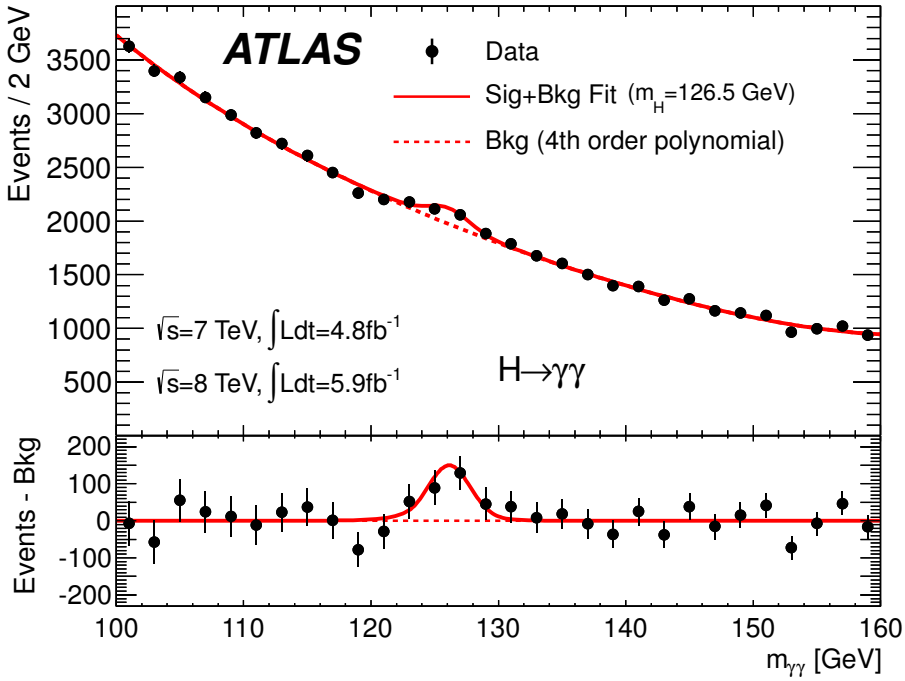

Figure 5.1: The distributions of the invariant mass of diphoton candidates for the combined 7 TeV and 8 TeV data sample [1].

However, after combining $\sqrt{s} = 7$ TeV and $\sqrt{s} = 8$ TeV data samples, Both

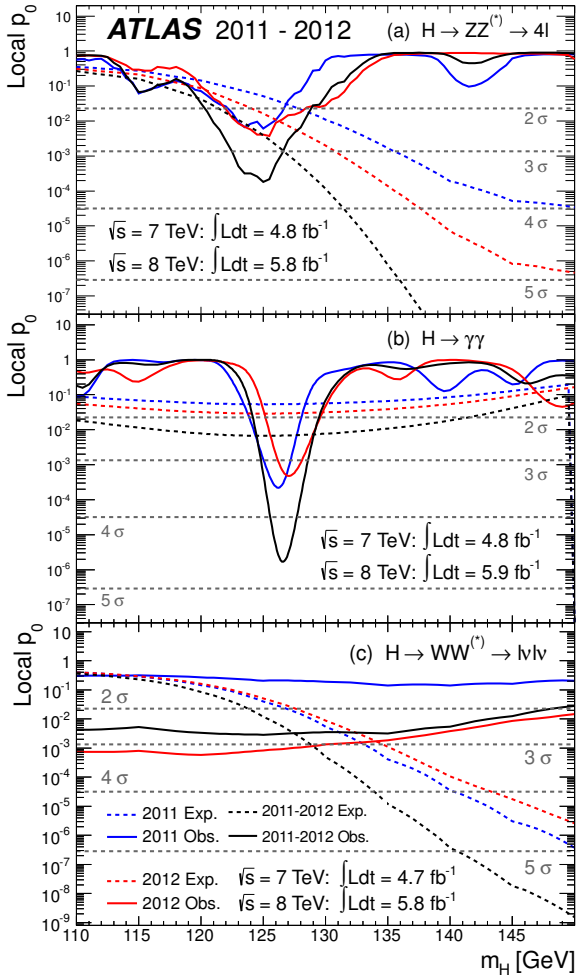

Figure 5.2: The observed local p_0 as a function of the hypothesized Higgs boson mass for the (a) $H \to ZZ^* \to \ell\ell\ell\ell$, (b) $H \to \gamma\gamma$ and (c) $H \to WW^* \to \ell\nu\ell\nu$ channels. The dashed curves show the expected local p_0 under the hypothesis of a SM Higgs boson signal at that mass. Results are shown separately for the $\sqrt{s}$ =7 TeV data (dark, blue), the $\sqrt{s}$ = 8 TeV data (light, red), and their combination (black) [1].

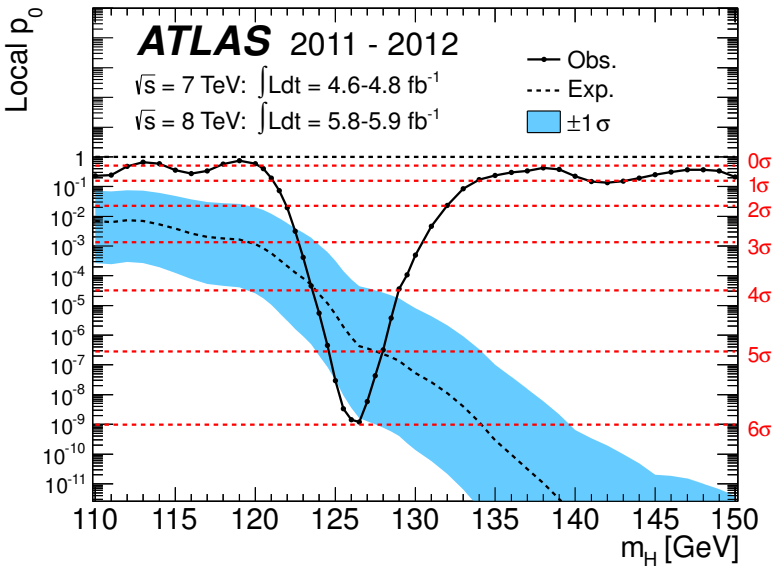

Figure 5.3: The observed (solid) local p_0 as a function of m_H in the low mass range. The dashed curve shows the expected local p_0 under the hypothesis of a SM Higgs boson signal at that mass with its $\pm 1\sigma$ band. The horizontal dashed lines indicate the p-values corresponding to significances of 1 to 6 σ [1].

ATLAS and CMS collaboration have observed excess of events near $m_H = 126$ GeV in the $H \to \gamma\gamma$ and $H \to ZZ^* \to \ell\ell\ell\ell$ channels, both of which provide fully reconstructed candidates with high resolution in invariant mass [1, 2]. Figure 5.1 shows the reconstructed Higgs boson mass in $H \to \gamma\gamma$ channel using the ATLAS detector.

Figures 5.2a and 5.2b. These excesses are confirmed by the highly sensitive but low-resolution $H \to WW^* \to \ell\nu\ell\nu$ channel, as shown in Figure 5.2c.

The largest local significance p_0 for the combination of the 7 and 8 TeV data is found for a SM Higgs boson mass $m_H = 126.5$GeV, where it reaches 6.0 σ, with an expected value in the presence of a SM Higgs boson signal at that mass of 4.9 σ (figure 5.3). For the 2012 data alone, the maximum local significance for the $H \to ZZ^* \to \ell\ell\ell\ell$, $H \to \gamma\gamma$ and $H \to WW^* \to \ell\nu\ell\nu$ channels combined is 4.9 σ, and occurs at $m_H = 126.5$ GeV (compared to expected 3.8 σ). The observed significance of the excess is mildly sensitive to uncertainties in the energy resolutions and energy scale systematic uncertainties for photons and electrons; the effect of the muon energy scale systematic uncertainties is negligible. After taking into consideration these uncertainties, the local significance reduces to 5.9 σ.

So far, the observed Higgs boson is consistent with the SM predicted Higgs boson. However, we do not know what is the hidden in the nature. There is compelling demand for the physics beyond the SM. If there is any Higgs in the high mass range, $H \to WW^* \to \ell\nu jj$ channel may be able to detect it.

References

[1] ATLAS Collaboration, *Observation of a new particle in the search for the Standard Model Higgs boson with the ATLAS detector at the LHC*, **Phys. Lett. B, 716(2012), 1-29**.

[2] CMS Collaboration, *Observation of a new boson at a mass of 125 GeV with the CMS experiment at the LHC*, **Phys. Lett. B, 716(2012), 30-61**.

[3] S. L. Glashow, *Partial symmetries of weak interactions*, Phys. Lett., **12**, (1964), 132.

[4] P. W. Higgs, *Broken symmetries, massless particles and gauge fields*, Phys. Lett., **12**, (1964), 132.

[5] P. W. Higgs, *Broken Symmetries and the Masses of Gauge Bosons*, Phys. Rev. Lett. **13** (1964), 508.

[6] G. U. of Fundamental Forces, *in Elementary Particle Theory, p. 367*. Almqvist and Wiksell, Stockholm, 1968.

[7] S. Weinberg, *A Model of Leptons*, Phys. Rev. Lett. **19** (1967), 1264.

[8] P. W. Higgs, *Spontaneous Symmetry Breakdown without Massless Bosons*, Phys. Rev. **145** (1966), 1156.

[9] A. Salam, *Gauge Unification of Fundamental Forces*, *http : //www.nobelprize.org/nobel$_p$rizes/physics/laureates/1979/salam − lecture.html*.

[10] C. Rubbia, *Experimental observation of the intermediate vector bosons W^+, W^- and Z*, Rev. Mod. Phys. **57** (1985), 699.

[11] U. Mossel, *Fields, Symmetries, and Quarks*, Springer-Verlag, Berlin, Germany **2nd edition** (1999) .

[12] P. Langacker, *Introduction to the Standard Model and Electroweak Physics*, `arXiv:0901.0241v1 [hep-ph]`.

[13] LHC Higgs Cross Section Working Group, S. Dittmaier, C. Mariotti, G. Passarino, and R. Tanaka (Eds.), *Handbook of LHC Higgs cross sections: 1. Inclusive observables*, `arXiv:1101.0593 [hep-ph]`.

[14] Ulrik Egede, *The search for a standard model Higgs at the LHC and electron identification using transition radiation in the ATLAS tracker*, http://www.hep.lu.se/atlas/thesis/egede/thesis-node39.html.

[15] Dilip Kumar Jana, *Search for Standard Model Higgs Boson in* $H \to WW \to \ell\nu jj$ *decay using* $1.04 fb^{-1}$ *of data recorded by the ATLAS Detector in pp Collision at* $\sqrt{s} = 7$ *TeV*, http://www.springerlink.com/content/67323636n73t8336.

[16] Jana, Dilip, *Search for Standard Model Higgs Boson in* $H \to WW \to \ell\nu jj$ *decay using* $1.04 fb^{-1}$ *of data recorded by the ATLAS Detector in pp Collision at* $\sqrt{s} = 7$ *TeV*, ATL-COM-PHYS-2011-1048, https://cdsweb.cern.ch/record/1374163/.

[17] ATLAS Collaboration, *Search for the Higgs Boson in the* $H \to WW \to \ell\nu jj$ *Decay Channel in pp Collisions at* $\sqrt{s} = 7$ *TeV with the ATLAS Detector*, Phys. Rev. Lett., **107**, (2012), 231801.

[18] ATLAS Collaboration, *Search for the Higgs Boson in the* $H \to WW \to \ell\nu jj$ *Decay Channel in pp Collisions at* $\sqrt{s} = 7$ *TeV with the ATLAS Detector*, Physics Letters **B** (2012), http://dx.doi.org/10.1016/j.physletb.2012.10.066.

[19] Jana, D. et.al.; Collaboration, *Search for the Higgs Boson in the* $H \to WW \to \ell\nu jj$ *decay channel using 4.7 fb-1 of pp collisions at* $\sqrt{s} = 7$ *TeV with the ATLAS Detector*, **ATL-COM-PHYS-2012-466**.

[20] L. Evans and P. Bryant, *LHC Machine*, JINST, 3(08):S08001, 2008.

[21] ATLAS Collaboration, *The ATLAS Experiment at the CERN Large Hadron Collider*, **JNIST, 3:S08003(2008)**.

[22] CMS Collaboration, *The CMS experiment at the CERN LHC*, **JINST, 3:S08004, 2008**.

[23] ALICE Collaboration, *The ALICE experiment at the CERN LHC*, **JINST, 3:S08002, 2008**.

[24] LHCb Collaboration, *The LHCb Detector at the LHC*, **JINST, 3:S08004, 2008**.

[25] ATLAS Collaboration, *Detector and Physics Performance Technical Design Report*, Tech. Rep. CERN/LHCC 99-14, CERN, Geneva, 1999.

[26] ATLAS Collaboration, *The ATLAS superconducting magnet system at the Large Hadron Collider*, Physica C, **468**, 21372142.

[27] The ATLAS Collaboration, *Level-1 Trigger*, Tech. Rep. ATLAS TDR-12, CERN, Geneva, 1998.

[28] I. Bird et al., *LHC computing Grid. Technical design report.*, CERN-LHCC 2005-024 (2005).

[29] ATLAS Collaboration, *The ATLAS Simulation Infrastructure*, Eur. Phys. J. C **70**, 823-874 (2010).

[30] S. Agostinelli et al., *Geant4 - a simulation toolkit.*, Nucl. Inst. Meth. **A506**, (2003) 250303.

[31] J. Allison et al., *Geant4 Developments and Applications*, IEEE Transactions on Nuclear Science 53, (2006) 270278.

[32] ATLAS Collaboration, *Luminosity determination in pp collisions at* $\sqrt{s} =$ *7 TeV using the ATLAS detector at the LHC*, Eur. Phys. J., **C71** (2011) 1630.

[33] ATLAS Collaboration, *ATLAS Forward Detectors for Luminosity Measurement and Monitoring*, CERN/LHCC/2004-010 (2004).

[34] H. M. Gray, *The Charged Particle Multiplicity at Center of Mass Energies from 900 GeV to 7 TeV measured with the ATLAS Experiment at the Large Hadron Collider*, http://cds.cern.ch/record/1309943.

[35] ATLAS Collaboration, *Calorimeter Clustering Algorithms: Description and Performance*, **ATL-LARG-PUB-2008-002 (2008)**, **https://cdsweb.cern.ch/record/1099735?ln=en**.

[36] S. Hassini et al., *A muon identification and combined reconstruction procedure for the ATLAS detector at the LHC using the (MUONBOY, STACO, MuTag) reconstruction packages*, NIM A, 572.

[37] S. Catani et al., *Longitudinally invariant K(t) clustering algorithms for hadron hadron collisions*, Nucl. Phys. **B 406** (1993) 187.

[38] M. Cacciari et al., *Anti-KT jet clustering Algorithm*, JHEP, **0804** (2008) 063.

[39] M. Cacciari et al., *Dispelling the N3 myth for the Kt jet-finder*, Phys. Lett., **B641** (2006) 57.

[40] Tev4LHC Higgs working group, *Standard Model Higgs cross sections at hadron colliders*, http://maltoni.home.cern.ch/maltoni/TeV4LHC/SM.html.

[41] M. Hance, D. Olivito, and H. Williams, *Performance Studies for e/gamma Calorimeter Isolation*, Tech. Rep. ATL-COM-PHYS-2011-1186, CERN, Geneva, Sep, 2011.

[42] ATLAS Collaboration, T. A. Collaboration, *Electron performance measurements with the ATLAS detector using the 2010 LHC proton-proton collision data*, arXiv:1110.3174 [hep-ex]. arXiv: 1110.3174, submitted to PLB.

[43] ATLAS Collaboration Collaboration, *Muon reconstruction efficiency in reprocessed 2010 LHC protonproton collision data recorded with the ATLAS detector*, ATLAS-CONF-2011-063, http://cdsweb.cern.ch/record/1345743.

[44] ATLAS Collaboration, *Jet energy scale and its systematic uncertainty for jets produced in proton-proton collisions at $\sqrt{s}$=7 TeV and measured with the ATLAS detector*, ATLAS-CONF-2010-056 (2010).

[45] The ATLAS Collaboration Tech. Rep. ATLAS-CONF-2011-089.

[46] ATLAS Collaboration, *LAr Correction*, https://twiki.cern.ch/twiki/bin/viewauth/Atlas/LArEventVetoRel17.

[47] ATLAS Collaboration, *Measurement of the b-tag efficiency in a sample of jets containing muons with 5 fb^{-1} of data from the ATLAS detector*, **ATLAS-CONF-2012-043**, **https://cdsweb.cern.ch/record/1435197**.

[48] ATLAS Collaboration, *Measurement of the mistag rate of b-tagging algorithms with 5 fb^{-1} of data collected by the ATLAS detector*, **ATLAS-CONF-2012-040**, **https://cdsweb.cern.ch/record/1454675**.

[49] M. L. Mangano et al., *ALPGEN, a generator for hard multi-parton processes in hadronic collisions*, JHEP **0307** (2003) 001, hep-ph/0206293.

[50] S. Frixione and B. Webber, *Matching NLO QCD and parton showers in heavy flavour production*, JHEP **0308** (2003) 007, hep-ph/0305252.

[51] G. C. et al., *HERWIG 6: an event generator for hadron emission reactions with interfering gluons (including super-symmetric processes)* , JHEP **0101** (2001) 010.

[52] J. Alwall et al., *MadGraph/MadEvent v4: The New Web Generation*, JHEP **0709** (2007) 028, arXiv:0706.2334 [hep-ph].

[53] P. Nason and C. Oleari, *NLO Higgs boson production via vector-boson fusion matched with shower in POWHEG*, JHEP **1002** (2010) 037, arXiv:0911.5299 [hep-ph].

[54] T. Sjostrand, S. Mrenna, and P. Z. Skands, *PYTHIA 6.4 physics and manual*, JHEP **0605** (2006) 026.

[55] Jana, D. et.al.; Collaboration, *A Search for the Higgs boson in the $H \to WW \to \ell\nu jj$ decay mode using 4.7 fb^{-1} of data collected with the ATLAS detector at $\sqrt{s} = 7$ TeV.*, **ATL-COM-PHYS-2012-401**.

[56] ATLAS Collaboration, *Jet energy resolution and selection efficiency relative to track jets from in-situ techniques with the ATLAS Detector Using Proton-Proton Collisions at a Center of Mass Energy $\sqrt{s} = 7$ TeV*, **ATLAS-CONF-2010-054**, **http://cdsweb.cern.ch/record/1281311?ln=en**.

[57] ATLAS Collaboration, T. A. Collaboration Tech. Rep. ATLAS-CONF-2010-054.

[58] ATLAS Collaboration, T. A. Collaboration Tech. Rep. ATLAS-CONF-2010-057.

[59] The ATLAS Collaboration Tech. Rep. ATLAS-CONF-2011-116.

[60] LHC Higgs Cross Section Working Group, S. Dittmaier, C. Mariotti, G. Passarino, and R. Tanaka (Eds.), *Handbook of LHC Higgs cross sections: 2. Differential distributions*, arXiv:1201.3084 [hep-ph].

[61] C. Anastasiou, S. Buehler, F. Herzog, and A. Lazopoulos, *Total cross section for Higgs boson hadroproduction with anomalous Standard Model interactions*, JHEP **12** (2011) 058, arXiv:1107.0683 [hep-ph].

[62] K. R. E. J. M. Campbell and C. Williams, *Gluon-gluon contributions to W+ W- production and Higgs interference effects*, arXiv:1107.5569 (2011).

[63] G. Cowan, K. Cranmer, E. Gross, and O. Vitells, *Asymptotic formulae for likelihood-based tests of new physics*, arXiv:1007.1727v2.

[64] A. L. Read, *Modified frequentist analysis of search results (the CL_s method)*. http://cdsweb.cern.ch/record/451614/files/p81.pdf.

[65] G.J. Feldman and R.D. Cousins, *Unified approach to the classical statistical analysis of small signals*, Phys. Rev. **D 57**, 38733889 (1998).

[66] E. G. G. Cowan, K. Cranmer and O. Vitells, *Power-Constrained Limits*, arXiv:1105.3166 [hep-ph].

Appendix A

Poster presented in the Lepton Photon conference in Mumbai, India (2011)

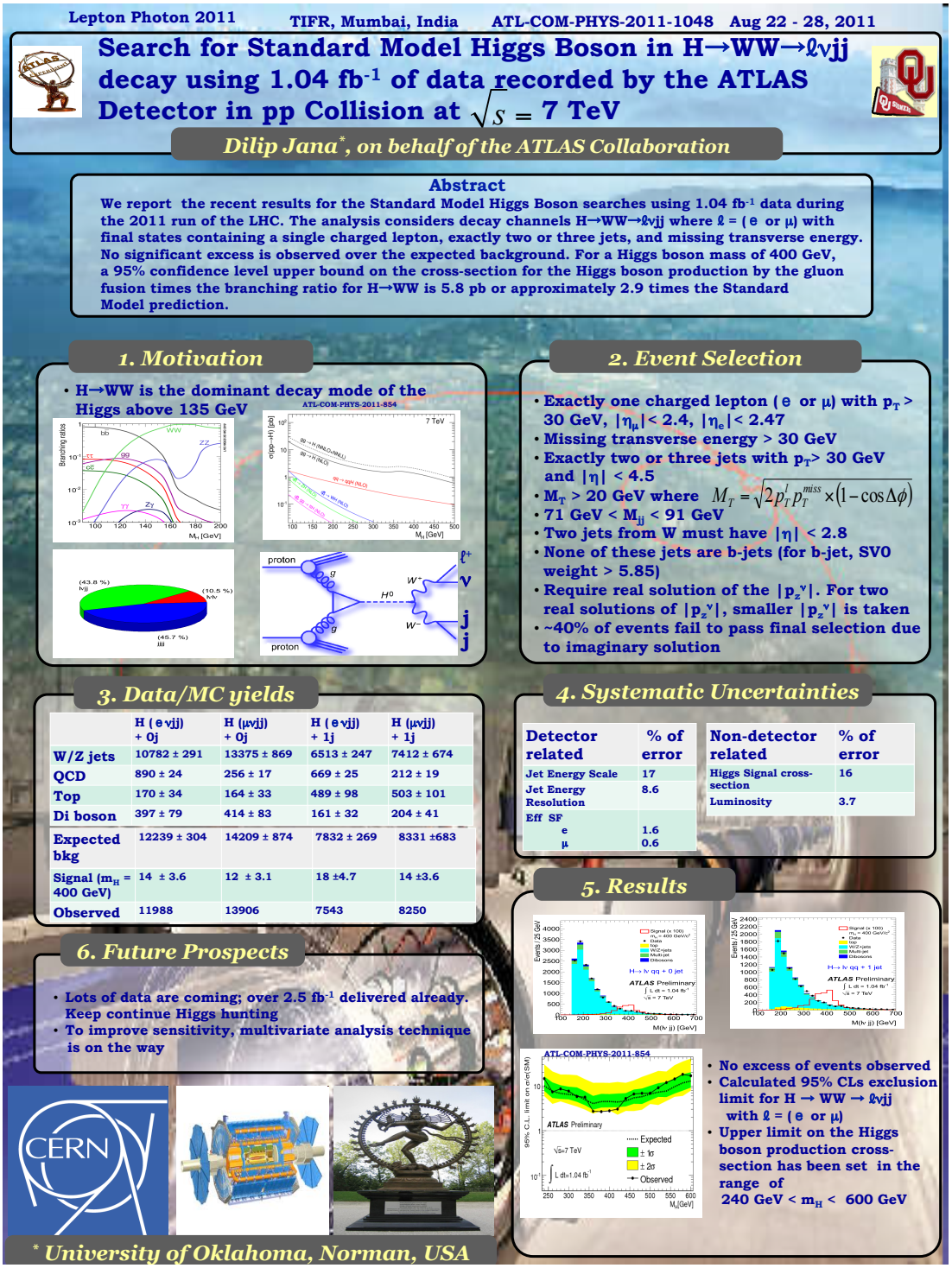

Best Poster Award

This is to certify that

Dilip Kumar JANA

has won Best Poster Award at the
XXV International Symposium on Lepton Photon Interactions at High Energies
(Lepton Photon 2011) held from 22-27 August 2011 at the
Tata Institute of Fundamental Research, Mumbai.

Prof.Naba.K.Mondal
Co-Chair, NOC
Lepton Photon 2011

Dr.Patricia McBride
Chairperson, IUPAP, C11

Prof.Rohini Godbole
Co-Chair, NOC
Lepton Photon 2011

LEPTON PHOTON 2011

Appendix B

Gluon-Gluon Fusion

The cross section for the basic gluon to Higgs process is

$$\begin{aligned}\hat{\sigma}(gg \to H) &= \frac{(2\pi)^4}{2m_H^2}\int \frac{1}{(2\pi)^3}\frac{d^3p}{2E}\delta^4(\vec{p}_{g1}+\vec{p}_{g2}-\vec{p})|M|^2 \\ &= \frac{8\pi^2\Gamma_{H\to gg}}{N_g^2 m_H}\int \frac{d^3p}{E}\delta^4(\vec{p}_{g1}+\vec{p}_{g2}-\vec{p}) \\ &= \frac{8\pi^2\Gamma_{H\to gg}}{N_g^2 m_H}\delta(\hat{s}-m_H^2)\end{aligned} \tag{B.1}$$

$N_g = 8$ the number of different gluons and $\hat{s} = x_1 x_2 s$ is the squared energy of the gluon pair.

We can calculate partial Higgs width $\Gamma_{H\to WW}$ by applying Feynman rule at HWW vertex shown in Figure B.1. The matrix element is

$$iM_{H\to WW} = \sum_{\lambda,\rho} ig\frac{m_W}{\cos\theta_W} g_{\mu\nu}\epsilon_{1\lambda}^{*\mu}\epsilon_{2\rho}^{*\nu} \tag{B.2}$$

where ϵ_1, ϵ_2 are the polarization vectors of the two W bosons with polarization

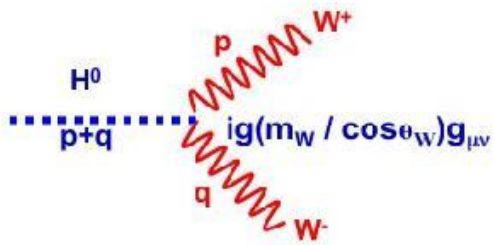

Figure B.1: $H \to WW$ vertex.

indices λ, ρ.

The differential decay rate for two body decay to two equal mass is given by

$$\frac{d\Gamma}{d\Omega} = \frac{\sqrt{\lambda(m_H^2, m_W^2, m_W^2)}}{64\pi^2 m_H^3}|M|^2 S \tag{B.3}$$

where

$$\sqrt{\lambda(m_H^2, m_W^2, m_W^2)} = m_H^2\sqrt{1 - (\frac{2m_W}{m_H})^2} \tag{B.4}$$

and

$$S = \prod_k n_k^{-1} = 1^{-1} = 1 \tag{B.5}$$

where n is the number of identical particles of type k.

The squared matrix element can be written as

$$|M|^2 = (\frac{gm_W}{\cos\theta_W})^2 \sum_{\lambda,\rho} g_{\mu\nu}\epsilon_{1\lambda}^{*\mu}\epsilon_{2\rho}^{*\nu} g_{\alpha\beta}\epsilon_{1\lambda}^{\alpha}\epsilon_{2\rho}^{\beta} \tag{B.6}$$

Using $\sum_\lambda \epsilon_\lambda^i \epsilon_\lambda^j = \delta^{ij}$, $\sum_\lambda \epsilon_\lambda^\mu \epsilon_\lambda^{*\nu}$ can be written as

$$\sum_\lambda \epsilon_\lambda^\mu \epsilon_\lambda^{*\nu} = -g^{\mu\nu} + \frac{p^\mu p^\nu}{m_W^2} \tag{B.7}$$

Using Figure B.1

$$\begin{aligned} m_H^2 &= (\vec{p} + \vec{q})^2 \\ &= p^2 + q^2 + 2\vec{p}.\vec{q} \\ &= 2m_W^2 + 2\vec{p}.\vec{q} \end{aligned} \tag{B.8}$$

Hence,

$$\vec{p}.\vec{q} = \frac{m_H^2 - 2m_W^2}{2} \tag{B.9}$$

$|M|^2$ can be simplified as

$$\begin{aligned}
|M|^2 &= (\frac{gm_W}{\cos\theta_W})^2 g_{\mu\nu}(-g^{\mu\alpha} + \frac{p^\mu p^\alpha}{m_W^2}) g_{\mu\nu}(-g^{\nu\beta} + \frac{q^\nu q^\beta}{m_W^2}) \\
&= (\frac{gm_W}{\cos\theta_W})^2 (-g_\nu^\alpha + \frac{p_\nu p^\alpha}{m_W^2})(-g_\alpha^\nu + \frac{q^\nu q_\alpha}{m_W^2}) \\
&= (\frac{gm_W}{\cos\theta_W})^2 (4 - \frac{p_\alpha p^\alpha}{m_W^2} - \frac{q^\nu q_\nu}{m_W^2} + \frac{p_\nu q^\nu p^\alpha q_\alpha}{m_W^4}) \\
&= (\frac{gm_W}{\cos\theta_W})^2 (2 + \frac{(\vec{p}.\vec{q})^2}{m_W^4}) \\
&= (\frac{gm_W}{\cos\theta_W})^2 (2 + \frac{(m_H^2 - 2m_W^2)^2}{4m_W^4}) \\
&= (\frac{gm_H^2}{2m_W\cos\theta_W})^2 (1 - \frac{4m_W^2}{m_H^2} + \frac{12m_W^4}{m_H^4})
\end{aligned} \tag{B.10}$$

The $H \to WW$ decay rate can be written as

$$\begin{aligned}
\Gamma_{H\to WW} &= \int d\Omega \frac{d\Gamma}{d\Omega} \\
&= \frac{g^2}{256\pi^2}\frac{m_H^3}{m_W^2}\sqrt{1 - (\frac{2m_W}{m_H})^2}(1 - \frac{4m_W^2}{m_H^2} + \frac{12m_W^4}{m_H^4}) \int d\Omega \\
&= \frac{g^2}{64\pi}\frac{m_H^3}{m_W^2}\sqrt{1 - (\frac{2m_W}{m_H})^2}(1 - \frac{4m_W^2}{m_H^2} + \frac{12m_W^4}{m_H^4}) \\
&= \frac{g^2}{64\pi}\frac{m_H^3}{m_W^2}(1 - x_W + \frac{3}{4}x_W^2)\sqrt{1 - x_W}
\end{aligned} \tag{B.11}$$

with $x_W = \frac{4m_W^2}{m_H^2}$

So for high mass Higgs boson, the Higgs coupling to vector bosons is totally dominated by longitudinal vector boson states.

$$\hat{\sigma}(gg \to H) = \frac{(2\pi)^4}{2m_H^2}\int \frac{1}{(2\pi)^3}\frac{|M|^2}{2E}\delta^4(\vec{p}_{g1} + \vec{p}_{g2} - \vec{p}) \tag{B.12}$$

The decay width in gluon gluon fusion can be written as below where the top quark has an insignificant contribution to the total decay width.

$$\Gamma_{H\to gg} = \frac{\alpha_s^2 g^2 m_H^3}{512\pi^3 m_W^2} \mid \sum_i F_i \mid 2 \tag{B.13}$$

Appendix C

Measuring b-tag efficiency

The b-tag efficiency is defined as the fraction of reconstructed jets originating from b-quarks that are tagged by the b-tagging algorithm. It has been measured in data using p_T^{rel} method [47]. p_T^{rel} is defined as the momentum of the muon transverse to the combined muon plus jet axis. Muons originating from b-hadron decays have a harder p_T^{rel} spectrum than muons in c- and light-flavour jets (jets from up, down, strange quarks). p_T^{rel} templates are constructed for b-, c- and light-flavour jets separately, and these are fit to the p_T^{rel} spectrum in data to obtain the fraction of b-jets before and after requiring a b-tag.

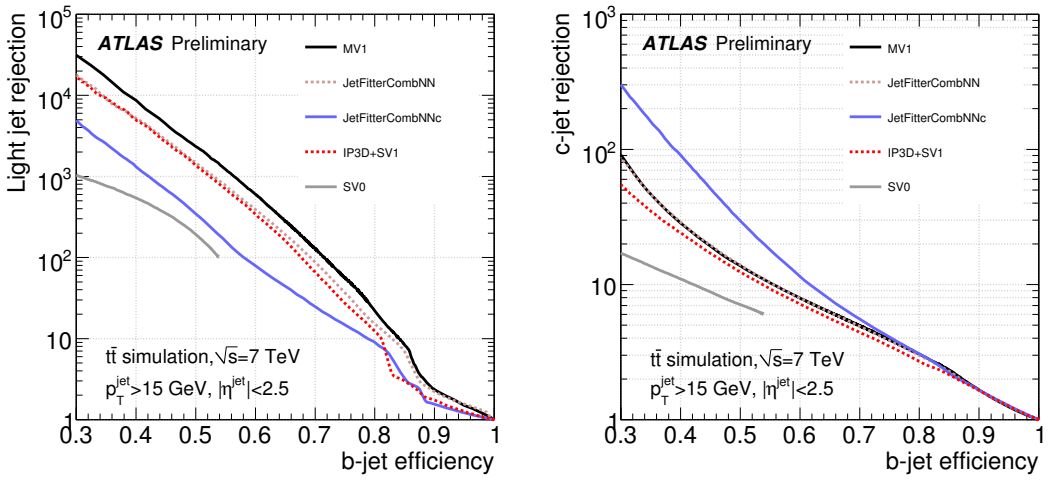

Figure C.1: Left: Light-jet rejection as a function of the b-tag efficiency, Right: c-jet rejection as a function of the b-tag efficiency for different b-tagging algorithms using simulated $t\bar{t}$ events [47].

The b-tag efficiency is defined as

$$\varepsilon_b^{data} = \frac{f_b^{tag} \cdot N^{tag}}{f_b \cdot N} \cdot C \tag{C.1}$$

where f_b and f_b^{tag} are fractions of b-jets in the pre-tagged and tagged samples while N and N^{tag} are the total number of jets in those two samples. The factor C corrects the efficiency for the biases introduced through differences between data and simulation in the modelling of the b-hadron direction.

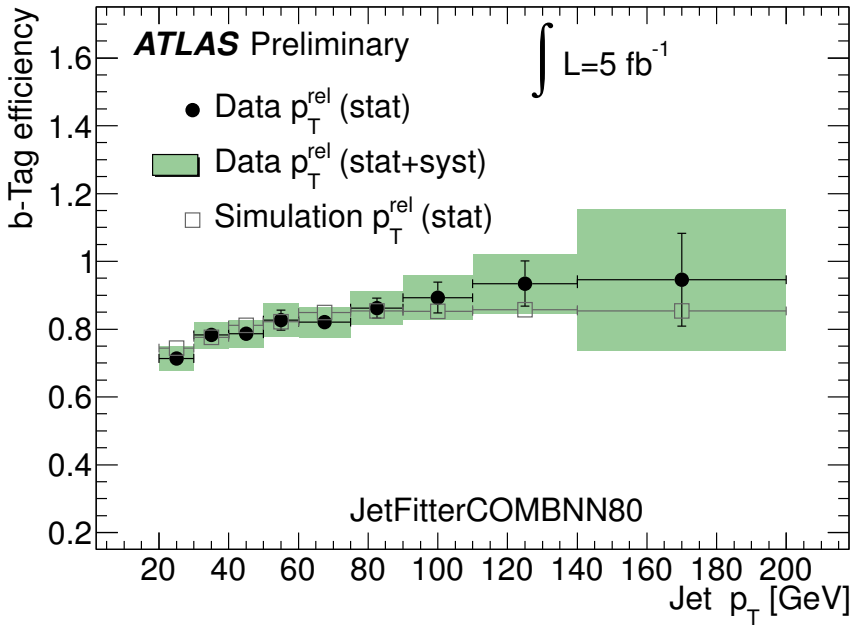

Figure C.2: The b-tag efficiency in data and simulation for the p_T^{rel} method for the JetFitterCombNN tagging algorithm (used in the analysis) at 80% efficiency [47].

Figure C.1 shows the expected performance of the various b-tagging algorithms in a simulated $t\bar{t}$ sample for jets with $p_T > 15$ GeV and $|\eta| < 2.5$.

Appendix D

Jet Energy Resolution (JER)

The transverse momenta asymmetry between two leading jets A($p_{T,1}$, $p_{T,2}$) is defined as

$$A(p_{T,1}, p_{T,2}) = \frac{p_{T,1} - p_{T,2}}{p_{T,1} + p_{T,2}} \tag{D.1}$$

The fitted Gaussian σ is used to characterize the asymmetry distribution and determine the jet p_T resolutions σ_A. Assuming transverse momentum balance ($\langle p_{T,1} \rangle = \langle p_{T,2} \rangle = p_T$) and requiring the jets to be in the same rapidity y region ($\sigma_{p_{T,1}} = \sigma_{p_{T,2}} = \sigma_{p_T}$), the relation between σ_A and the relative jet resolution is given by

$$\sigma_A = \frac{\sqrt{\left(\sigma^2_{p_{T,1}} + \sigma^2_{p_{T,2}}\right)}}{\langle p_{T,1} + p_{T,1} \rangle} = \frac{\sigma_{p_T}}{\sqrt{2} p_T} \tag{D.2}$$

$$\sqrt{2}\sigma_A = \frac{\sigma_{p_T}}{p_T} \tag{D.3}$$

The asymmetry distributions for two $\bar{p_T} = (p_{T,1} + p_{T,2})/2$ bins (20-30, 30-40 GeV) are shown in Figure D.1.

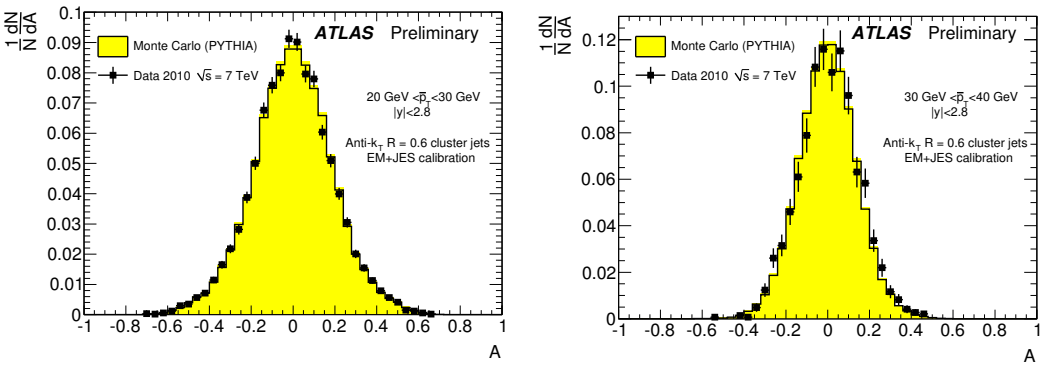

Figure D.1: Asymmetry distributions for different $\bar{p_T}$ bins and $|y| < 2.8$ [56].

Appendix E

Fits to the signal Monte Carlo for $H + 0j$ channel

E.1 $H \to WW^* \to e\nu jj$

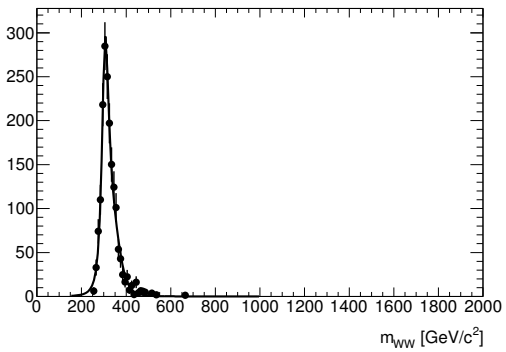

Figure E.1: $m_{WW^*} = 300$ GeV.

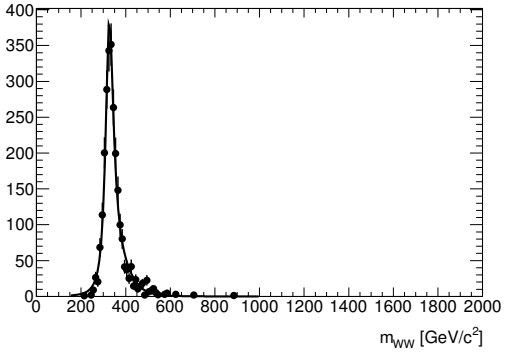

Figure E.2: $m_{WW^*} = 320$ GeV.

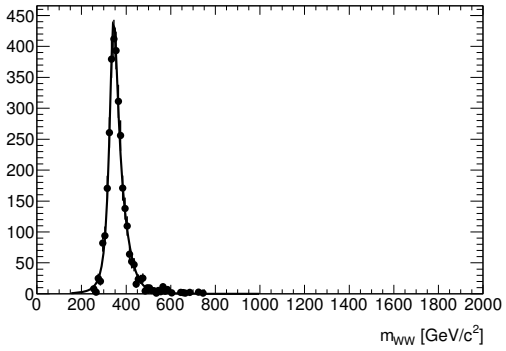

Figure E.3: $m_{WW^*} = 340$ GeV.

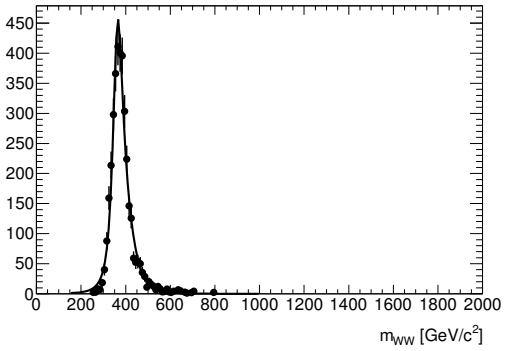

Figure E.4: $m_{WW^*} = 360$ GeV.

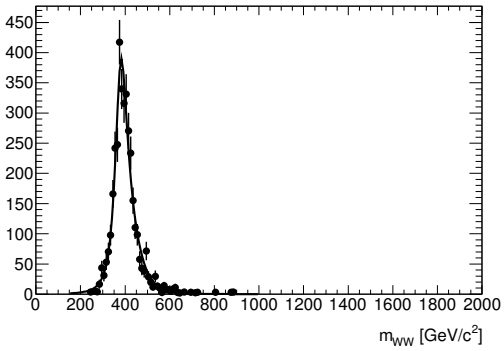

Figure E.5: $m_{WW^*} = 380$ GeV.

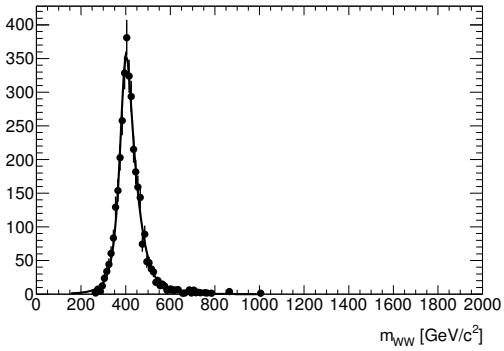

Figure E.6: $m_{WW^*} = 400$ GeV.

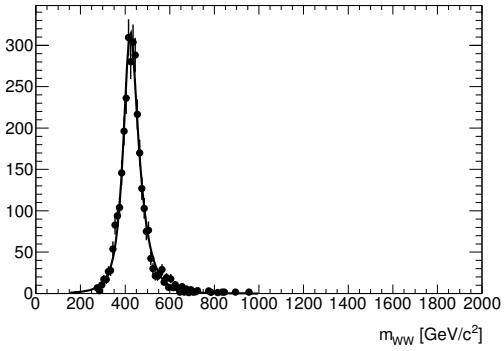

Figure E.7: $m_{WW^*} = 420$ GeV.

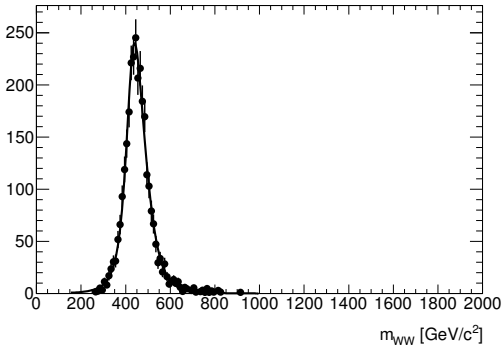

Figure E.8: $m_{WW^*} = 440$ GeV.

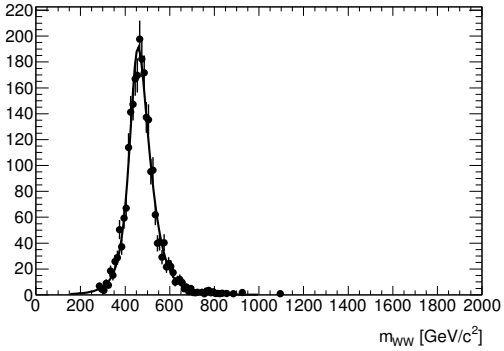

Figure E.9: $m_{WW^*} = 460$ GeV.

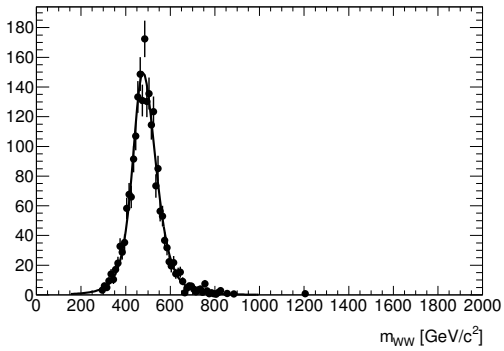

Figure E.10: $m_{WW^*} = 480$ GeV.

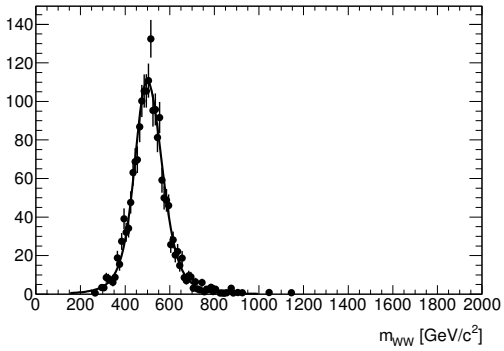

Figure E.11: $m_{WW^*} = 500$ GeV.

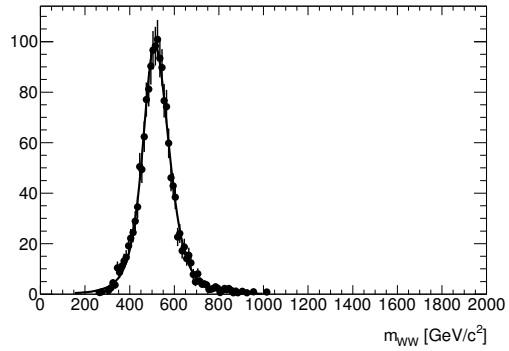

Figure E.12: $m_{WW^*} = 520$ GeV.

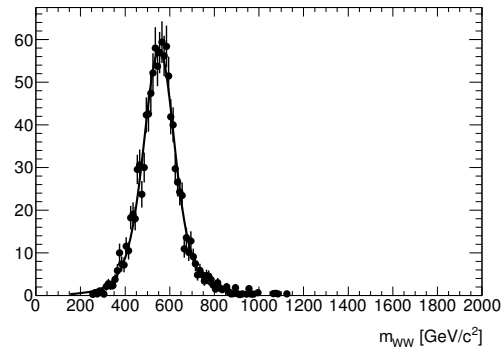

Figure E.13: $m_{WW^*} = 560$ GeV.

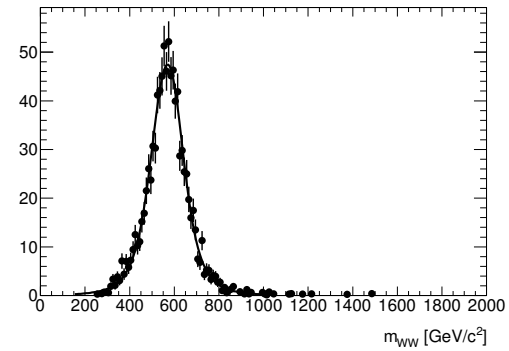

Figure E.14: $m_{WW^*} = 580$ GeV.

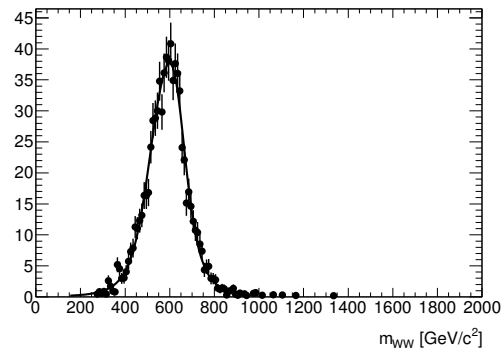

Figure E.15: $m_{WW^*} = 600$ GeV.

E.2 $H \to WW^* \to \mu\nu jj$

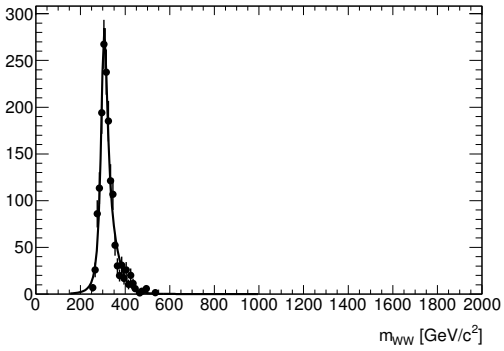

Figure E.16: $m_{WW^*} = 300$ GeV.

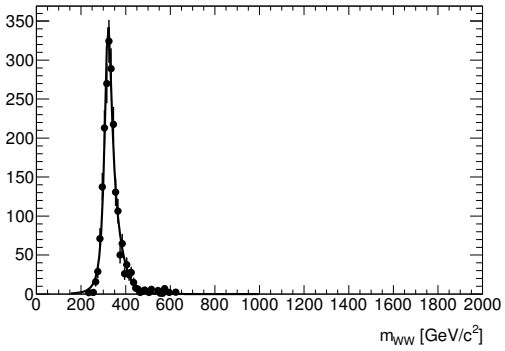

Figure E.17: $m_{WW^*} = 320$ GeV.

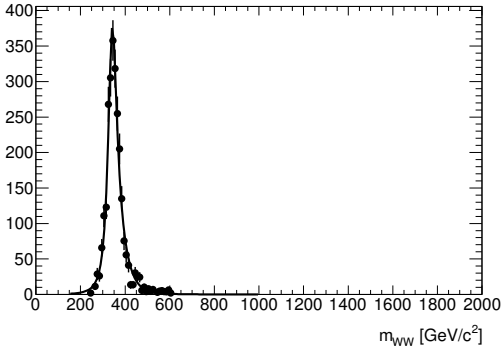

Figure E.18: $m_{WW^*} = 340$ GeV.

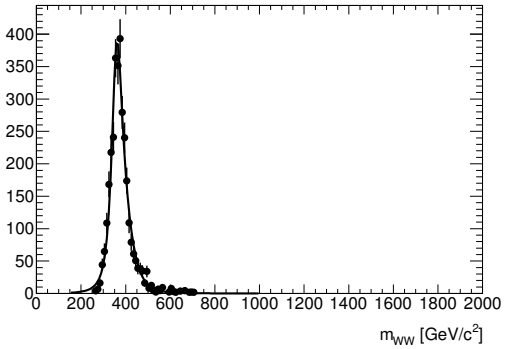

Figure E.19: $m_{WW^*} = 360$ GeV.

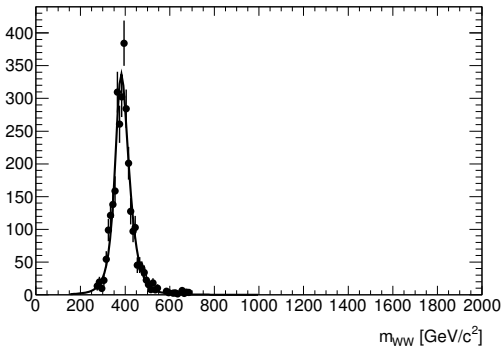

Figure E.20: $m_{WW^*} = 380$ GeV.

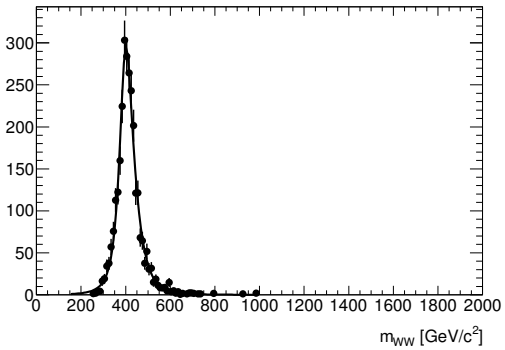

Figure E.21: $m_{WW^*} = 400$ GeV.

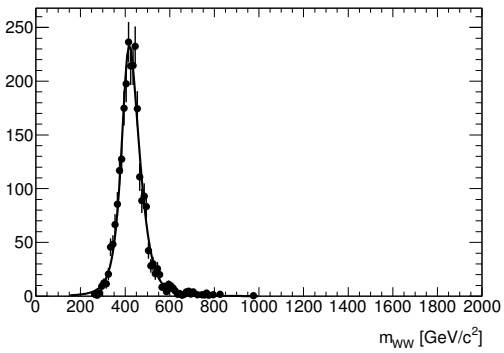

Figure E.22: $m_{WW^*} = 420$ GeV.

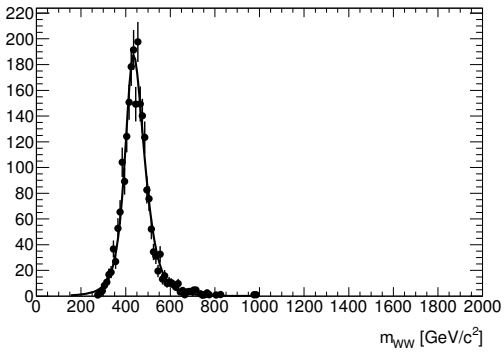

Figure E.23: $m_{WW^*} = 440$ GeV.

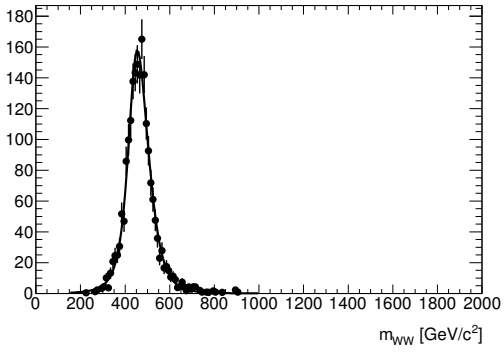

Figure E.24: $m_{WW^*} = 460$ GeV.

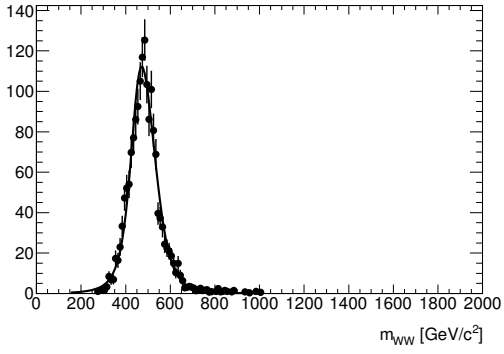

Figure E.25: $m_{WW^*} = 480$ GeV.

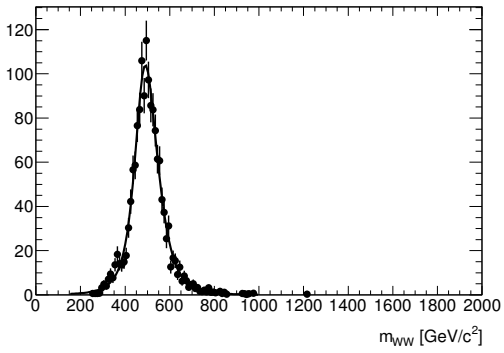

Figure E.26: $m_{WW^*} = 500$ GeV.

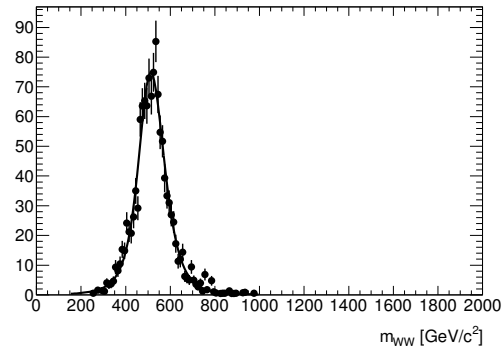

Figure E.27: $m_{WW^*} = 520$ GeV.

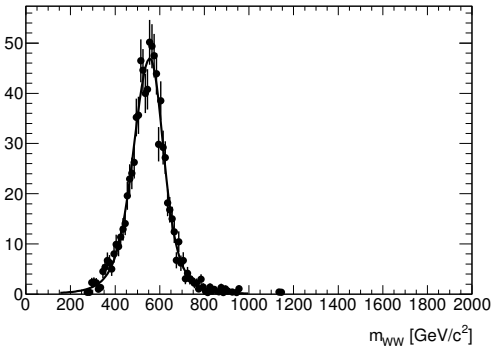

Figure E.28: $m_{WW^*} = 560$ GeV.

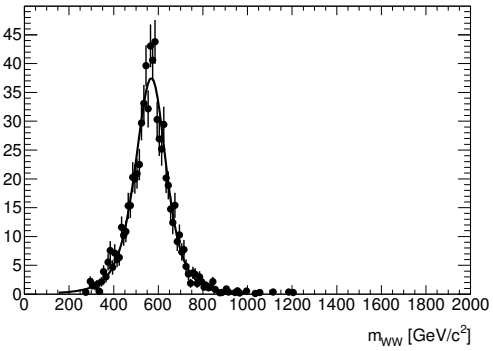

Figure E.29: $m_{WW^*} = 580$ GeV.

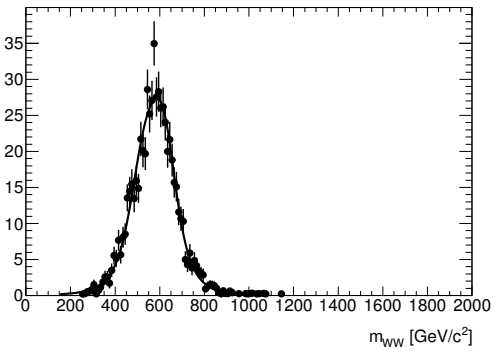

Figure E.30: $m_{WW^*} = 600$ GeV.